

# Engineering Journal



American Institute of Steel Construction

First Quarter 2017 Volume 54, No. 1

- 1 Letter from the Editor
- 3 Simple-Made-Continuous Steel Bridges with Steel Diaphragms  
Robert I. Johnson and Rebecca A. Atadero
- 21 Investigation of Web Post Compression Buckling Limit State and  
Stiffener Requirements in Castellated Beams  
Fatmir Menkulasi, Cristopher D. Moen, Matthew R. Eatherton and  
Dinesha Kurupparachchi
- 45 Observations from Cyclic Tests on Deep, Wide-Flange  
Beam-Columns  
Gulen Ozkula, John Harris and Chia-Ming Uang
- 61 Shear Capacity of High-Strength Bolts in Long Connections  
Raymond H.R. Tide

# Letter from the Editor

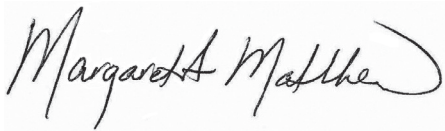
Dear Readers,

Hello and Happy New Year! As we head into the new year, I would like to take this opportunity to recognize all of the hard work of our reviewers, last year and every year. Their contributions are invaluable to the success of the *Journal* as we continue to strive to bring you the very best articles and information in the steel construction industry. A list of our 2016 reviewers is posted on the AISC website at [www.aisc.org/ej](http://www.aisc.org/ej).

Is there a steel design topic you would like to see in *EJ*? We are always looking for ideas for papers. Authors interested in submitting papers should visit our website at [www.aisc.org/ej](http://www.aisc.org/ej) for author guidelines and submittal information.

Best wishes for a healthy and happy 2017!

Sincerely,

A handwritten signature in black ink that reads "Margaret A. Matthew". The signature is written in a cursive style with a large, sweeping flourish at the end.

Margaret A. Matthew, P.E.  
Editor



# Simple-Made-Continuous Steel Bridges with Steel Diaphragms

ROBERT I. JOHNSON and REBECCA A. ATADERO

---

## ABSTRACT

Simple-made-continuous (SMC) bridges are a relatively new innovation in steel bridge design. The majority of SMC bridges currently in use are constructed with concrete diaphragms. This article presents the results of numerical analysis and physical laboratory testing of an alternative simple-made-continuous (SMC) connection scheme that uses steel diaphragms in lieu of concrete diaphragms. A bridge using steel diaphragms was constructed by the Colorado Department of Transportation in 2005, and the connections on this bridge serve as the basis for the research discussed herein. The results of the analysis and testing provided information for the development of a design methodology based on the physical behavior of the SMC connection. The paper also compares the steel-diaphragm SMC connection to concrete-diaphragm SMC connections and demonstrates that the steel-diaphragm design has several desirable features. For a diaphragm cost, which is similar in cost to other SMC schemes, the steel-diaphragm design requires less total construction time. Additionally, because the girder ends are exposed, it is easy to verify that the girders have fully weathered (for weathering steel), they may be easily inspected, and there is no concern about cracking of a concrete diaphragm at re-entrant corners around the steel bridge girders.

**Keywords:** steel bridges, composite steel girders, steel diaphragms, simple-made-continuous (SMC).

---

## INTRODUCTION

Simple-made-continuous (SMC) bridges (also known as simple for dead–continuous for live, or SD-CL) are a relatively new innovation in steel bridge design. The majority of steel girder bridges using the SMC concept have steel girders cast into concrete-diaphragm beams on concrete piers, and a significant quantity of research has been performed on these types of SMC bridges (Azizinamini, 2014). The subject of this article is an alternative SMC design using steel wide-flange-shape diaphragms and concrete support piers, which leave the entire steel structure exposed. A bridge of this type was constructed by the Colorado Department of Transportation (CDOT). It is shown prior to the placement of the concrete deck in Figure 1 and in its condition at the time of this writing in Figure 2. The specific detail was developed by CDOT due to depth limitations over an existing creek to be bridged. Originally, concrete bulb tees were considered; however, their depth did not provide the necessary 2-ft clearance over the high water level. The choice

was made to use steel girders with SMC end connections (NSBA, 2006). At the time, the concept was commonly used with precast concrete beams, and CDOT felt that the same concept could be modified to be used with steel girders.

The connection is considered in the present research because the detail is straightforward, it allows the ends of the girders to be exposed to fully weather and to be visible for periodic inspection, and SMC bridges using steel diaphragms with exposed ends have not been the subject of previous research efforts. These bridges not only have the advantages of being simpler in design and faster to construct than conventional fully continuous bridges, but they are also more than 15% less in cost than fully continuous bridges. This paper describes physical testing and analysis of the steel-diaphragm SMC bridge connection and provides cost comparisons to other SMC schemes and fully continuous girder bridges.

## BASICS OF SMC BEHAVIOR

As described in previous AISC *Engineering Journal* articles (Azizinamini, 2014; Farimani, 2014), simple-made-continuous bridge girders in effect act as simple beams for the dead load of the bridge superstructure and act as continuous beams for live loads and superimposed dead loads. The behavior is achieved by placing simple span bridge girders, which are typically cambered for the precomposite dead loads (Figure 3). After the girders are installed, the slabs are formed and top and bottom bending and shrinkage reinforcing is placed for the slab along with additional top

---

Robert I. Johnson, Ph.D., S.E., P.E., Instructor, Department of Civil and Environmental Engineering, Colorado State University, Fort Collins, CO. Email: bob.johnson@colostate.edu (corresponding)

Rebecca A. Atadero, Ph.D., P.E., Assistant Professor, Department of Civil and Environmental Engineering, Colorado State University, Fort Collins, CO. Email: ratadero@enr.colostate.edu

---



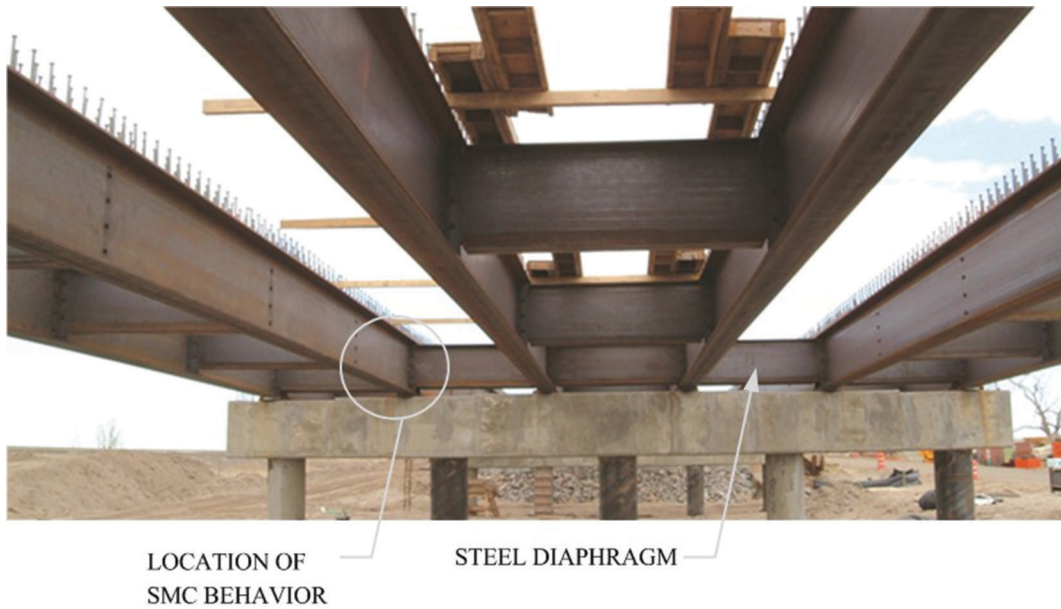


*Fig. 1. Bridge over Box Elder Creek, 2005 (reprinted courtesy of AISC).*



*Fig. 2. Bridge over Box Elder Creek, 2015.*

longitudinal reinforcing (the SMC reinforcing) placed over the supports and extended partially or fully into the spans for development (Figure 4). The concrete slab is then placed and allowed to cure and develop bond with the reinforcing steel; at this time, the camber should be nearly equalized. Once the slab has attained design strength, the additional top reinforcing placed over the supports will enable the composite section to resist negative moments and, in effect, become continuous for live and superimposed dead loads. The ability to resist negative moments, along with the combined positive moment strength of the composite section,

create a nearly continuous girder with significant strength (Figure 5).

The behavior of SMC bridges better balances the interior positive and continuous end negative moments than fully continuous girder bridges. In addition, SMC bridges actually have smaller negative moments over the supports than fully continuous girder bridges; negative moments control the design of fully continuous bridges as they are primarily resisted by the steel girder, with a small portion possibly resisted by longitudinal slab shrinkage reinforcing. The positive moments in SMC bridges are larger than those in

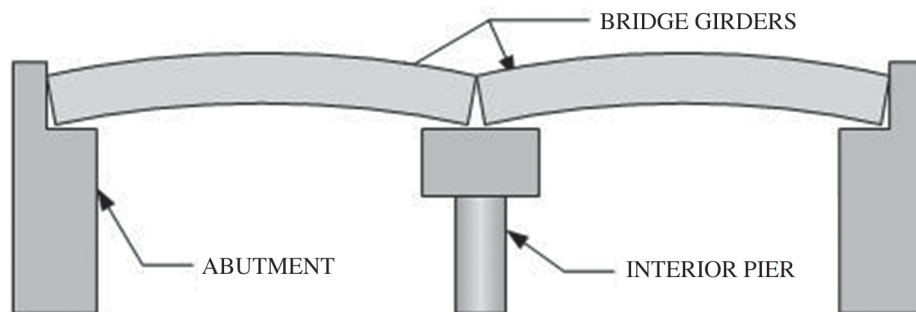


Fig. 3. Girders placed on supports.

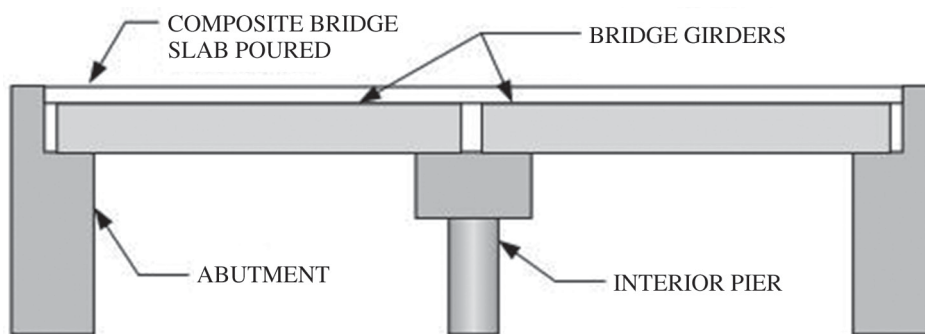


Fig. 4. Bridge deck slab cast on girders.

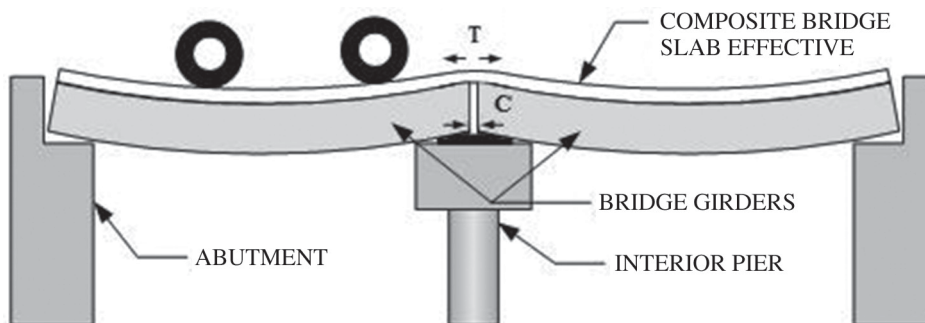


Fig. 5. Slab strength and continuity attained.

the fully continuous bridges; however, the total moment range (the sum of the absolute value of the negative moment and positive moment for a particular span) is less for SMC bridges. Figure 6 shows the combination of dead and live loads on a sample SMC bridge. The sample bridge consists of two equal 140-ft spans; the superstructure is constructed of a 10-in.-thick composite slab supported by 54-in.-deep plate girders spaced at 10 ft on center. For the first stage, when the girder is carrying the slab noncompositely, the maximum factored dead load positive moment is 4,835 kip-ft. In the SMC condition, the maximum factored positive moment is 7,450 kip-ft, while the maximum factored negative moment is 5,860 kip-ft (factored dead and live load moment range = 13,310 kip-ft). Figure 7 compares the combined moment diagrams of the sample SMC bridge to the moment diagram of a fully continuous bridge, which has maximum factored positive and negative moments of 5,585 kip-ft and -11,214

kip-ft, respectively (factored dead and live load moment range = 16,800 kip-ft). While the SMC bridge has a higher positive moment, this moment will be taken by the girder and slab in composite action; the significant advantage is the difference in the maximum negative moments. In the SMC bridge, the post-composite action negative moment is resisted by the girder in composite action with the top-reinforcing steel, whereas in the fully continuous bridge, the negative moment must be resisted by the steel girder section and only slab shrinkage reinforcing, which provides considerably less area of steel than reinforcing designed for SMC behavior. If negative moment redistribution were considered for the fully continuous bridge in accordance with AASHTO article B6.3.3, the maximum reduction to the negative moment would be 20%. The reduced fully continuous moment would be 8,971 k-ft, which is still 68% greater than the SMC negative moment.

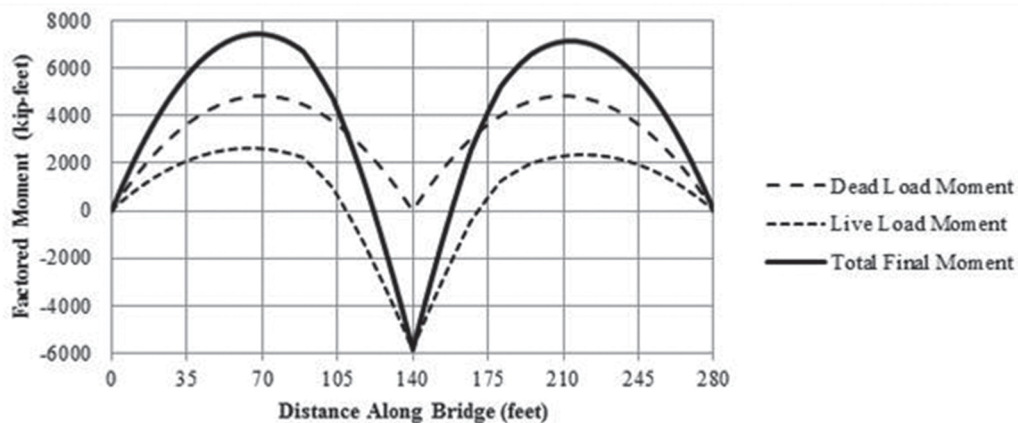


Fig. 6. Simple-made-continuous two-span bridge behavior.

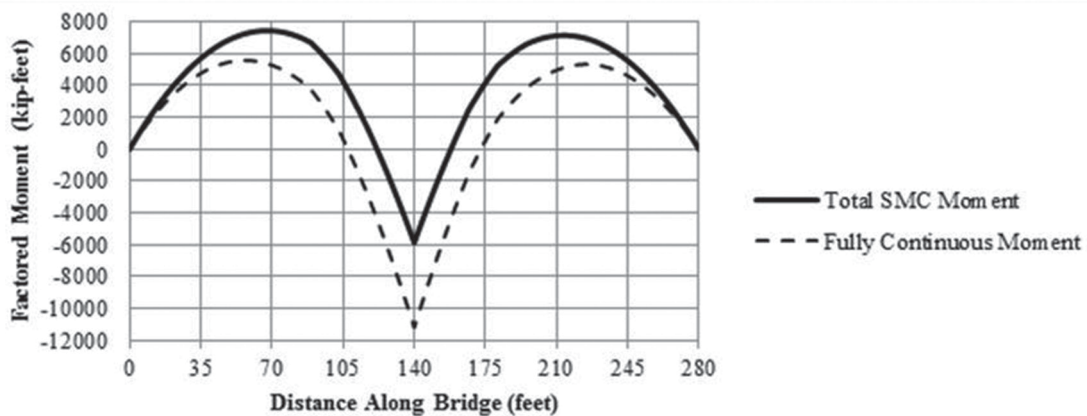


Fig. 7. Comparison of factored moments between two-span fully continuous and SMC bridge girders.

## BASIC CONNECTION BEHAVIOR

The SMC connection investigated consists of four basic load transfer elements (Figure 8):

1. SMC top-reinforcing steel.
2. Girder bottom flange.
3. Welds to bearing plate.
4. Bearing/transfer plate.

The factored moment at the continuous end of the girder is resisted by a couple between the girder bottom flange and the SMC reinforcing steel in the slab. At the end of the girder, the compression in the bottom flange is transferred by the welds to the bearing/transfer plate. The bearing/transfer plate then transfers the load from one girder end to the adjacent girder end.

While this connection detail appears simple and straightforward, there are several potential points of weakness in the design. The compression component of the moment must be resisted by shear in fillet welds in order to transfer to the adjacent girder. Failure of these welds would result in nonductile behavior; also, basic hand analysis of the force components in the connection indicated that the weld on the Box Elder Creek bridge in particular may be too small. In

addition, the weld in the position used raises fatigue concerns about the connection. While the girder bottom flange and the bearing plate are transferring the load in compression, the weld is transferring load in shear. Based upon the uniqueness of this connection and concerns regarding the weld capacity, this connection was chosen for further study, including finite element analysis (FEA) and a physical test of the connection in the lab.

## PRELIMINARY FINITE ELEMENT ANALYSIS

Finite element analysis (FEA) of the connection was performed using Abaqus finite element software. Various material models for the concrete, structural steel, reinforcing steel and welds were investigated until models with behavior that agreed within roughly 10% or less with approximate hand calculation results on a simplified bridge structure were found. The structural steel and reinforcing steel were modeled as a linear elastic material up to yield and then modeled as nonlinear up to their corresponding ultimate strengths. A concrete damage model presented by Carreira and Chu (1985) was used for the concrete slab. Following the material model selection, a sensitivity analysis was performed to determine element types to optimize both the speed of analysis and correctness of results. On the basis of the sensitivity

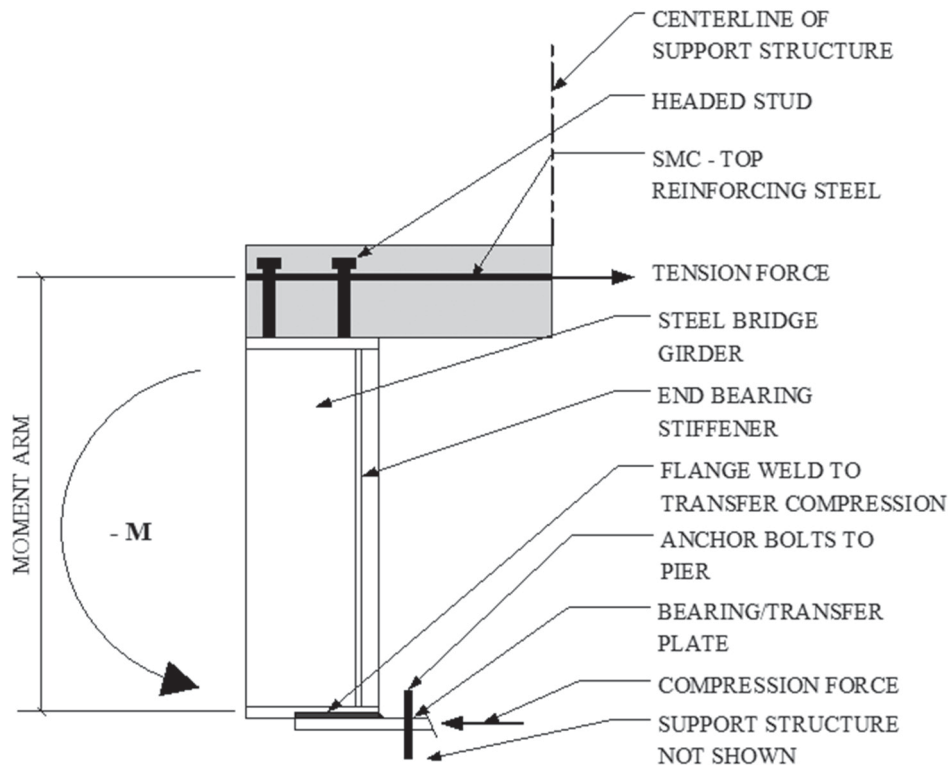


Fig. 8. Girder SMC behavior.



analysis, the element types and meshing of the full connection model were modified to take advantage of the results. The concrete slab, structural steel shapes and reinforcing steel were all modeled using linear brick elements because the use of higher-order elements provided virtually no additional accuracy in results; shear studs were modeled as beam elements. The slab connection to the studs was modeled as a tie, and the reinforcing steel was modeled as embedded in the slab.

Based on comparison with the physical test, the final FEA results provided close results for internal forces in the SMC reinforcing, girder flanges, welds and bearing/transfer plate. Of particular interest, it was noted in the FEA model that there was a reduction of the moment at the centerline of the connection due to the actual location of the reaction force not being at the center of the support, but rather at various locations under the girder end depending upon load. This effect is shown in Figure 9, which presents results of the FEA showing the moment diagram at an applied load of 98 kips, which in theory would result in a centerline moment of -1176 kip-ft instead of the actual centerline moment of 970 kip-ft. It is evident that the moment reduces once the girder bearing/transfer plate becomes involved; there is also a slight reduction in the negative moment up to the center of the plate (0 on the X-axis) and then the behavior mirrors for the adjacent girder. This effect was also observed in the physical test, although with fewer data points. Also noted in the FEA results was that the longitudinal axial stresses at isolated locations in the vicinity of the center of the bearing/transfer plate (Figure 10) were in excess of yield stress by

nearly 40%. Figure 10 also shows the location of the girder bearings, which are denoted by dashed black lines, and the locations of the welds, which are denoted by solid black lines.

The deflection at the end of the slab predicted by the FEA model was found to be about 50% of that recorded during the physical test. It appears that the difference in behavior was most likely due to the concrete material model used. Modifications to the FEA model—including varying the concrete modulus of elasticity in the slab to simulate the decreased effect of the stiffness of the concrete at the extremities of the model and at areas of cracking in the top of the slab—were considered after the physical test results were available. These modifications were able to improve the correlation between the FEA and physical test deflections. These modifications were based on physical understanding of what the concrete should be experiencing during the test, but further study is needed to provide modeling guidance that can improve a priori predictions when no test data are available for calibration.

#### EXPERIMENTAL TESTING OF FULL-SCALE CONNECTION

A physical test of the full-scale connection was conducted in the structures lab at Colorado State University (Johnson, 2015). The test specimen consisted of a center connection with two 15-ft cantilevered spans loaded with hydraulic actuators at the cantilever ends, 12 ft from the center of the connection (Figure 11). The connection was constructed as

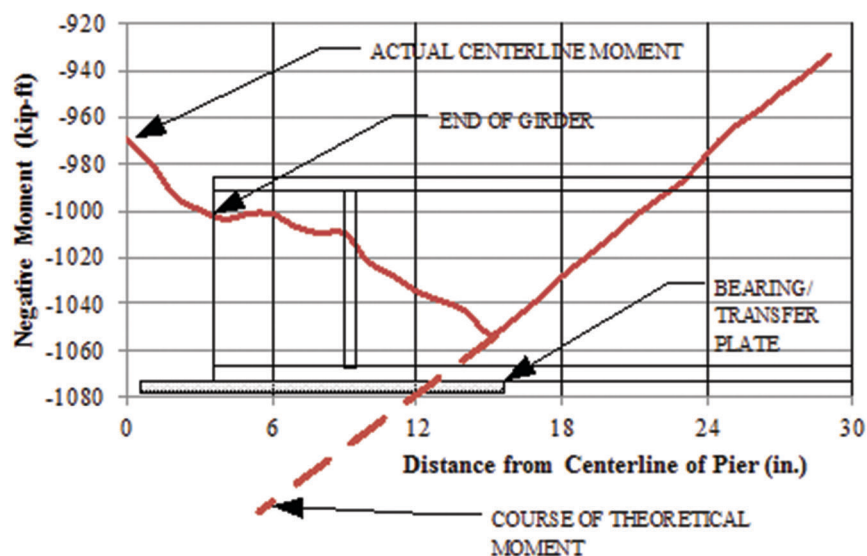


Fig. 9. Girder moment behavior over support.

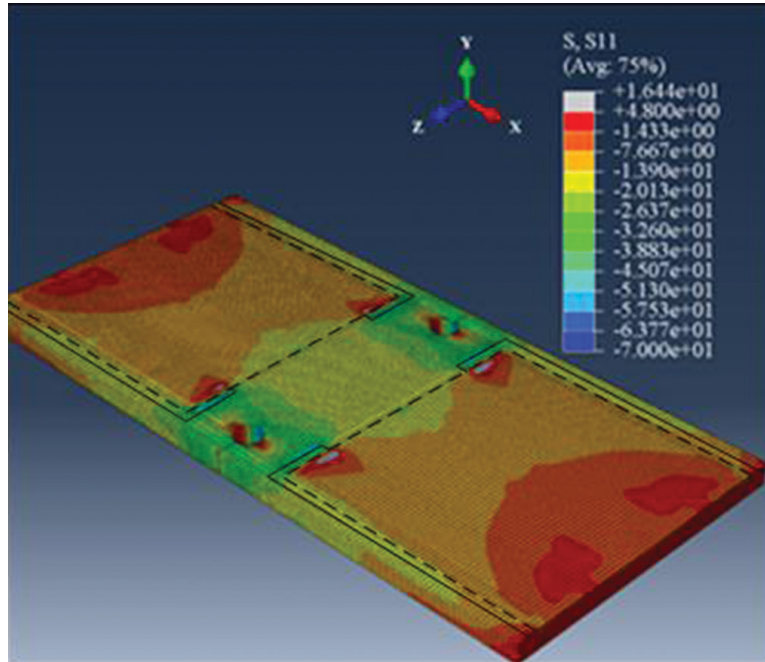


Fig. 10. Longitudinal axial stress in bearing plate (the extent of the girder bearings are indicated by the dashed lines, and the extent of the welds are indicated by the solid black lines).

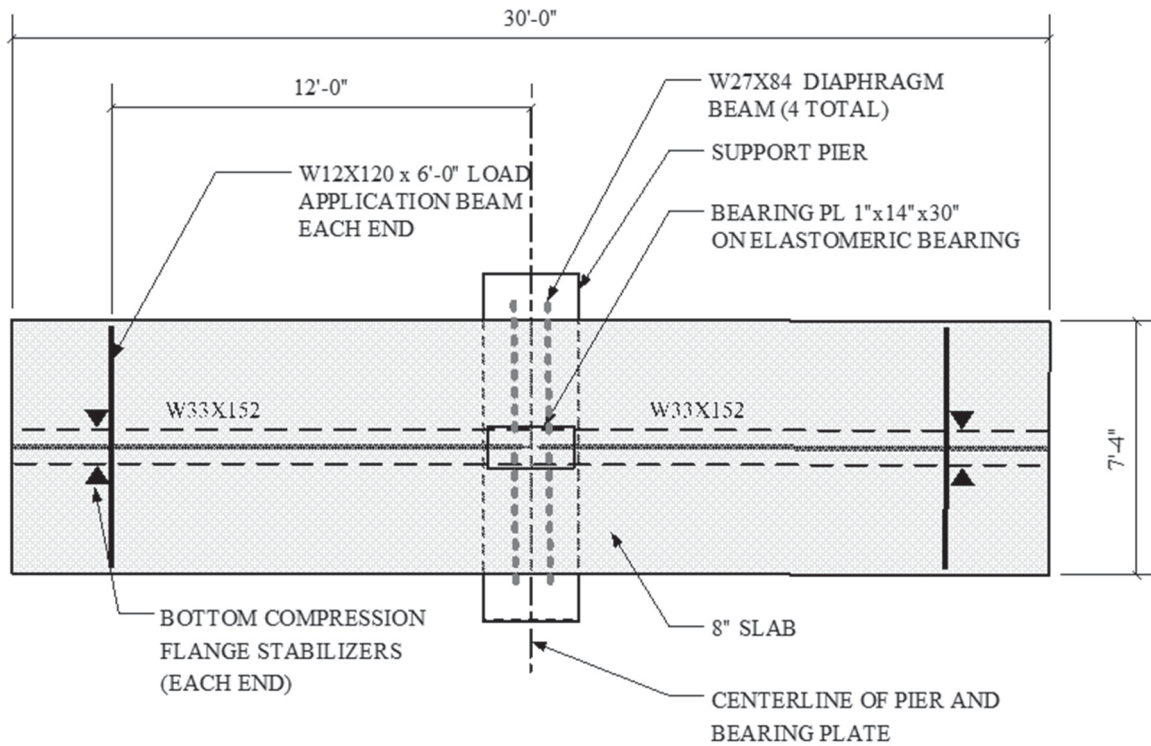


Fig. 11. Physical test specimen plan layout.

indicated in the original drawings, except for the addition of a safety device installed between the ends of the girder bottom flanges (Figures 12 and 13) to be activated in the event the welds failed as anticipated. The plate was initially installed with a gap of  $\frac{1}{16}$  in. at each side so that it did not engage prior to the anticipated failure of the fillet weld of the girder end to the bearing/transfer plate. Also, the size of the welds on one of the girder end connections was increased to ensure that both would not fail simultaneously. The final test configuration is shown in Figure 14; the center SMC connection showing the steel-diaphragm beam and the safety device is shown in Figure 15. The diaphragm beam was used in the test specimen to laterally stabilize the girder, which is its key function in the actual bridge.

During the test, the connection was loaded by displacement control at a rate of 0.02 in./min. The test specimen performed well until an actuator load of 80 kips was applied at each end, resulting in an approximate centerline moment of 960 kip-ft. At the 80-kip load point, the specimen emitted a loud bang as the girder bottom flanges made sudden contact with the safety device, which then became engaged (Figure 12). The testing was stopped and the actuators withdrawn from the test specimen. Upon visual examination of the welds and review of the strain data, no failure of the welds was evident.

Further analysis was then performed on the connection design, and it was determined that the bearing/transfer plate had yielded due to a combination of bending (both from rotation of the attached girder and the eccentric loading of the weld), axial load and deformation of the elastomeric bearing; this behavior is diagrammed in Figure 16. The following day, the cantilever ends of the test specimen were shored up, and the safety device was removed and machined down  $\frac{1}{8}$  in. in order to allow a slightly larger gap between it and the girders. The safety device was then reinstalled and the test recommenced.

During the recommenced test, at an applied load of 120 kips, which resulted in an approximate centerline moment of 1,440 kip-ft, there was another loud bang, again due to the safety device (Figure 12) becoming activated. The loading was halted and the actuators unloaded. The welds matching the actual construction (north connection) were examined and found to be cracked along the sides and end of the girder. Based on original hand calculations for the strength of the weld and the behavior of the connection, the estimated ultimate moment for the welds was 1433 kip-ft. Testing thus confirmed that the welds were undersized.

Following the examination of the connection and verifying that the safety device was properly seated, the test was restarted again. Due to limitations of the actuators and the load frame used for the test, the maximum load that could be applied at each girder end was 200 kips, and this full load was successfully applied to the connection, producing in a theoretical centerline moment of 2400 kip-ft without incident. The 2400-kip-ft moment is well in excess of the maximum ultimate design moment of 1783 kip-ft.

Strain gages positioned on the SMC reinforcing, the bearing/transfer plate and the safety device provided additional information about the behavior of the connection. Figure 17 shows the axial force in the top SMC bars and also the top SMC bars in combination with the top temperature bars at the center of the connection; this diagram gives a clear picture of the shear lag behavior in the slab. For comparison, the shear lag from the FEA is also shown, which is very similar in shape and varies by a maximum of approximately 10%. Reviewing the shear lag behavior of the connection (Figure 17), it is apparent that the bars immediately adjacent to the bar directly over the girder take a disproportionate share of the SMC tension component. In the case investigated, the bars immediately adjacent to the center bar each resisted 8% of the total SMC tension. Research performed at the University of Nebraska (Niroumand, 2009) indicated that for



Fig. 12. Safety device at end of physical test.

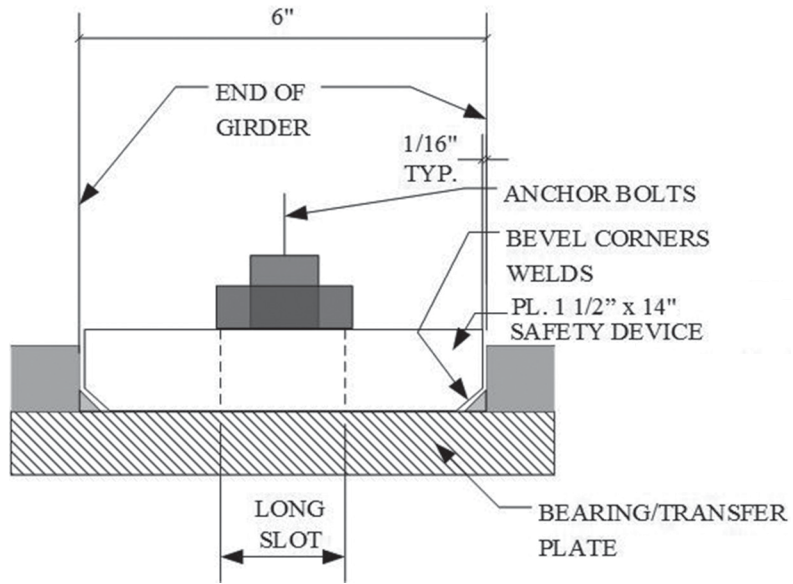


Fig. 13. Construction detail of safety device.



Fig. 14. Physical test specimen.

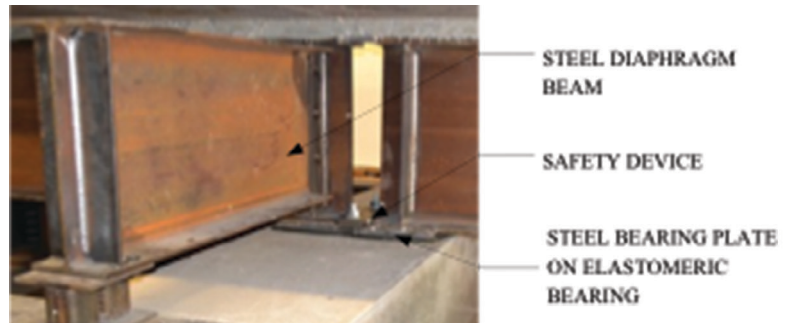


Fig. 15. Detail at steel diaphragm.

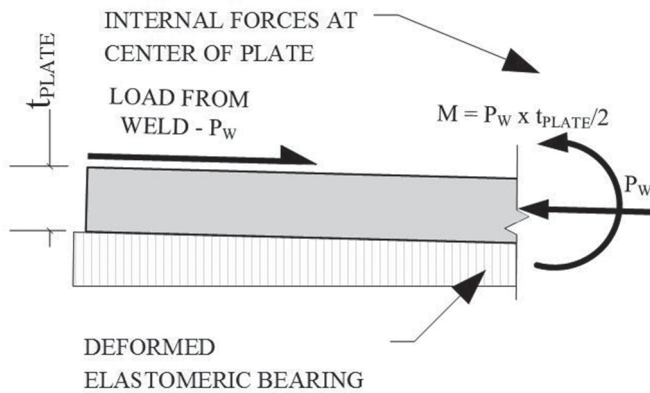


Fig. 16. Effects of load eccentricity at center of bearing plate.



<b>Event</b>	<b>Theoretical Moment at Center of Support, kip-ft</b>	<b>Actual Moment at Center of Support, kip-ft</b>	<b>Center of Actual Bearing from Center of Bearing Plate, in.</b>
End of day 1 test, load = 135 kips	1620	1490	12
Activation of safety device, day 2 test	1440	1370	10.5
End of day 2 test, load = 196.5 kips	2360	2230	8

SMC bridges, loaded such that the top reinforcing begins to yield near the center (as is the case herein), and upon the application of additional load, the adjacent bars would begin to take more load and the behavior would continue to propagate until the last bars in the effective width had yielded. While this behavior is acceptable in an overload condition, having the center bars and adjacent bars possibly going plastic under normal service conditions would be unacceptable due to excessive slab cracking and permanent elongation in the SMC reinforcing. Thus, in order to prevent yielding of the most highly stressed SMC bars, it is recommended that additional bars be placed adjacent to the as-designed SMC reinforcing. The best way to achieve this is by placing the longitudinal top shrinkage reinforcing at the same spacing and adjacent to the SMC reinforcing and using a minimum of #5 bars. As it so happens, all of the SMC bridges reviewed for this study spaced the top shrinkage reinforcing bars at the same spacing as the SMC reinforcing, which was most likely for ease of placement and to avoid confusion. Further study of the shear lag phenomenon is recommended to evaluate the behavior of the SMC reinforcing bars acting with the shrinkage reinforcing to verify that they have the

capability to prevent the center SMC bars from yielding.

Comparison of the physical test results to hand calculations of the moments indicated that the actual centerline moment was less than that predicted by hand calculation on an ideal cantilever. Figure 18 and Table 1 show the theoretical centerline moment as that calculated using a point support of the SMC girder, while in actuality, the girder begins to be supported and thus relieved of load at the face of the bearing/transfer plate; this was also the case in the finite element analysis as shown in Figure 9. The actual moment is the moment at the center of the support based on the actual support condition. The actual moment values are as shown in Table 1 and were determined by evaluating strains in the SMC reinforcing steel, the bearing/transfer plate and the safety device; their moment arms were then used to the current neutral axis—i.e., assuming the web carries no moment. Table 1 also lists the distance from the center of actual bearing to the center of the bearing/transfer plate. This phenomenon again is due to the reaction being under the beam bearing and, in actuality, much closer to the position of the beam bearing stiffener; this behavior would also occur in the actual bridge, a continuous-for-live-load structure. This

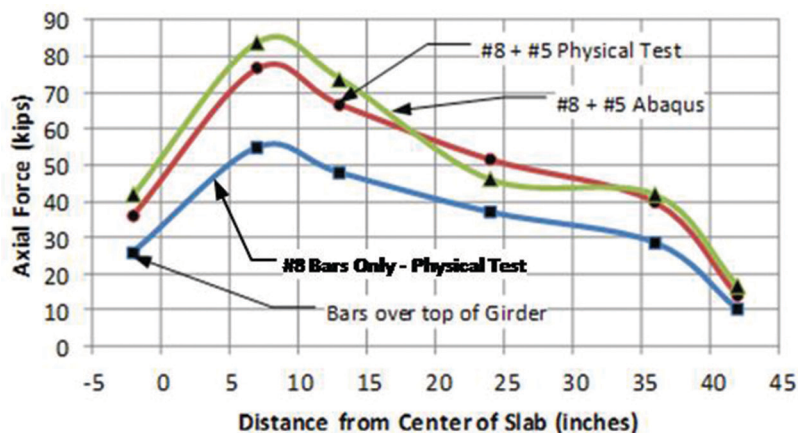


Fig. 17. Axial force in top slab bars at center of connection—physical test vs. Abaqus.

means that designing the connection for the full theoretical centerline moment would be somewhat conservative.

### RECOMMENDED IMPROVEMENTS TO DESIGN AND DESIGN METHODOLOGY

The scheme investigated has several design flaws, specifically the welds to the bearing/transfer plate and the bearing/transfer plate itself. The welds are undersized and thus inadequate to resist the maximum design loads. In addition, the welds would be subject to a load-induced fatigue category E', which limits the constant amplitude fatigue threshold to 2.6 ksi, a fatigue range that would be far exceeded during the course of regular service of the bridge. The bearing/transfer plate, which is connected to the girder bottom flange by the aforementioned welds, is unable to resist the combined effects of the axial compression and the moment induced into the plate by the eccentricity of this compression. In order to avoid plate and weld failure and subjecting the welds to fatigue, a direct means of load transfer between the bottom girder flanges would be desirable.

As was described in the testing portion of this article, a safety device (Figure 13) was installed in the event that the welds failed, and during testing, this device successfully transferred the compressive force component of moment when the bearing/transfer plate failed. Due to the satisfactory behavior of this device, it is recommended that a transfer device similar to the safety device be used in new

designs, omitting the welds to the bearing plate and any connection of the girders to the base plate. This modification to the connection will be a definite improvement to the scheme investigated, in both strength and economy. A proposed solution is shown in section in Figure 19 and in plan in Figure 20; this detail provides two wedge-shaped plates to allow for field fit-up based on designs used in partial SMC bridges in Tennessee (Talbot, 2005). The girders are laterally supported by anchor bolts through their bottom flanges and cast into the support pier.

The design methodology for the proposed scheme involves three major steps: (1) preliminary steel girder design, (2) design of SMC top-reinforcing steel based on the girder size and (3) verification of the girder size. Design of the steel girders is based on:

1. Their strength and stability to support themselves, formwork, wet concrete and any construction live load as noncomposite, simple beams.
2. Their composite positive moment strength to support the superimposed loads from the SMC behavior along with the locked-in forces from item 1.
3. Additionally, the composite girders must be evaluated to meet all the post-composite strength and serviceability requirements, in particular, deflection. These girders are typically cambered for the dead loads of the girder and the composite slab, so only deflection due to post-composite loads needs to be considered.

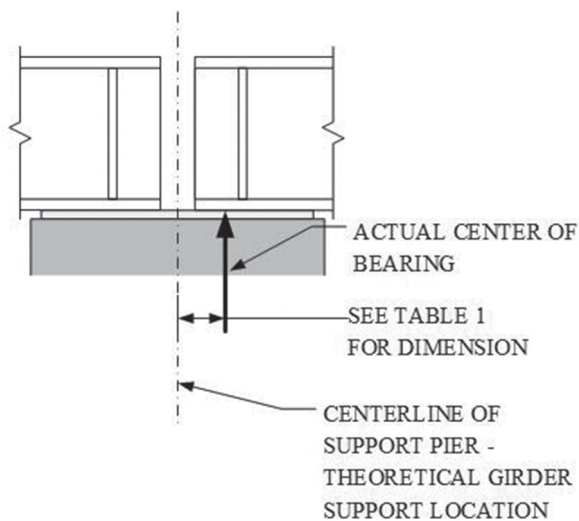


Fig. 18. Theoretical vs. actual center of girder bearing.

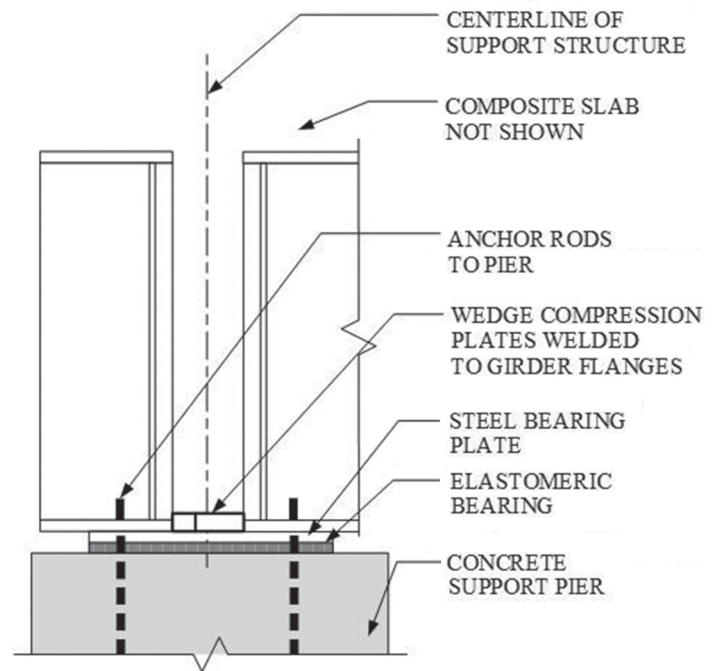


Fig. 19. Recommended revised bearing plate section.

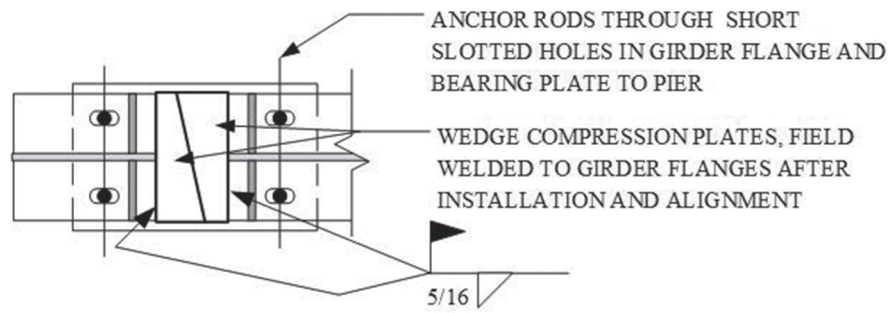


Fig. 20. Recommended revised base plate plan.

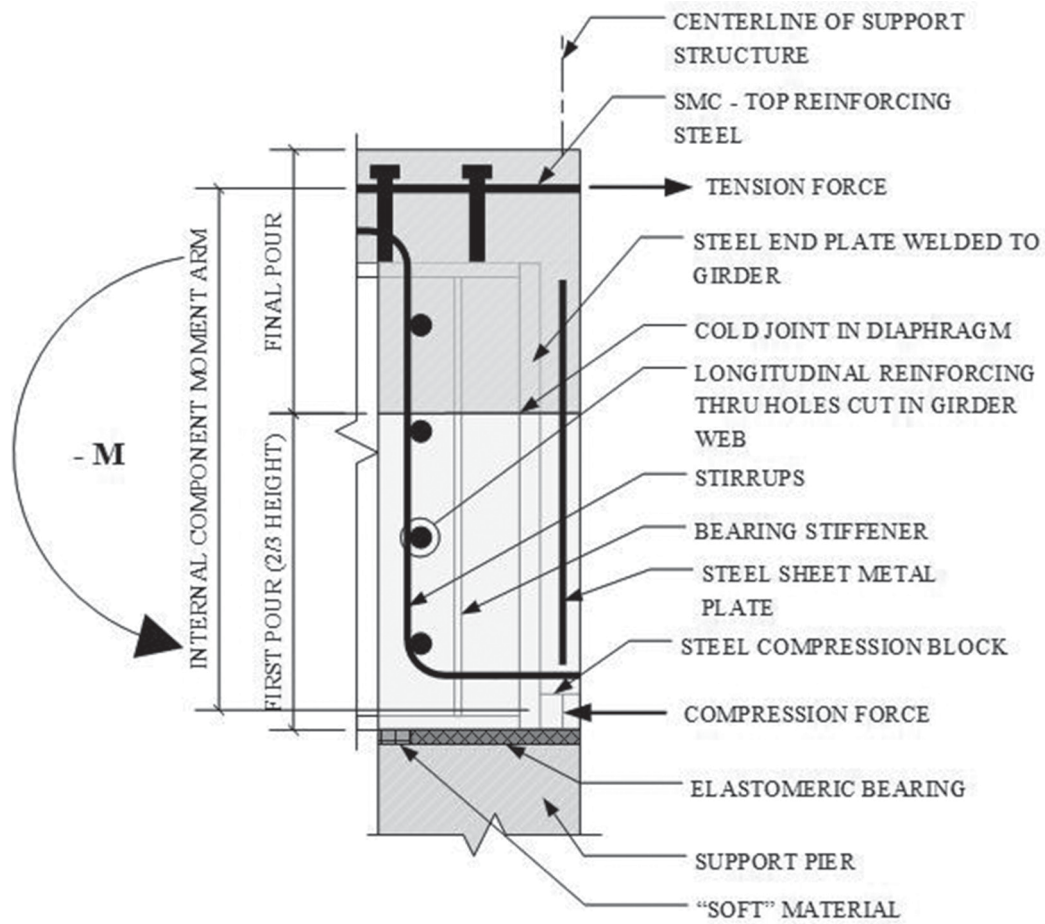


Fig. 21. Details of SMC connection (Azizinamini, 2014).

After the girders are sized, design of the remaining connection elements is relatively straightforward, and the overall behavior is similar to that developed by researchers studying SMC connections with concrete diaphragms (Azizinamini, 2005, 2014). The current concrete-diaphragm scheme proposed and developed by these researchers and currently in use is shown in Figure 21; this detail basically resists the SMC moment by a couple between the SMC top-reinforcing and steel-compression blocks between the bottom flanges and portions of the webs of the girders. For the steel-diaphragm scheme proposed herein, there are two important differences: The first is not encasing the connection in a concrete diaphragm, but rather leaving the connection exposed and using steel diaphragms. The second is that the compression component is transferred only between the girder bottom flanges using longitudinally adjustable wedge compression transfer plates because, with this SMC scheme, only the bottom flange is considered to resist the compression component of the SMC behavior. The wedge plates should be  $\frac{3}{8}$  in. or greater in thickness than the bottom flanges in order to provide sufficient depth for the weld to the girder flange. By considering only the bottom flange in compression, the internal moment arm is larger and thus will require less total resultant force in the tension and compression components

for the same moment capacity (Figure 22); this is not to say the stresses will be lower, only the resultant couple forces. After the girder size has been established, the moment arm between the girder bottom flange and the SMC top-reinforcing steel is easily determined as it is a function of all known values and an assumed SMC reinforcing bar diameter. For 50-ksi girder steel and 60-ksi reinforcing steel, the area of the reinforcing steel can be easily determined by directly equating the total area of SMC reinforcing steel required to the area of the girder bottom flange without regard to the differences in yield strength or resistance factors, which will add a very slight conservatism to the design.

Once the reinforcing steel area is known and the resultant moment arm determined, the final check of the girder is to verify that the moment capacity developed is adequate for the design negative moment due to the SMC behavior. This is accomplished by multiplying the girder flange area by the yield strength of the flange (resistance factor,  $\phi = 1.0$ ) and then by the moment arm determined. The resultant internal moment strength from the previous calculation should be compared with the actual factored design negative moment in the bridge; if the applied factored moment is less than the strength, then the connection is adequate. Otherwise, the girder size should be increased to the next available shape in

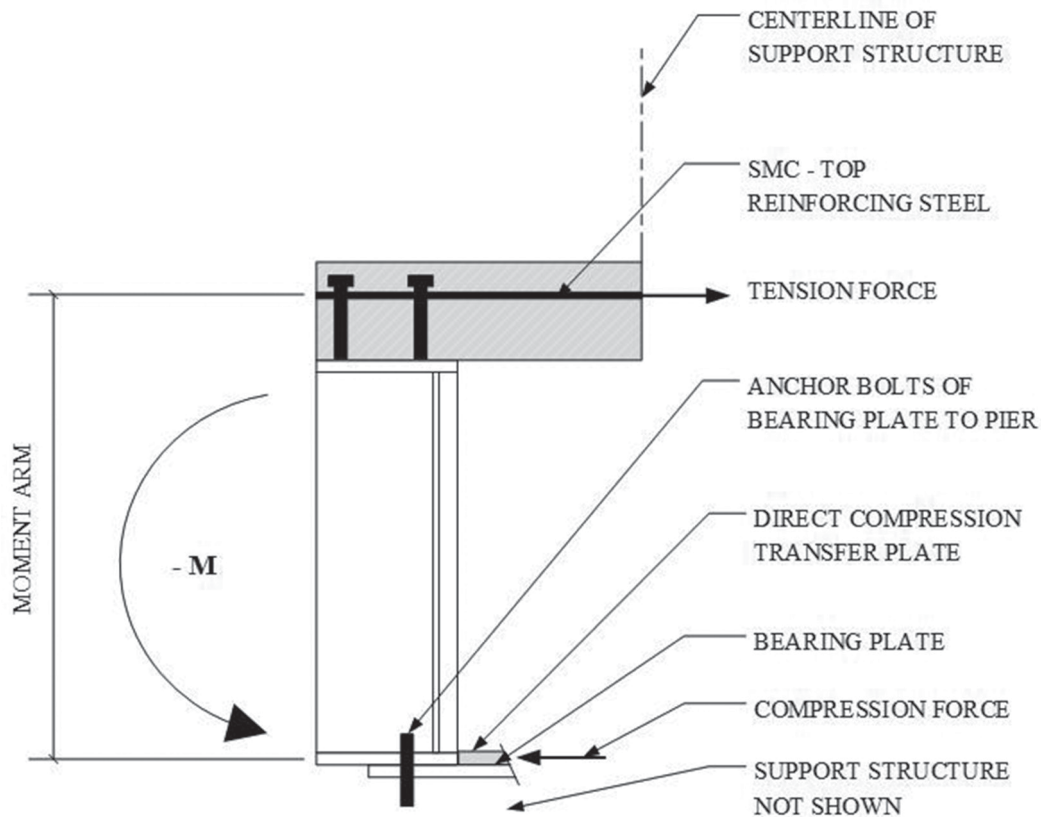


Fig. 22. Final proposed support detail.

the depth range and the second and third steps repeated. If the next girder is a deeper depth range, it would be prudent to reanalyze the bridge because there could be load distribution consequences based on the increased depth and corresponding increase in stiffness. It is important to note that this is a somewhat simplistic design methodology for a connection with a complex behavior and not fully continuous behavior. Full continuity of the girder would require continuity of the webs; however, it is apparent that the stiffness of the webs relative to moment resistance is a small fraction ( $\leq 20\%$  based on comparison of sample  $Z_x$ 's of various shapes) of that of the flanges and SMC reinforcing. Based on the additional conservatism of using the theoretical factored centerline moments versus actual factored moments (Table 1), a typical continuous girder analysis for superimposed dead and live loads would be reasonable for design. It should be noted that no other SMC connection or partial SMC connection reviewed has a positive full-height connection between girder webs.

The design procedure for the SMC connection components based upon a selected girder size is outlined here:

1. Design of SMC reinforcing. Equate the area of SMC reinforcing to the area of the bottom flange:

$$A_r = A_f = b_f t_f$$

where

$A_r$  = required area of SMC reinforcing steel, in.<sup>2</sup>

$A_f$  = area of girder bottom flange, in.<sup>2</sup>

$b_f$  = width of bottom flange, in.

$t_f$  = thickness of bottom flange, in.

The recommended minimum bar size is #8; smaller bars would require a significantly greater number (over 30%) of bars be placed.

2. Determine the moment arm of the couple between the girder bottom flange and the SMC reinforcing based on girder and slab geometry:

$$d_m = d_h + t_s - cl - D_t - \frac{D_{SMC}}{2} + d_G - \frac{t_f}{2}$$

where

$d_h$  = depth of haunch, in.

$t_s$  = thickness of slab, in.

$cl$  = reinforcing clear distance, in.

$D_t$  = main (lateral) top reinforcing bar diameter, in.

$D_{SMC}$  = SMC (longitudinal) reinforcing bar diameter, in.

$d_G$  = depth of girder flange, in.

$t_f$  = thickness of girder flange, in.

3. Verify the moment capacity of the section designed using the area and yield stress of the girder flange:

$$\phi M_n = A_f d_m F_{yG}$$

where

$\phi$  = 1.0 for the steel girder

$M_n$  = nominal moment capacity, kip-in.

$A_f$  = area of the bottom flange, in.<sup>2</sup>

$d_m$  = moment arm between SMC reinforcing and center of bottom flange, in.

$F_{yG}$  = yield stress of girder flange, ksi

4. Size the compression transfer wedge plates based upon girder bottom flange dimensions:

$$w_{tp} = b_f + \frac{1}{2}$$

$$t_{tp} = t_f + \frac{3}{8}$$

where

$w_{tp}$  = minimum width of transfer plate, in.

$b_f$  = width of girder bottom flange, in.

$t_{tp}$  = minimum thickness of transfer plate, in.

$t_f$  = thickness of girder bottom flange, in.

A design example is presented next for a bridge with 80-ft girder spans, a 9-in.-thick slab, 9-ft girder spacing and #9 SMC reinforcing bars. From a strength and serviceability analysis of the composite section for positive moments, a W33x169 was selected. The SMC moment is -2248 kip-ft.

$$b_f = 11.5 \text{ in.}$$

$$t_f = 1.22 \text{ in.}$$

$$d = 33.8 \text{ in.}$$

$$A_f = (1.22 \text{ in.})(11.5 \text{ in.}) = 14.03 \text{ in.}^2$$

$$d_h = 3.00 \text{ in.}$$

$$t_s = 9.00 \text{ in.}$$

$$cl = 2.50 \text{ in.}$$

$$D_t = 0.625 \text{ in. (#5 bar)}$$

$$D_{SMC} = 1.125 \text{ in. (#9 bar)}$$

$$d_g = 33.8 \text{ in.}$$

$$t_f = 1.22 \text{ in.}$$

$$d_m = 3.00 \text{ in.} + 9.00 \text{ in.} - 2.50 \text{ in.} - 0.625 \text{ in.} - \frac{1.125 \text{ in.}}{2}$$

$$+ 33.8 \text{ in.} - \frac{1.22}{2} \text{ in.} = 41.5 \text{ in.}$$

$$\phi M_n = \frac{14.03 \text{ in.}(41.5 \text{ in.})(50 \text{ ksi})}{12 \text{ in./ft.}} = 2,426 \text{ kip-ft}$$

$$> 2,248 \text{ kip-ft} \quad \mathbf{o.k.}$$

Determine SMC bar quantity and spacing:

$$A\#9 = 1.00 \text{ in.}^2$$

$$N = 14.03 \text{ in.}^2 / (1 \text{ in.}^2 / \text{bar}) = (14) \#9 \text{ bars}$$

$$\text{Slab width} = 9.00 \text{ ft} = 108 \text{ in.}$$

$$\text{Spacing} = 108 \text{ in.} / 14 \text{ bars} = 7.7 \text{ in./bar; use \#9 at } 7\frac{1}{2} \text{ in.}$$

Compressions transfer plate size:

$$t_{tmin} = t_f + 0.375 \text{ in.} = 1.22 \text{ in.} + 0.375 \text{ in.} = 1.595 \text{ in.}$$

$$W_{tmin} = b_f = 11.5 \text{ in.} + 1.00 \text{ in.} = 12.5 \text{ in.}$$

Use compression transfer plate: 1 $\frac{5}{8}$  in.  $\times$  12 $\frac{1}{2}$  in.



Table 2. Comparison of SMC to Fully Continuous Moments					
Bridge Type	Location				
	Span 1 Interior, kip-ft	Spans 1 and 2 Support, kip-ft	Span 2 Interior, kip-ft	Spans 2 and 3 Support, kip-ft	Span 3 Interior, kip-ft
SMC	+2460	-1970	+2030	-1640	+2110
Fully continuous	+2170	-2730	+1420	-2180	+1570

Table 3. Material Unit Costs		
Material	Unit Cost	Units
Structural steel	\$2500	Ton
Girder splice (Azizinamini, 2014)	\$2000	Each
Epoxy-coated reinforcing steel	\$1685	Ton

Table 4. Girder Cost Comparison Fully Continuous Bridge to SMC Bridge per Girder		
Element	Fully Continuous	Simple-Made-Continuous
Girder	\$19,360	\$14,790
Splice	\$2,000	0
SMC reinforcing	\$0	\$2,580
Total cost	\$21,400	\$17,400
Cost difference	23.0%	

### COMPARISON TO FULLY CONTINUOUS STEEL BRIDGES

SMC construction has been touted as a way to make construction with steel more cost effective (NSBA, 2006). To compare the costs with the steel-diaphragm connection, the State Highway 36 bridge over Box Elder Creek was analyzed for the as-constructed SMC condition and as a fully continuous for all loads condition. The girders spans (77 ft 10 in.), girder spacing (7 ft 4 in.) and slab thickness (8 in.) were the same for both bridges. Maximum positive and negative moments in the first two spans of this six-span bridge are shown in Table 2. As is evident, the negative moments are considerably larger for the fully continuous girder bridge and, thus, would require larger girders than the SMC girder bridge. This is a significant point because it means that the SMC girder bridge would not only be simpler and faster to construct than a conventional fully continuous girder bridge, but it would also be more economical by requiring lighter girders.

The fully continuous girder bridge required to resist the negative moments would be a W40×199, W36×231 or W33×241 girder, depending upon depth restrictions. The SMC girder was a W33×152, and the SMC reinforcing

consisted of approximately 14.5 #8 epoxy-coated SMC reinforcing bars full span. The slab bending and shrinkage reinforcing was assumed to be the same for both bridges. Assuming no depth restrictions and selecting the lightest size, W40×199, and using the unit costs shown in Table 3, a cost comparison was performed and is shown in Table 4. For a six-span six girder bridge, the total cost savings is more than \$143,000. The cost comparison used data from RS Means, *Open Shop Building Construction Cost Data* (Waier, 2003); this particular edition was selected for ease of cost comparisons with other SMC bridge schemes with documented cost information.

### COMPARISON TO STEEL BRIDGES USING OTHER SMC CONCEPTS

The most commonly used SMC scheme is one in which the steel bridge girders are encased in concrete diaphragms at the piers; based on all available data, this design appears to have been developed by researchers at the University of Nebraska. The Nebraska researchers based their use of a concrete diaphragm for this scheme on the existing Nebraska Department of Roads standards (NDOR, 2001)

Table 5. Cost Comparison—Concrete vs. Steel Diaphragm						
Bridge	Sprague over I-680			S.H. 36 over Box Elder Creek		
Element	Quantity	Unit Cost	Total Cost	Quantity	Unit Cost	Total Cost
Formwork	69 SFCA	\$7.05	\$486			
Epoxy-coated reinforcing steel	0.09 ton	\$2545	\$229			
Cast-in-place concrete	3.5 CY	\$116	\$371			
Sheet steel plate	1.75 cwt	\$52.5	\$92			
End plates and welding	2 each	\$202	\$404			
W27×84 diaphragms				14.67 ft	\$70.6/ft	\$1036
Girder weld to sole plate	3 LF	\$12.75/LF	\$38	5 LF	\$12.75/LF	\$64
Total			\$1620			\$1100
Diaphragm length	10.33 ft			7.33 ft		
Cost/foot		\$157			\$150	

used in the design of precast concrete girder SMC bridges without any other justification (Azizinamini, 2005). The use of the aforementioned scheme led to cracking at the ends of the concrete diaphragms; thus, in subsequent designs, gage metal steel plates were installed into the pier diaphragms during their construction to alleviate the cracking (Azizinamini, 2014).

The installation of the girder ends into a concrete diaphragm is not only a time-consuming process, but also requires additional construction time. Moreover, there are possible effects on the long-term performance of the connection, specifically:

1. The diaphragm concrete may develop cracks at reentrant corners of the girder.
2. If cracks develop in the diaphragm, this may allow moisture to penetrate into the diaphragm, potentially causing freeze-thaw damage.
3. The girder ends and, particularly, the SMC transfer mechanism are not visible for periodic inspection.

A comparison of diaphragm construction costs was made between the two methods as the diaphragm construction for either scheme would not vary significantly (<5%) between different bridge girder spans as shown in Table 5. The bridges used for comparison are the bridge carrying Sprague Avenue over I-680 in Omaha, Nebraska (Sprague Street Bridge), and the bridge carrying Colorado State Highway 36 over Box Elder Creek (Box Elder Creek Bridge). For better comparison, the diaphragm beam size for the S.H. 36 bridge was increased in size to better correspond with the

depth of the girders used on the Sprague Street bridge. As may be seen, the cost of a steel diaphragm is approximately 5% more than of that of a cast-in-place diaphragm, which, in comparison to the total cost of the bridge, is negligible because for the bridges considered in the comparison, the diaphragms occur 77 ft on center or greater. Also, a construction man-hour comparison is made between the two types of diaphragms and is shown in Table 6. As is evident, the number of man-hours per foot of diaphragm construction for the steel-diaphragm bridge is only 6% of that for the concrete-diaphragm bridge, which is notable because this would affect the total construction time involved to construct the bridge. Also, for the concrete-diaphragm bridge, it was recommended that the concrete diaphragm be allowed to cure for 7 days (Azizinamini, 2014) prior to placement of the remaining one-third of the diaphragm and the bridge slab; this would not be the case with the scheme using steel diaphragms. Using steel diaphragms attached to full-height stiffeners will completely brace the top flange, whereas in the concrete-diaphragm scheme, the top third of the girder is effectively free to buckle until the concrete has attained some strength.

## CONCLUSIONS

This article presented and discussed simple-made-continuous (SMC) bridges and, in particular, a scheme that uses steel diaphragms in lieu of concrete diaphragms for lateral and torsional restraint over the supporting piers. Based on physical testing, the original detail considered was found to have weaknesses in its compression load transfer

Table 6. Construction Man-Hour Comparison						
Bridge	Sprague over I-680			S.H. 36 over Box Elder Creek		
Element	Quantity	Man-Hours	Total Hours	Quantity	Man-Hours	Total Hours
Formwork	69 SFCA	0.163/SFCA	11.25			
Reinforcing steel placement	0.08 ton	16/ton	1.28			
Cast-in-place concrete	3.19 CY	1.067/CY	3.4			
Sheet steel plate	1	2	2			
W27×84 diaphragms				14.67 ft	0.06/ft	0.9
Total			17.9			0.9
Diaphragm length	10.33 ft			7.33 ft		
Hours/foot	1.73			0.123		

mechanism; these weaknesses were addressed by using direct compression transfer plates. The SMC connection using steel diaphragms was shown to be quicker to construct than other current SMC schemes and more economical and faster to construct than fully continuous girder bridges. Also presented herein was a proposed design methodology based on research performed at Colorado State University.

The testing program described herein had several limitations. The maximum applied load at each end was limited to 200 kips by the capabilities of the lab equipment, and thus, while several elements were taken beyond their capacity, more information would have been gained had the equipment been capable of loading the structure to yield the SMC reinforcing steel. Additionally, the application of more load may also provide additional information on the slab behavior. As noted earlier, further study of the shear lag phenomenon is recommended to evaluate the behavior of the SMC reinforcing bars acting with the shrinkage reinforcing to verify that they have the capability to prevent the center SMC bars from yielding. Also, while an SMC connection using wedge plates for direct transfer of the compression force is in service in Tennessee, wedge plates were not included in this test program. For these reasons, further study/testing encompassing the final connection configuration presented herein is recommended to provide further validation of the proposed design equations.

The research described in this article provides preliminary evidence that a steel SMC connection based on steel diaphragms may be a competitive alternative to a steel SMC bridge with concrete diaphragms. Local labor, material, scheduling concerns and service conditions may contribute to making one alternative more attractive than the other. It is important that designers are aware of this potentially advantageous alternative.

## REFERENCES

- Azizinamini, A. (2005), *Development of a Steel Bridge System-Simple for Dead Load and Continuous for Live Load, Volumes 1 and 2*, University of Nebraska, Lincoln, NE.
- Azizinamini, A. (2014), "Simple for Dead Load-Continuous for Live Load Steel Bridge Systems," *Engineering Journal*, AISC, Vol. 51, No. 2, 2nd Quarter, pp. 59–70.
- Carreira, D.A. and Chu, K.-H. (1985), "Stress-Strain Relationship for Plain Concrete in Compression," *ACI Structural Journal*, ACI, Vol. 82, No. 6, pp. 797–804.
- Farimani, R.S. (2014), "Numerical Analysis and Design Provision Development for the Simple for Dead Load-Continuous for Live Load Steel Bridge System," *Engineering Journal*, AISC, pp. 109–126.
- Johnson, R.I. (2015), *Simple Made Continuous Bridges with Steel Diaphragms: Tension and Compression Transfer Mechanisms*, Colorado State University, Fort Collins, CO.
- NDOR (2001), *Bridge Office Policies and Procedures (BOPP) Manual 200*, NDOR, Lincoln, NE.
- Niroumand, S.J. (2009), *Resistance Mechanism of Simple-Made-Continuous Connections in Skew and Non-Skew Steel Girder Bridges Using Conventional and Accelerated Types of Construction*, University of Nebraska, Lincoln, NE.
- NSBA (2006), "Steel Bridge Uses Simple-Span-Made-Continuous Construction," *Modern Steel Construction*, September, pp. 18–21.
- Talbot, J. (2005), "Simple Made Continuous," *NSBA Steel Bridge News*, October, pp. 1–5.
- Waier, P.R. (2003), *Open Shop Building Construction Cost Data*, R S Means, Kingston, MA.





# Investigation of Web Post Compression Buckling Limit State and Stiffener Requirements in Castellated Beams

FATMIR MENKULASI, CRISTOPHER D. MOEN, MATTHEW R. EATHERTON and  
DINESHA KURUPPUARACHCHI

---

## ABSTRACT

The research presented in this paper addresses the need for a design method to estimate the nominal capacity of castellated beams against concentrated loads. The limit state investigated is that of web post buckling due to compression loads. The purpose of the paper is twofold: (1) to investigate the limit state of web post buckling due to compression loads and (2) to quantify the enhanced capacity of the web post against concentrated loads when stiffeners are provided. Five castellated beam depths are considered, which cover a wide range of the available depths. For each beam section, three load cases are investigated: (1) center of load aligns with the middle of web post, (2) center of load aligns with the center of the hole, and (3) center of load aligns with a point half-way between the center of web post and center of hole. For each load position, two cases are considered: one without a stiffener and one with full-height transverse stiffeners. Each case is investigated using nonlinear finite element analysis to examine the behavior of the web post to failure. The efficiency of stiffeners to increase the resistance of castellated beams against concentrated loads is examined. For each investigated beam depth and stiffener arrangement, the loads that cause failure are noted. In addition, a simplified approach for checking the limit state of web post buckling in compression is proposed.

**Keywords:** castellated beams, web post buckling in compression, stiffeners.

---

## INTRODUCTION

Castellated beams have been used since the 1940s (Zaarour and Redwood, 1996) because of their ability to offer wide and open spaces, reduce floor-to-floor heights, increase illumination, and improve aesthetic appeal. Engineering advantages of castellated beams include superior load deflection characteristics, higher strength and stiffness, lower weight, and the ability to span up to 90 ft without field splicing. Also, the automation process has reduced the cost of their fabrication to the level where, for certain applications, they may be competitive with open-web steel joists (Zaarour and Redwood, 1996). Castellated beams have consisted typically of hexagonal or octagonal openings, with the octagonal openings made possible by the addition of incremental plates between the cut webs. Figure 1 illustrates an

application of castellated beams with hexagonal openings. Another similar form is the cellular beam, which consists of circular web openings. Cellular beams have gained popularity because of the aesthetic appeal they offer in architecturally exposed surfaces. Some manufacturers have recently developed new opening shapes for castellated beams. For example, ArcelorMittal presented castellated beams with sinusoidal web openings, called the Angelina Beam (Wang et al., 2014). Durif and Bouchair (2013) performed an experimental study on beams with such openings. Tsavdaridis and D'Mello (2011, 2012) investigated the behavior of castellated beams with novel, elliptically based web openings.

Castellated beams are subject to a variety of failure modes. Some of the typically investigated failure modes are flexural failure, shear failure, lateral-torsional buckling, Vierendeel mechanism (Figure 2), web post buckling or yielding (Figure 3), local buckling, and welded joint rupture (Figure 4). Pure bending, shear and overall lateral-torsional buckling are similar to the corresponding modes for solid-web beams and can be treated in an almost identical manner if the relevant geometric properties used are based on the reduced cross-section (Soltani et al., 2012). The failure modes that are specific to castellated beams are the Vierendeel mechanism, yielding or buckling of the web post, and fracture of the welded joint. The Vierendeel mechanism is likely to occur in castellated beams with large web-opening lengths under high shear-to-moment ratio. Buckling of the web post can occur due to shear or compression. The buckling or yielding of the web post in shear occurs due to the combination of the shear force acting at mid-depth

---

Fatmir Menkulasi, Assistant Professor, Department of Civil and Environmental Engineering, Wayne State University, Detroit, MI. Email: fmenkula@vt.edu (corresponding)

Cristopher D. Moen, Associate Professor, Department of Civil & Environmental Engineering, Virginia Tech, Blacksburg, VA. Email: cmoen@vt.edu

Matthew R. Eatherton, Assistant Professor, Department of Civil & Environmental Engineering, Virginia Tech, Blacksburg, VA. Email: meather@vt.edu

Dinesha Kuruppuarachchi, Graduate Research Assistant, Department of Civil Engineering, Louisiana Tech University, Ruston, LA. Email: dku003@latech.edu

---

of the web post with a double curvature bending moment over the height of the web post. The buckling of the web post in compression can occur when the web post is subject to concentrated forces. The horizontal shear force can also cause the fracture of the welded joint in the web post, especially in cases when the length of the welded joint is small. Local buckling may occur in three ways in castellated beams: (1) buckling of the compression flange, (2) buckling of the T-section in compression and (3) vertical instability of the sides of the web openings in high shear zones. Ellobdy (2011, 2012) reports that additional failure modes may occur independently or interact with each other.

In many cases, castellated beams are subject to concentrated loads, such as a reaction from a column or a reaction from a supporting girder. The solution in situations like this is typically to provide a stiffener or filler plate (Figure 5) at such concentrated load locations to prevent the buckling of the web post due to compression. However, both of these solutions require additional labor and, in the case of the filler plate, may defeat the aesthetic appeal offered by castellated beams. Additionally, if the advantages of automation are to be fully exploited, such strengthening details must be minimized. The purpose of this paper is twofold: (1) to investigate the limit state of web post buckling due to

compression loads and (2) to quantify the enhanced capacity of the web post against concentrated loads when stiffeners are provided. This is accomplished by performing 30 non-linear finite element analyses, which feature various locations of the concentrated force, castellated beams with and without stiffeners, and various web post height to thickness ratios. In this study, only castellated beams with hexagonal openings are investigated. Additionally, the hexagonal openings feature a specific size relative to the total beam depth. A simplified approach, utilizing an effective web width, is proposed to aid engineers during the design process.

## DESIGN METHODS

At present, there is not a generally accepted design method published in the form of a design guide for castellated beams—primarily because of the complexity of their behavior and the associated modes of failure. Soltani et al. (2012) report that at the European level, design guidance given in Amendment A2 of Eurocode 3 (ENV, 1993): Annex N Openings in Webs was prepared in draft format but was never completed (SCI, 2006). In the United States, while *Design Guide 2* (Darwin, 2003) covers steel and composite beams with web openings, it is explicitly stated that castellated beams are excluded. Various design approaches exist for how to treat failure modes such as Vierendeel mechanism,



Fig. 1. Application of castellated beams (Scherer Steel Structures, Inc.).

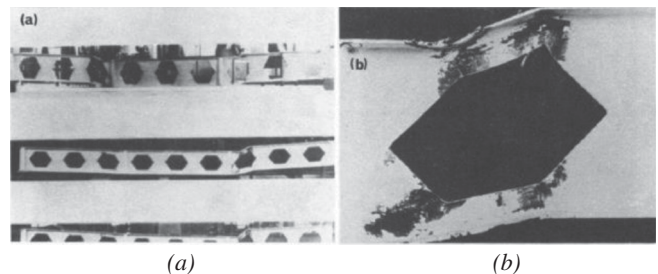


Fig. 2. Vierendeel mechanism caused by shear transfer through perforated web zone (Halleux, 1967): (a) overall view, (b) close-up view of castellation.

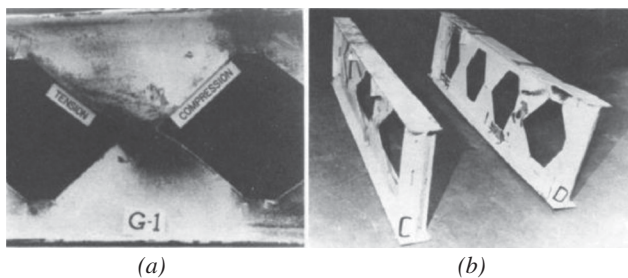


Fig 3. Web buckling: (a) shear compressive half-wave near a support; (b) flexural buckling below a concentrated load (Hosain and Spiers, 1973).

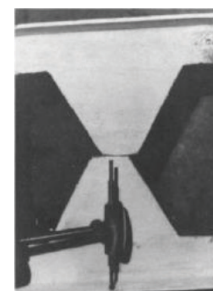


Fig. 4. Rupture of a welded joint (Halleux, 1967).

fracture of a welded joint, and web-post buckling due to the horizontal shear and bending moments. Soltani et al. (2012) provide a summary of these design methods and propose a numerical model to predict the behavior of castellated beams with hexagonal and octagonal openings up to failure. Tsavdaridis and D’Mello (2011, 2012) performed an optimization study on perforated steel beams with various novel web-opening shapes through nonlinear finite element analyses and an investigation on the behavior of perforated steel beams with closely spaced web openings. Zaarour and Redwood (1996) investigated the strength of castellated beams susceptible to web-post buckling due to horizontal shear and bending moments. Wang et al. (2014) examined the Vierendeel mechanism failure of castellated beams with fillet corner web openings.

One of the studies that addresses the resistance of castellated beams against concentrated loads, in addition to the other modes of failure, is the one performed by Hosain and Spiers (1973), in which they tested 12 castellated beams with the objective of investigating the effect of hole geometry on the mode of failure and ultimate strength of such

beams. An attempt was made to study the phenomenon of web buckling due to compression and due to shear in the framework of existing approximate design methods of that time. Three beams failed prematurely due to web buckling, and they either had no stiffeners or partial-depth stiffeners below the concentrated loads. Buckling of the web posts prevented these beams from reaching their maximum capacity. The method proposed by Blodgett (1966) was used to compare the predicted capacity of the web post in compression with the experimentally obtained failure loads. Blodgett’s method treats the nonprismatic solid web as a column having a length equal to the clear height of the hole, a width equal to the web weld length and a thickness equal to the web thickness (Figure 6). To calculate the effective column length ( $kl$ ),  $k$  was assumed to be 1.0.

Kerdal and Nethercot (1984) reviewed previous studies on the structural behavior of castellated beams and identified a number of different possible failure modes. It was concluded that both lateral-torsional instability and the formation of a flexural mechanism may be handled by an adaption of established methods for plain webbed beams, provided

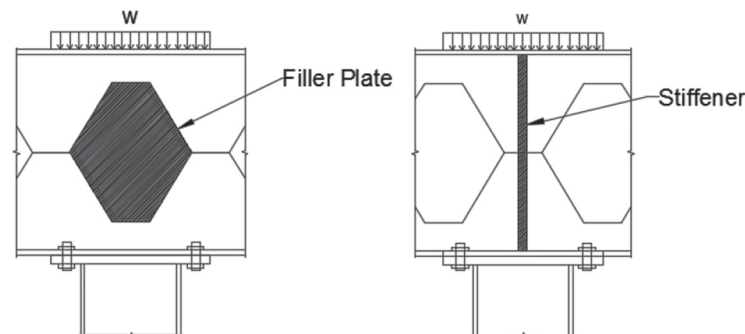


Fig. 5. Reinforcing techniques for castellated beams subject to concentrated loads.

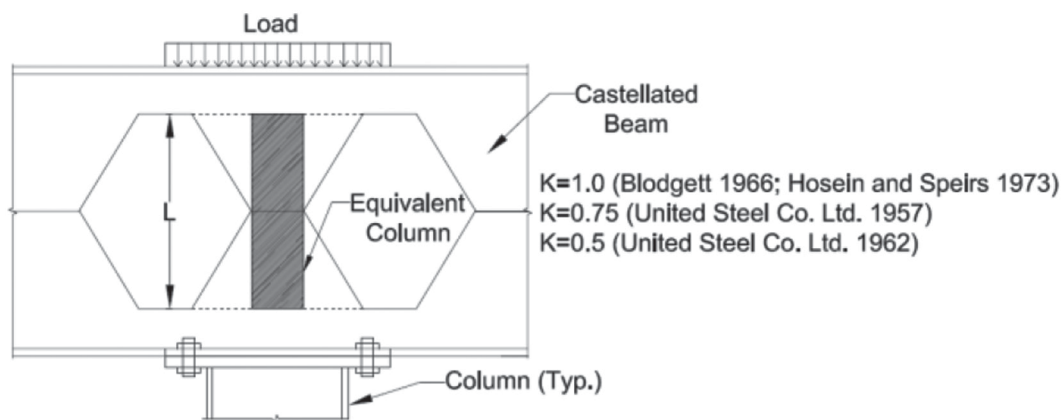


Fig. 6. Simplified equivalent column approach for the investigation of the limit state of web post buckling in compression.

Table 1. Investigated Castellated Beams (CB)						
W Section	CB Section	$h_{wcb}/t_w$	Section Length ( $S^{**}$ ) (in.)		Aspect Ratio ( $S/d_g^{**}$ )	
			A*, B*	C*	A*, B*	C*
W8×40	CB12×40	27.7	11.5	5.75	1	0.50
W12×50	CB18×50	44.7	15.0	7.50	0.83	0.42
W16×50	CB24×50	62.0	19.0	9.50	0.77	0.39
W21×62	CB30×62	76.7	23.0	11.5	0.76	0.38
W27×84	CB40×84	89.6	30.0	15.0	0.74	0.37

\*Load position (Figure 7). \*\*See Table 2.

that the cross-sectional properties are those corresponding to the centerline of castellation. It was also concluded that the methods available at that time for the determination of collapse in the other modes, while rather less accurate, were adequate for design except in the case of web post buckling in compression. Kerdal and Nethercot state that while the web post could be considered to be a column having the depth of the hole and the area of the welded joint, there does not seem to be an agreement as to which effective length of the column to use. For example, an effective length factor of 0.75 was used in the study by the United Steel Co. Ltd. (1957). This was later (1962) reduced to 0.5 in a report by the same agency. Finally, Hosain and Spiers (1973) assumed the web posts to be pinned at both ends. Accordingly, one of the conclusions in the report by Kerdal and Nethercot is that no satisfactory method has been identified for the prediction of the load causing vertical buckling of the web post under a concentrated load or at a reaction point. As a result, this failure mode was reported as an area of uncertainty in the design of castellated beams, and there is a need to obtain a better idea as to what is the effective area of the column and its effective length.

In the light of this discussion, the investigation described in this paper was undertaken with the goal of investigating the capacity of castellated beams under concentrated loads using nonlinear finite element analysis and models that specifically address this condition by isolating the beam sections from the other modes of failure.

### RESEARCH APPROACH

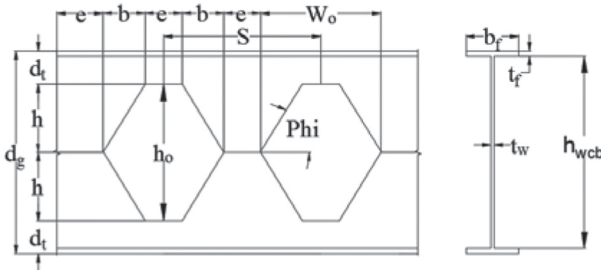
To investigate the capacity of castellated beams when they are subject to concentrated loads, five beam depths were selected (Table 1). Next to each castellated beam section is provided the original wide flange beam used to fabricate the castellated beams. These beams were selected such that they covered a wide range of depths so that the capacity of each section against concentrated loads, with and without stiffeners, could be investigated. In cases when castellated beam sections feature stiffeners, the thickness of the stiffener was

always 0.5 in. The web clear height to thickness ratios for these five beams range from 27.7 to 89.6. Table 2 provides a summary of the information used to define the geometry of the castellated beams. Each beam depth was subject to compressive loads at the top flange (Figure 7). The compression load was applied in the form of a uniformly distributed load over the length of the castellated beam section under consideration. Three load locations were investigated: (A) centered over the web post, (B) centered over the hole, and (C) centered midway between the center of the hole and the center of the web post. These load positions are identified as A, B and C, respectively, and cover the potential concentrated load positions that castellated beams will be subject to. The castellated beam section lengths for each of these three load cases are provided in Table 1 together with the aspect ratio between the section length,  $S$ , and the overall depth of the beam,  $d_g$ . The top flange of the castellated beam specimens was restrained against translations in directions 1 and 3 and against rotations about all three axes to simulate out-of-plane lateral bracing, the restraint provided by the rest of the beam, and the restraint provided by the slab or any other supported member. The top flange was free to translate in the vertical direction to accommodate the application of the load. The bottom flange was restrained against all translations and rotations. The restraint provided by the continuation of the beam to the vertical edges of the webs was conservatively ignored, and these edges were modeled as free. As stated earlier, the five selected beams were investigated for the case when their webs are unreinforced and reinforced with full-height bearing stiffeners.

The concentrated loads were assumed to apply over the supports. This loading arrangement is believed to be the most critical for the limit state of web post buckling in compression, compared to other cases when the concentrated loads are applied away from the supports. To demonstrate this, a simply supported castellated beam was analyzed once with a concentrated load applied at mid-span and another time with a concentrated load applied over the left support. Figure 8 illustrates the orientation and magnitude of principal compressive stresses for both cases. When the load is



**Table 2. Geometry of Investigated CBs**



CB Section	e (in.)	b (in.)	d <sub>t</sub> (in.)	d <sub>g</sub> (in.)	t <sub>w</sub> (in.)	b <sub>f</sub> (in.)	t <sub>f</sub> (in.)	S (in.)	h <sub>o</sub> (in.)	h (in.)	W <sub>o</sub> (in.)	Phi (deg)
CB12×40	4.0	1.75	2.50	11.5	0.375	8.125	0.563	11.5	6.50	3.25	7.50	61.70
CB18×50	4.5	3.25	3.25	18.0	0.375	8.125	0.625	15.0	11.375	5.75	10.75	60.27
CB24×50	4.5	5.00	4.00	24.5	0.375	7.125	0.625	19.0	16.50	8.25	14.50	58.81
CB30×62	6.0	5.50	6.00	30.0	0.375	8.250	0.625	23.0	18.00	9.00	17.00	58.54
CB40×84	7.0	8.00	6.50	40.5	0.438	10.00	0.625	30.0	27.375	13.75	23.00	59.74

applied at mid-span, the magnitude of the principal compressive stresses in the region underneath the load is 10.6 ksi at most. The orientation of the principal compressive stresses is vertical in the region immediately underneath the load and becomes more inclined and horizontal toward the bottom section of the beam. This is expected because the load is finding its way toward the supports. The maximum principal compressive stress occurs at the right support and is 14.4 ksi. When the load is applied over the left support, the

magnitude of the maximum compressive stress is 14.1 ksi, which is higher than the magnitude of principal compressive stresses underneath the load when the load was applied at mid-span, even though the width of web post at mid-height of the beam section is higher than the width at mid-span. This demonstrates that the most critical loading condition as it pertains to the limit state of web post buckling in compression is when the load is applied directly over the support.

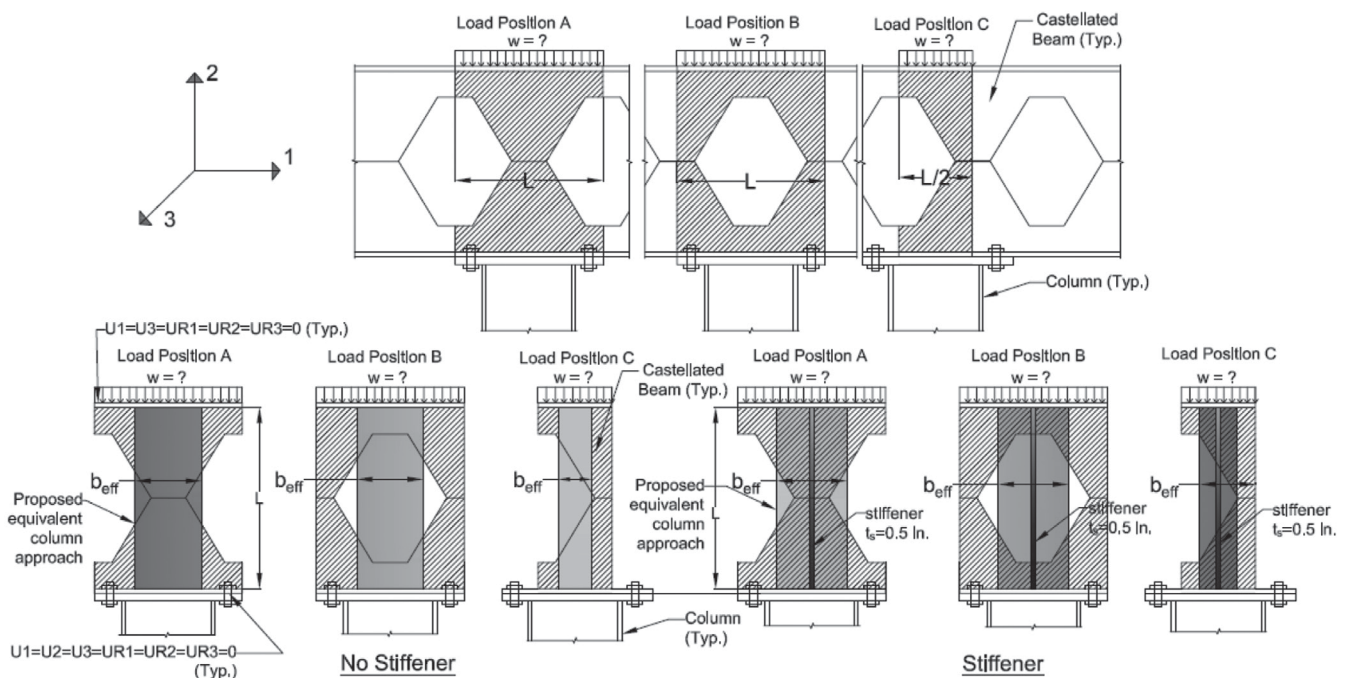


Fig. 7. Investigated cases.

Thirty nonlinear finite element analyses were performed to obtain failure loads for the investigated specimens and to propose a simple design methodology that is based on the concept of an effective web width.

### FINITE ELEMENT ANALYSIS

The numerical simulations described in this paper were performed by using the commercially available finite element analysis software Abaqus (Dassault Systemes, 2014). Because the primary goal of this investigation is the buckling of the web under concentrated loads, flanges were modeled as rigid bodies. The webs and stiffeners were modeled using S8R5 shell elements. The S8R5 element is a doubly curved thin-shell element with eight nodes, and it employs quadratic shape functions. The “5” in S8R5 denotes that each element has five degrees of freedom (three translational, two rotational) instead of six (three translational, three rotational). The rotation of a node about the axis normal to the element mid-surface is removed from the element formulation to improve computational efficiency (Moen, 2008). The

“R” in the S8R5 designation denotes that the calculation of the element stiffness is not exact; the number of Gaussian integration points is reduced to improve computational efficiency and avoid shear locking (Moen, 2008). This element is designed to capture the large deformations and through-thickness yielding expected to occur during the out-plane buckling of the web post to failure. The size of the mesh was selected such that each element side did not exceed 0.5 in. in length and was determined based on results from convergence studies to provide a reasonable balance between accuracy and computational expense. It was assumed that the self-weight of the specimens was negligible compared to the applied loads. Although the cross-sections were symmetrical about the major axis, it was necessary to model the full cross-section because the buckled shape could be nonsymmetrical.

The finite element model takes into account both material and geometric nonlinearities. The structural steel was modeled using a bilinear stress-strain relationship based on coupon test data provided by Arasaratnam et. al (2011). The true stress versus true strain relationship is shown in

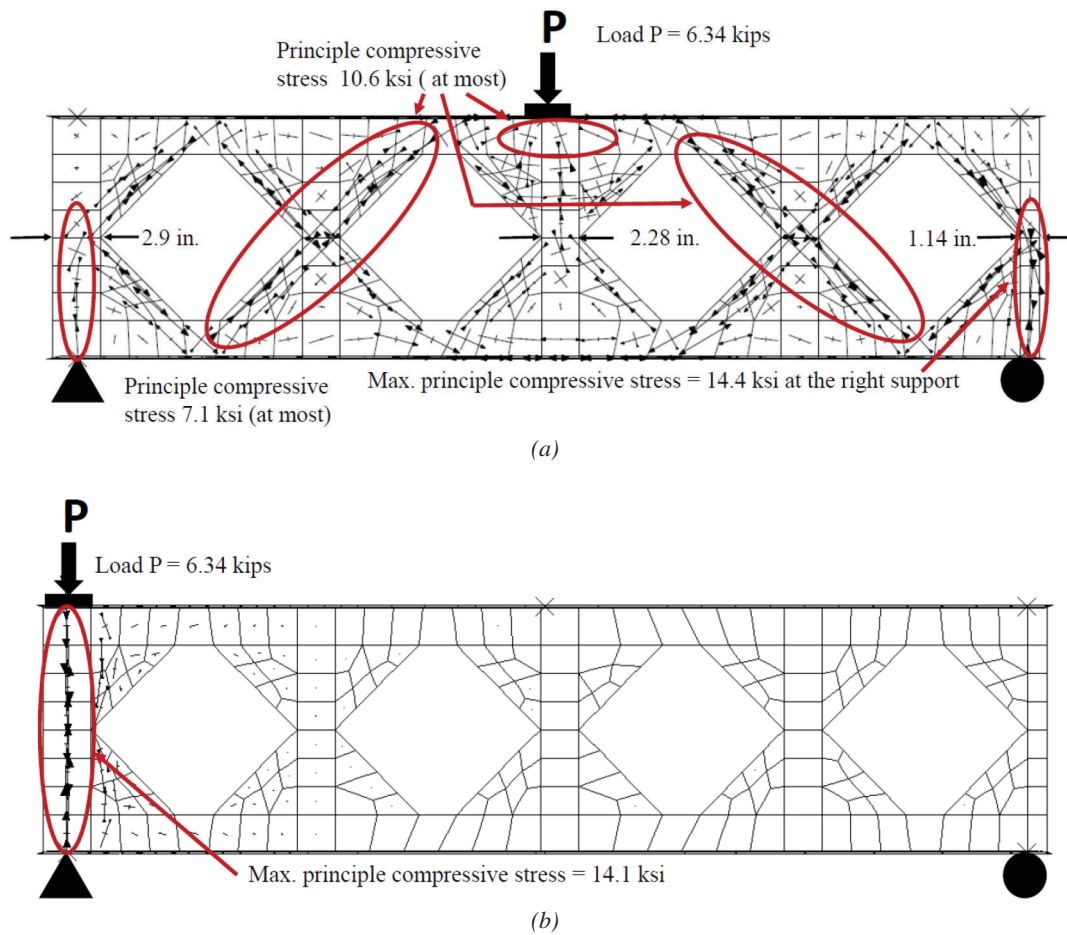


Fig. 8. Orientation and magnitude of principle compressive stresses: (a) load near mid-span; (b) load over left support.

Figure 9 and was input into Abaqus to define the limits of the Von Mises yield surface. Young's modulus,  $E$ , was set at 29,000 ksi, and Poisson's ratio,  $\nu$ , was set to 0.3. To initiate buckling, an initial, small, out-of-plane geometric imperfection—in the form of the first mode shape obtained from an eigenvalue buckling analysis—was imposed to the model. An Abaqus.fil file is created for each eigenbuckling analysis, which is then called from the nonlinear.inp file with the \*IMPERFECTION command. During the design phase, the imperfections are typically unknown and are accounted for in the design equations used to estimate the capacity of the members. They are usually used as general random quantities that can be rigorously treated by stochastic techniques (Soltani et al., 2012). In their investigation, Soltani and colleagues state that according to their knowledge, no consensus exists on maximum imperfection magnitudes for castellated beams even when the imperfection is in the shape of the lowest eigenmodes. Two imperfection magnitudes were used in the study performed by Soltani et al.— $d_w/100$  and  $d_w/200$ , where  $d_w$  is the clear web depth between the flanges—and it was shown that the model was not significantly affected by a change in the magnitude of the initial lateral deflection taken in the shape of the lowest buckling mode. Accordingly, the magnitude of the initial imperfection employed in this study is  $h_{cbw}/100$  [where  $h_{cbw}$  is the clear height of the web (see Table 2) and is the same as  $d_w$  used by Soltani et al.]. Material nonlinearity is simulated in Abaqus with classical metal plasticity theory, including the assumption of a Von Mises yield surface. In this study, residual stresses are not considered.

The modified Riks method was used to determine the nonlinear response of the castellated beam section. The modified Riks method (i.e., \*STATIC,RIKS in Abaqus),

was developed in the early 1980s and enforces an arc length constraint on the Newton-Raphson incremental solution to assist in the identification of the equilibrium path at highly nonlinear points along the load-deflection curve (Crisfield, 1981). The loads are applied uniformly along the length of the web and stiffeners when applicable. As stated earlier, top and bottom flanges were modeled as rigid bodies with reference nodes at the centroid of each flange (Figure 10). For each case, the vertical displacement at the reference node of the top flange and the reaction at the reference node of the bottom flange were recorded. The maximum vertical displacement at the reference node of the top flange was typically limited to 2 in. because such a vertical displacement corresponded with loads that were much lower than the peak load and were well into the descending branch of the load displacement curve. A 2-in. vertical displacement provides the opportunity to investigate the full behavior to failure and determine the reserve capacity of the section once the peak load is achieved and the beam continues to deform. Also, when the vertical displacement is 2 in., the deformed configuration of the beam web can be clearly seen. Additionally, a 2-in. vertical displacement helps examine the efficiency of various stiffener arrangements in terms of post-peak-load-carrying capabilities.

To validate the modeling approach, the failure loads for seven beam tests performed by Chen and Oppenheim (1974) and Chen and Newlin (1973) were compared to the failure loads obtained from finite element analyses. The tests were performed on solid web beam sections, which were compressed on both flanges until the web buckled. This loading setup is similar to the loading condition described in this study for castellated beams. The results for these beam tests were used to develop the current AISC *Specification*

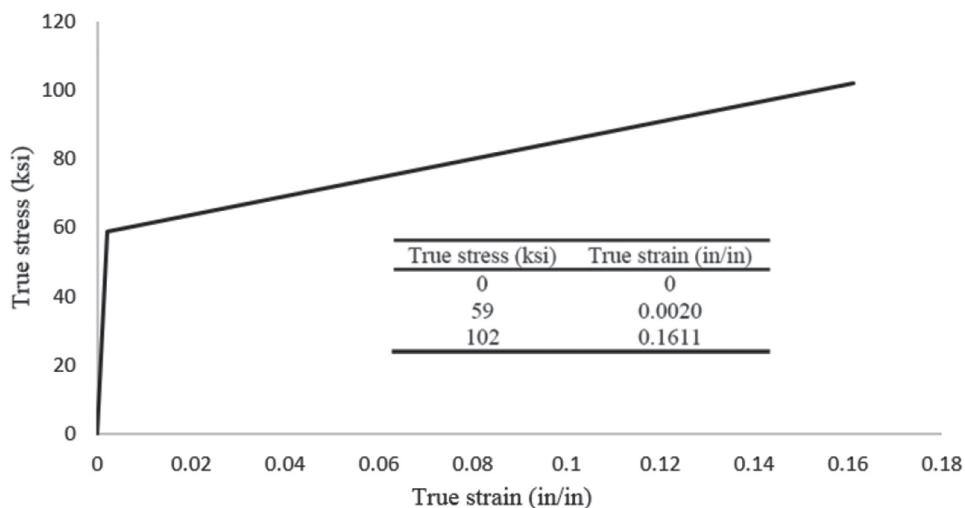


Fig. 9. True stress-strain curve based on data from Arasaratnam et al. (2011).



**Table 3. Comparison of Web Compression Buckling Capacities**

Case No.	Reference	Section	$P_{test}$ (kips)	$P_{FEA}$ (kips)	Ratio = $\frac{P_{ult}(Test)}{P_{ult}(FEA\ fixed)}$
1	Chen & Oppenheim (1974)	W10×30	90	81	1.11
2	Chen & Oppenheim (1974)	W10×39	253	232	1.09
3	Chen & Newlin (1973)	W12×27	64	59	1.09
4	Chen & Oppenheim (1974)	W12×30	61	64	0.95
5	Chen & Newlin (1973)	W12×45	166	146	1.14
6	Chen & Newlin (1973)	W12×45	260	274	0.95
7	Chen & Oppenheim (1974)	W12×45	168	153	1.10
Average					1.06

equation for the web compression buckling limit state in Section J10.5 (AISC, 2010). Additional information on the applicability of the AISC web-buckling provisions to the castellated beams is provided later in this paper. A summary of the experimentally obtained failure loads and those computed using finite element analysis is provided in Table 3. The average ratio between the peak load obtained from the tests and that obtained from finite element analyses is 1.06. This suggests that the modeling approach used in this study provides reliable results with respect to being able to predict the buckling capacity of the web.

### RESULTS

Figure 10 shows the first buckled mode shapes for CB12×40 when it is unreinforced and reinforced with stiffeners. As expected, the first buckled mode shape for the unreinforced cases is a typical out-of-plane buckling of the castellated beam web. For the reinforced cases, the first buckled mode shape featured a combination of web and stiffener buckling for load cases A and C and only web buckling for load case B. This was due to the fact that although the stiffener in load case B was located such that it aligned with the center of the load, the web post was the weakest element, and it buckled first. This behavior is similar to local buckling when, in a given cross-section, one element is more susceptible to buckling than the rest of the elements.

Figure 11 shows the deformed shape at simulated failure for all five cases investigated using CB12×40. As stated earlier, simulated failure corresponds to a vertical displacement of 2 in. in the reference node of the top flange. As expected, in all cases, the deformed shape at failure is an exaggeration of the first buckled mode shape. Even for load case B when the section is reinforced with a stiffener, due to deformation compatibility, the stiffener is eventually engaged in the resistance against the applied load. It should be noted that because the stiffeners could only be minimally attached to

the web for load position B, the stiffener buckled in a flexural mode. For load position A, the stiffeners were fully attached to the web, which resulted in a buckling mode that featured translation and rotation.

Figure 12 illustrates the uniform load versus vertical displacement relationship for all investigated cases. Five graphs are presented, with each graph illustrating the results pertaining to each castellated beam section. The uniform load is obtained by dividing the reaction obtained at the reference node of the bottom flange with the section length provided in Table 1. This was done to make a consistent comparison among all three load cases considered, given that the castellated beam section length for load case C is half of that considered in load cases A and B. The vertical displacement is obtained at the reference node of the top flange, and the analysis was typically stopped when this value reached 2 in. As can be seen, all three unreinforced cases behaved similarly, and the load displacement curves are almost identical. This is expected and intuitive because the effective section resisting the applied load per unit length is the same. The peak uniformly distributed loads for each case are summarized in Table 4. It can be observed that for all cases, the peak load decreases as the section depth increases. This is also expected and intuitive because the higher the unbraced length against buckling the lower the peak load.

The presence of stiffeners increases significantly the capacity of the castellated beam sections against concentrated loads. In almost all cases, the highest resistance is provided by load case C when it is reinforced with a stiffener. This is due to the fact that even though the section length and the applied load were both half of those considered in cases A and B, the stiffener size was kept constant. Accordingly, reinforced load case C benefited relatively more from the presence of the stiffener. It can also be observed that the slope of the descending branch of the load displacement curve is smaller in reinforced load case A compared to reinforced load cases B and C. This occurs because, for load

Table 4. Uniformly Distributed Failure Load, $w_n$ (kip/in.)										
Load Position	CB12x40		CB18x50		CB24x50		CB30x62		CB40x84	
	No Stiffener	Stiffener	No Stiffener	Stiffener	No Stiffener	Stiffener	No Stiffener	Stiffener	No Stiffener	Stiffener
A	6.8	28.5	3.7	23.3	2.3	17.4	1.8	16.9	1.6	16.0
B	6.5	23.0	3.6	17.7	2.2	12.9	1.8	9.4	1.5	5.0
C	6.5	46.7	3.6	35.9	2.2	24.0	1.8	22.0	1.5	15.9

case A, the stiffener was placed where it was needed the most, which is at the center of the web post. The center of the web post in all three cases is the section that is most susceptible to web buckling.

The uniformly distributed load applied to the castellated beam sections was also normalized with respect to the uniformly distributed load that causes yielding at the smallest cross-section along the height of the web (mid-height of web) to investigate the efficiency of the sections in resisting the applied load (Figure 13). Figure 13 suggests that as the sections get deeper, the effect of web slenderness becomes more pronounced in the unstiffened castellated beams. Also, in all stiffened cases and load position A, the failure load is equal to or slightly higher than the yield load, which once again highlights the efficiency of the stiffener for this load

position. The reason the failure load is slightly higher than the yield load in some cases is attributed to strain hardening.

In all cases, the presence of the stiffeners enhances the capacity of the section significantly. Stiffened cases with load position C yielded lower ratios than those with load position A but higher ratios than those with load position B. This again suggests the relative inefficiency of the stiffener location for load position B. The lower normalized values for the peak load obtained for load position B are partially attributed to the fact that the stiffener was only minimally attached to the web at the top and bottom portions of the beam. As mentioned earlier, this led to a flexural buckling mode for the stiffener about its minor axis. In contrast, for load position A, the stiffener was fully attached to the web, which positively influenced its efficiency in resisting the applied load.

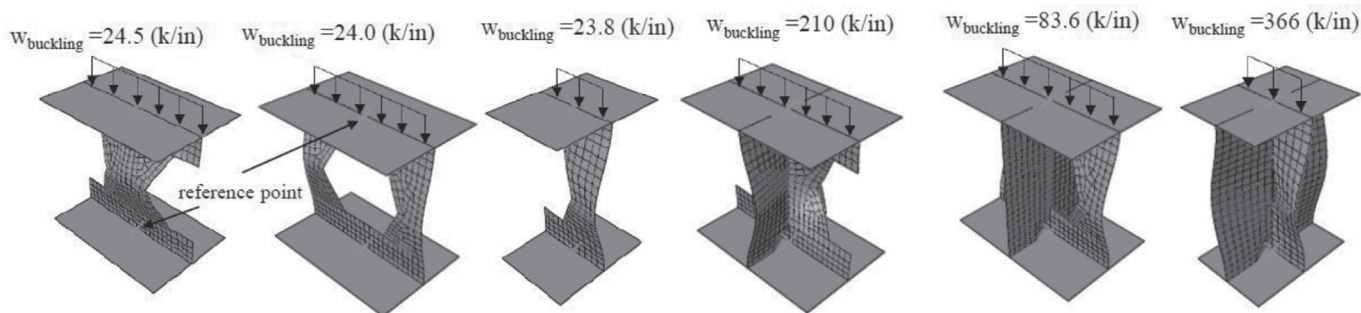
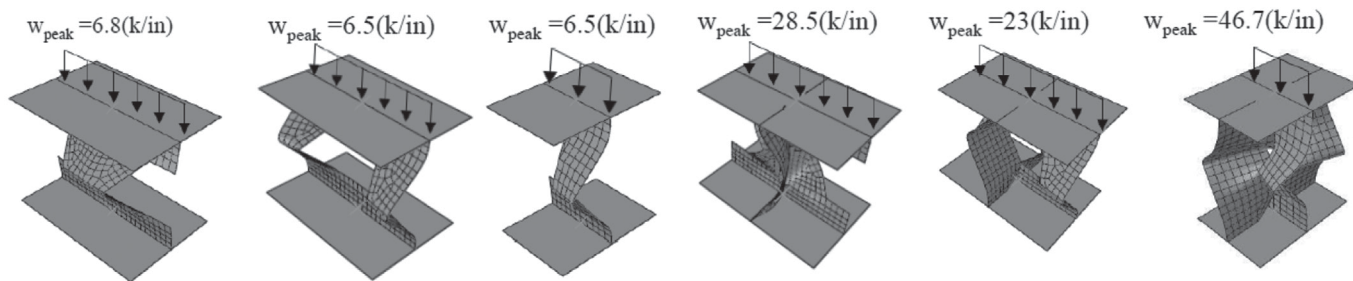


Fig. 10. First buckled mode shape for CB12x40.



Note: The deformed shape corresponds with a vertical deflection of 2 in. at the reference point of the top flange

Fig. 11. Deformed shape at failure for CB12x40.

The total reaction that corresponded with the peak load obtained at the reference point of the bottom flange was compared with the predicted nominal strength of an equivalent solid web beam section calculated based on AISC *Specification* Section J10 (Table 5) (AISC, 2010). Only the unreinforced sections were included in this comparison, and only articles J10.2 (web local yielding), J10.3 (web crippling) and J10.5 (web compression buckling) were considered because the investigated sections were adequately braced against out-of-plane translations at the top and bottom flanges. The web local yielding provisions (Eqs. 1 and 2) apply to both

compressive and tensile forces of bearing and moment connections. These provisions are intended to limit the extent of yielding in the web of a member into which a force is being transmitted (AISC, 2010). The bearing length,  $l_b$ , in all cases was taken equal to the section length (Table 1), and  $k$  was taken as zero because the fillet between the web and the flange was not included in the finite element model. The web crippling provisions (Eqs. 3, 4 and 5) apply only to compressive forces, which is consistent with the cases investigated in this study. Web crippling is defined as crumpling of the web into buckled waves directly beneath the load, occurring

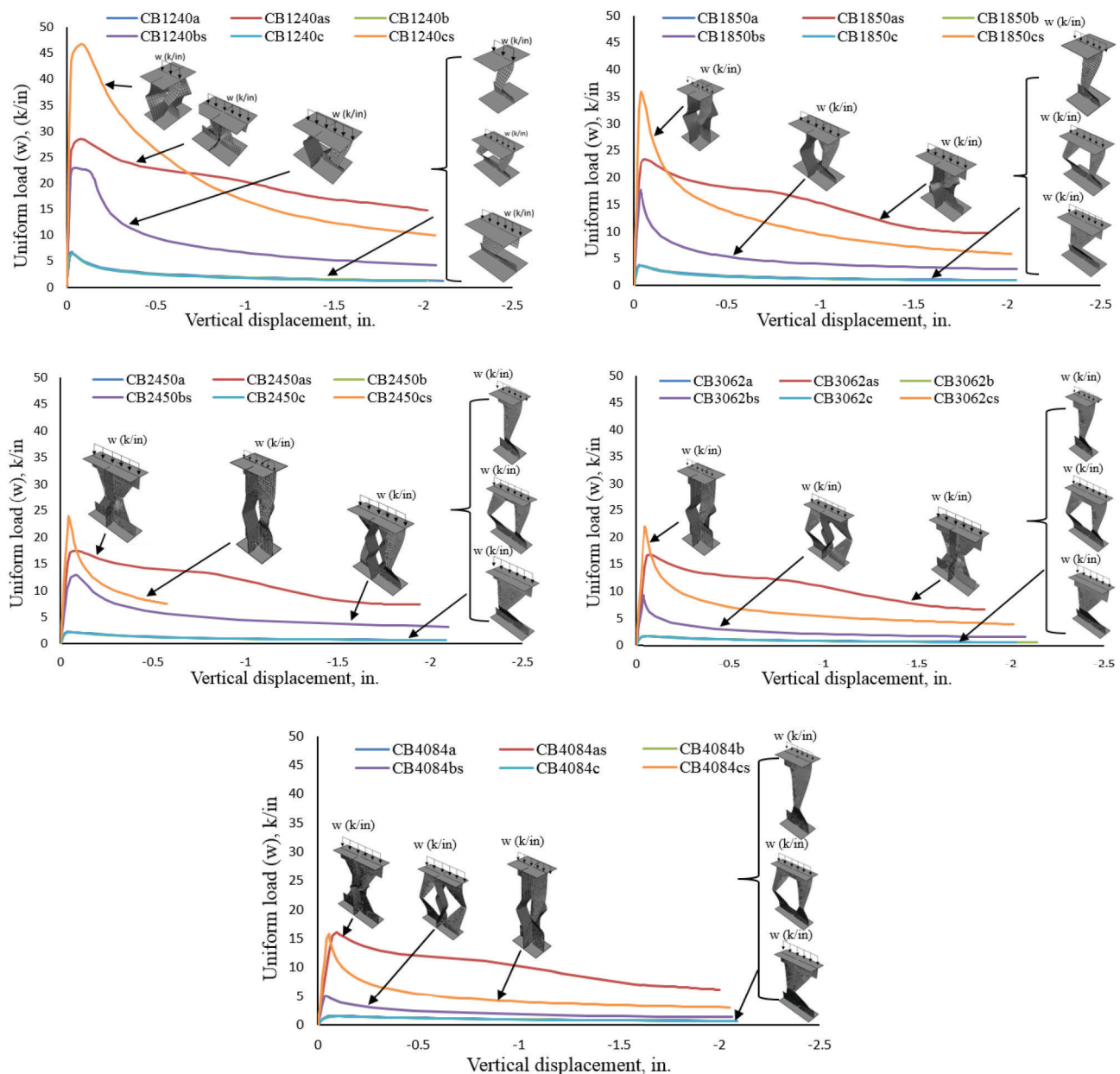


Fig. 12. Uniform load versus vertical displacement at the top of the web post.

in more slender webs, whereas web local yielding is yielding of that same area, occurring in stockier webs (AISC, 2010). The web compression buckling provisions (Eqs. 6 and 7) apply only when there are compressive forces on both flanges of a member at the same cross-section, which is also consistent with the cases investigated in this study. Equation 6 is predicated on an interior member loading condition, and in the absence of applicable research, a 50% reduction has been introduced for cases wherein the compressive forces are close to the member end (Eq. 7) (AISC, 2010).

Equation 6 was developed by Chen and Newlin (1973) during a study on the column web-buckling strength in beam-to-column connections. Equation 6 was derived by using the critical buckling stress of a square plate simply supported on all sides and by adjusting it to fit the results from the most critical test. Figure 14 shows the test setup. Because the investigation was focused on beam-to-column connections, Chen and Newlin state that from observations of the test results in the present and previous tests, it appears justified to assume that the concentrated beam-flange load acts

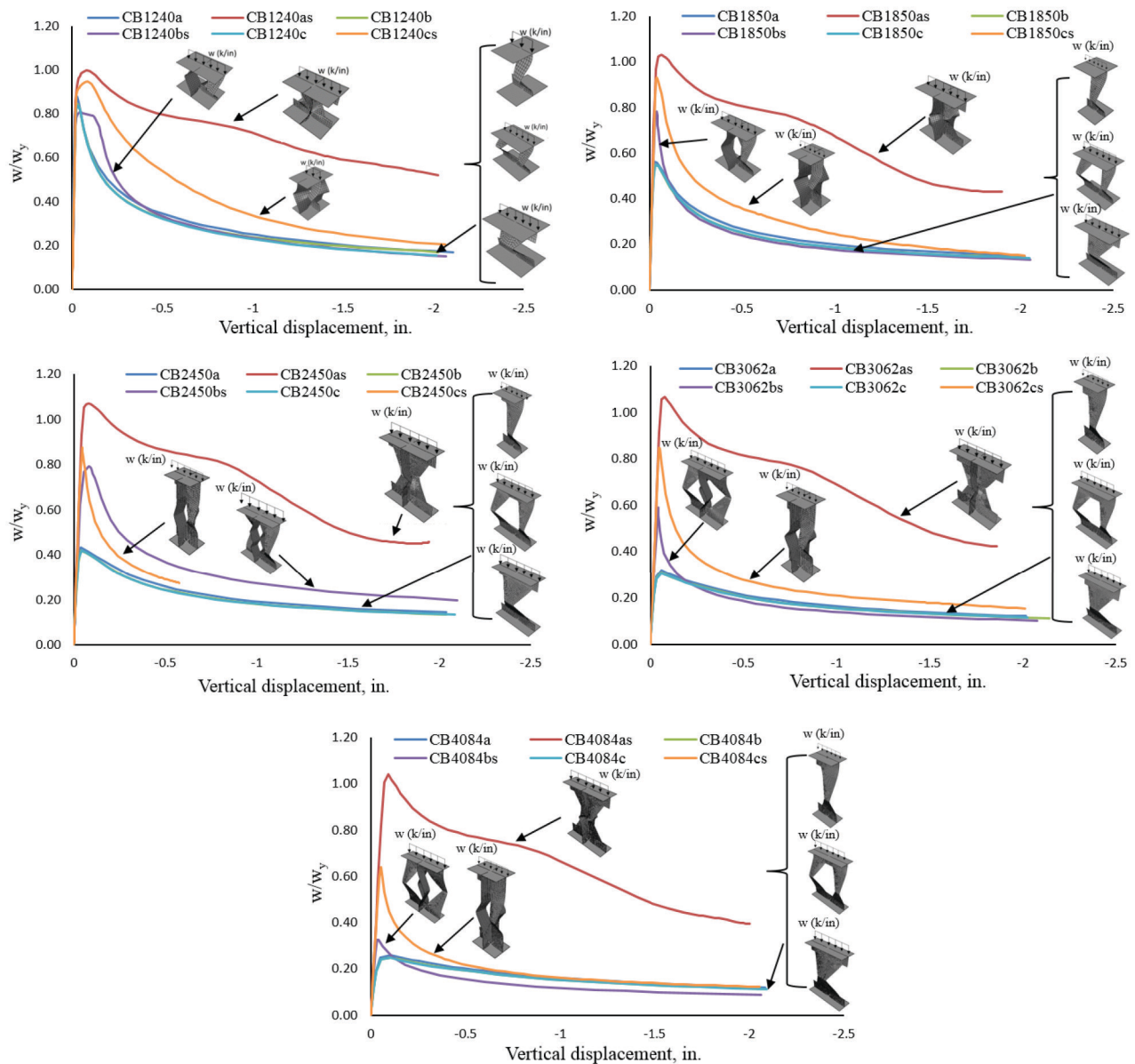


Fig. 13. Normalized uniform load versus vertical displacement at the top of the web post.



on a square panel whose dimensions are  $d_c \times d_c$ , where  $d_c$  is the column web depth.

In all cases in which the load was assumed to be away from member ends, the limit state of web compression buckling controlled, with the exception of C12×40 load case C, in which web local yielding controlled over the other limit states. When the load was assumed to be at member ends, the limit state of web compression buckling controlled in all cases. Accordingly, this was primarily an evaluation of the applicability of Equations 6 and 7. Equations 6 and 7 are used to predict web compression buckling in solid web beams as a function of web thickness,  $t_w$ , modulus of elasticity,  $E$ , web yield stress,  $F_{yw}$ , and clear distance between flanges less the fillet,  $h$ . Because these equations were derived assuming that the load is applied over a length equal to the depth of the web, they do not distinguish between various load bearing lengths.

Equation 6 grossly overestimated the nominal strength of the castellated beam sections against concentrated loads when the loads were assumed to be away from the member ends. This was expected for several reasons. Equation 6 was developed for solid web beams and does not take into consideration the presence of the holes. Additionally, in the cases investigated in this study, the restraint provided by the continuation of the castellated beam to the web on both sides (if applicable) was conservatively ignored, whereas in the derivation of Equation 6, the square web panel was assumed to be simply supported on all sides. Also, the aspect ratio between the loaded length and member depth was, at best, 1.0 (Table 1). The combination of lower than 1.0 aspect ratios between the loaded length and the depth of the castellated beam, especially for load position C, and the fact that no restraint was assumed on the sides of the beam, resulted in computed capacities lower than those predicted by AISC equations for web compression buckling.

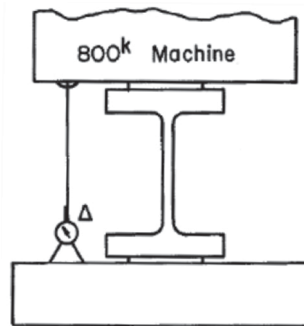


Fig. 14. Test setup used by Chen and Newlin to investigate web-buckling strength (1973).

When the load was assumed to be at member ends (Eq. 7), the prediction improved, especially for load cases A and B. This is also expected because when the load is applied at member ends, the restraint provided by the continuation of the castellated beam to the web applies only to one end, and it represents more closely the boundary conditions used in this study. For load case C, the equation still grossly overestimated the strength of the castellated beam sections because it does not take into account the shorter loaded length and the lower aspect ratios.

The average between the peak load obtained from nonlinear finite element analysis and that obtained from the AISC web buckling provisions, assuming that the load is at member ends, was 1.16 for load position A and B and 0.57 for load position C.

#### Web Local Yielding

*Away from member ends*

$$R_n = F_{yw}t_w(5K + l_b) \quad (1)$$

*At member ends*

$$R_n = F_{yw}t_w(2.5K + l_b) \quad (2)$$

where

$t_w$  = web thickness, in.

$F_{yw}$  = web yield stress (59 ksi)

$k$  = distance from outer face of the flange to the web toe of the fillet, in.

$l_b$  = length of bearing, in.

#### Web Local Crippling

*Away from member ends*

$$R_n = 0.80t_w^2 \left[ 1 + 3 \left( \frac{l_b}{d} \right) \left( \frac{t_w}{t_f} \right)^{1.5} \right] \sqrt{\frac{EF_{yw}t_f}{t_w}} \quad (3)$$

*At member ends*

for  $l_d/d \leq 0.2$

$$R_n = 0.40t_w^2 \left[ 1 + 3 \left( \frac{l_b}{d} \right) \left( \frac{t_w}{t_f} \right)^{1.5} \right] \sqrt{\frac{EF_{yw}t_f}{t_w}} \quad (4)$$

for  $l_d/d > 0.2$

$$R_n = 0.40t_w^2 \left[ 1 + \left( \frac{4l_b}{d} - 0.2 \right) \left( \frac{t_w}{t_f} \right)^{1.5} \right] \sqrt{\frac{EF_{yw}t_f}{t_w}} \quad (5)$$

where

$E$  = modulus of elasticity (29,000 ksi)

$d$  = full nominal depth of the section, in.

$t_f$  = thickness of flange, in.

**Table 5. Comparison of Predicted Failure Loads**

	Load Position	FEA* (kips)	AISC** (kips)		Ratio = FEA/AISC	
			Away from Member Ends	At Member Ends	Away from Member Ends	At Member Ends
CB12×40	A	77.8	172.6	86.3	0.45	0.90
	B	74.6	172.6	86.3	0.43	0.86
	C	37.2	127.2***	86.3	0.29	0.43
CB18×50	A	56.0	105.3	52.7	0.53	1.06
	B	54.6	105.3	52.7	0.52	1.04
	C	27.2	105.3	52.7	0.26	0.52
CB24×50	A	43.1	73.8	36.9	0.58	1.17
	B	41.7	73.8	36.9	0.57	1.13
	C	20.8	73.8	36.9	0.28	0.56
CB30×62	A	42.3	59.6	29.8	0.71	1.42
	B	41.0	59.6	29.8	0.69	1.38
	C	20.4	59.6	29.8	0.34	0.68
CB40×84	A	47.1	69.2	34.6	0.68	1.36
	B	45.1	69.2	34.6	0.65	1.30
	C	22.5	69.2	34.6	0.33	0.65
					Average of A and B	1.16
					Average of C	0.57
* Nominal capacity computed from nonlinear finite element analysis.						
** Nominal strength calculated based on AISC <i>Specification</i> Sections J10.2, J10.3 and J10.5. Typically governed by J10.5 (web compression buckling unless otherwise noted).						
*** Governed by web local yielding.						

**Web Compression Buckling**

*Away from member ends*

$$R_n = \frac{24t_w^3 \sqrt{EF_{yw}}}{h} \quad (6)$$

*At member ends*

$$R_n = \frac{12t_w^3 \sqrt{EF_{yw}}}{h} \quad (7)$$

where

$h$  = clear distance between flanges less the fillet

**PROPOSED SIMPLIFIED APPROACH**

The results from nonlinear finite element analyses were used to calculate an effective web width for castellated beams with and without bearing stiffeners. For cases in which the castellated beams had no stiffeners, the web post was treated as a rectangular column with a height equal to the clear height of the web ( $h_{web}$ ) and an effective width ( $b_{eff}$ )

(Figure 15) that was calculated using an iterative procedure such that the axial load capacity of the rectangular column matched that calculated from finite element analyses of the corresponding castellated beam section. The nominal axial strength of the rectangular column was calculated using AISC *Specification* Section E3 (2010) and was determined based on flexural buckling of the effective portion of the web. The rectangular column was assumed fixed at both ends and braced against out-of-plane translations at both top and bottom flanges.

For cases in which the castellated beams featured transverse stiffeners, the web post was treated as a column with a cruciform cross-sectional shape consisting of the web and the stiffeners (Figure 15). The effective width of the web ( $b_{eff}$ ) was again calculated iteratively such that the nominal axial strength of the column with the cruciform cross-sectional shape calculated based on AISC *Specification* Sections E3 and E4 (2010) matched with the peak load calculated from finite element analyses of the corresponding castellated beam section. In this case, the nominal strength of the equivalent column section was always controlled by the torsional buckling mode. The column with the cruciform

Load Position	CB12×40		CB18×50		CB24×50		CB30×62		CB40×84	
	No Stiffener	Stiffener	No Stiffener	Stiffener	No Stiffener	Stiffener	No Stiffener	Stiffener	No Stiffener	Stiffener
A	4.29	5.63	4.24	7.48	5.28	7.74	7.93	12.17	10.36	13.28
B	4.11	2.37	4.14	2.63	5.11	2.70	7.68	2.11	9.91	1.86
C	2.05	2.58	2.06	2.84	2.55	2.30	3.82	2.58	4.94	2.38

cross-sectional shape was assumed fixed at both ends and braced against out-of-plane translations at both top and bottom flanges.

The calculated effective widths for unstiffened and stiffened cases are provided in Table 6 for all CB sections considered. These effective web widths will allow the engineer to check the limit state of web post buckling due to compression by treating unstiffened webs as rectangular columns and stiffened webs as columns with a cruciform cross-sectional shape. The nominal strength of these equivalent columns can then be calculated based on the AISC *Specification* (2010). The equivalent rectangular column can be designed in accordance with AISC *Specification* Section E3, and the equivalent column with the cruciform cross-sectional shape can be designed in accordance with Sections E3 and E4. In this approach, the effects of local buckling for the cruciform cross-sectional shape need not be considered because the effective width was computed to match the results from nonlinear finite element analysis, which account for local buckling effects. The height of the equivalent columns is taken equal to clear height of the web ( $h_{wcb}$ ) of the castellated beam. This height is different from that used in design approaches proposed by other investigators (Blodgett, 1966;

United Steel Co. Ltd., 1957, 1962; Hosain and Spiers, 1973), in which the height of the column was taken equal to clear height of the hole. After examining the deformed shapes of the castellated beam sections at simulated failure, it was decided to take  $K$  equal to 0.5. Table 6 provides a summary of the effective web widths for all the investigated cases.

For the unstiffened cases, the effective width typically increases as the castellated beam depth increased. Also, for the stiffened cases and load position A, the effective width increased as the section depth increases; however, for load positions B and C, there was no direct relationship between the increase in depth and the magnitude of the effective web width.

In most unstiffened cases, the calculated effective width is greater than the minimum width of the castellated beam web post  $e$  (Table 7). For all stiffened cases and load position A the effective widths are always greater than  $e$ . For stiffened cases in which load position B was investigated, the effective width was always smaller than  $e$ , and for stiffened cases and load position C, the effective width was greater than  $e$  for C12×40, C18×50 and C24×50 and smaller than  $e$  for C30×62 and C40×84. The reason the effective width was smaller than  $e$  in some of the stiffened cases is attributed to the fact that the loads obtained from nonlinear finite element analyses include the effects of local buckling, and the proposed approach was developed such that the engineer would only have to check the global buckling of the equivalent column shapes. The results provided in Table 7 suggest once again that the stiffeners in load case B are not placed in the optimal position because the buckling of the web post occurs prior to the efficient engagement of the stiffeners.

To complement the proposed simplified approach, an additional investigation was carried out in which the effective width,  $b_{eff}$ , was taken equal to the minimum width of the web post,  $e$  (i.e.,  $b_{eff} = 1.0e$ ), and the nominal capacities calculated using the proposed simplified approach were compared with those obtained from finite element analyses (FEA). Table 8 provides a summary of the results. Assuming that  $b_{eff} = 1.0e$  generally resulted in conservative estimates of the nominal load capacity for web post compression buckling for the unstiffened cases. The average of the ratios between the predicted capacity using the simplified approach and the computed capacity using FEA was 0.87. For CB12×40

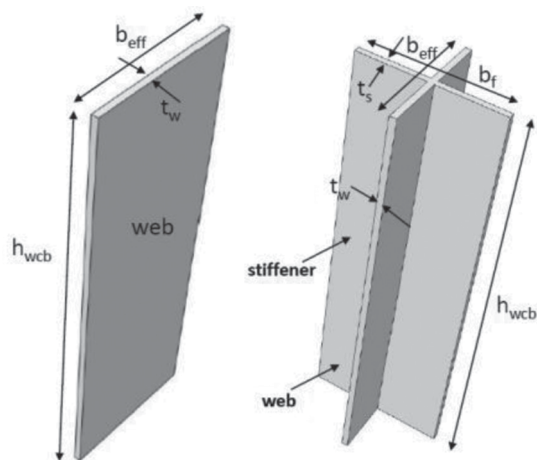


Fig. 15. Equivalent rectangular and cruciform column sections.

Table 7. Comparison of Effective Web Width with Minimum Width of Web Post ( $K = 0.5$ )						
Section	Stiffener	Load Position	$b_{eff}^*$ (in.)	$e^{**}$ (in.)	Section Width ( $S^{**}$ ) (in.)	Ratio = $b_{eff}/e$
CB12×40	No	A	4.29	4.00	11.5	1.07
		B	4.11	4.00	11.5	1.03
		C	2.05	2.00	5.75	1.03
	Yes	A	5.63	4.00	11.5	1.41
		B	2.37	4.00	11.5	0.59
		C	2.58	2.00	5.75	1.29
CB18×50	No	A	4.24	4.25	15	1.00
		B	4.14	4.25	15	0.97
		C	2.06	2.125	7.5	0.97
	Yes	A	7.48	4.25	15	1.76
		B	2.63	4.25	15	0.62
		C	2.84	2.125	7.5	1.34
CB24×50	No	A	5.28	4.50	19	1.17
		B	5.11	4.50	19	1.14
		C	2.55	2.25	9.5	1.13
	Yes	A	7.74	4.50	19	1.72
		B	2.70	4.50	19	0.60
		C	2.30	2.25	9.5	1.02
CB30×62	No	A	7.93	6.00	23	1.32
		B	7.68	6.00	23	1.28
		C	3.82	3.00	11.5	1.27
	Yes	A	12.17	6.00	23	2.03
		B	2.11	6.00	23	0.35
		C	2.58	3.00	11.5	0.86
CB40×84	No	A	10.36	7.00	30	1.48
		B	9.91	7.00	30	1.42
		C	4.94	3.50	15	1.41
	Yes	A	13.28	7.00	30	1.90
		B	1.86	7.00	30	0.27
		C	2.38	3.50	15	0.68

\* See Figure 7.  
\*\* See Table 2.

and CB18×50, this assumption led to rather accurate results for the unstiffened cases. However, as the castellated beam depth increased, this assumption led to more conservative results for castellated beams with no stiffeners.

For castellated beams with stiffeners and load position A, assuming that  $b_{eff} = 1.0e$  resulted in conservative estimates. For stiffened cases and load position B, this assumption always led to estimates that were higher than those

computed from FEA. For stiffened cases and load position C, the results varied. For the first three castellated beams, the assumption led to rather accurate estimates, and for the last two, it led to estimates that were higher than those computed from FEA. In general, assuming that  $b_{eff} = 1.0e$  serves as a good starting point to create a general idea for the capacity of the web post in compression, with the exception of the stiffened cases for load position B and the two deeper beam



Table 8. Comparison of Predicted and Computed Strengths for the Web Post Buckling Limit State						
Section	Stiffener	Load Position	$b_{eff} = 1.0e^*$ (in.)	$P_{ns}$ (kips)	$P_{nFEA}$ (FEA) (kips)	Ratio = Min ( $P_{ns}/P_{nFEA}$ )
CB12×40	No	A	4.00	72.5	77.8	0.93
		B	4.00	72.5	74.6	0.97
		C	2.00	36.3	37.2	0.98
	Yes	A	4.00	289.5	327.3	0.89
		B	4.00	289.5	264.2	1.10
		C	2.00	248.9	268.6	0.93
CB18×50	No	A	4.25	56.1	56.0	1.00
		B	4.25	56.1	54.6	1.03
		C	2.125	28.1	27.2	1.03
	Yes	A	4.25	289.7	349.4	0.83
		B	4.25	289.7	264.9	1.09
		C	2.125	247.6	269.2	0.92
CB24×50	No	A	4.50	36.7	43.1	0.85
		B	4.50	36.7	41.7	0.88
		C	2.25	18.4	20.8	0.88
	Yes	A	4.50	272.9	331.4	0.82
		B	4.50	272.9	245.5	1.11
		C	2.25	216.8	228.0	0.95
CB30×62	No	A	6.00	32	42.3	0.76
		B	6.00	32	41.0	0.78
		C	3.00	16	20.4	0.79
	Yes	A	6.00	319.8	388.8	0.82
		B	6.00	319.8	215.3	1.49
		C	3.00	265.5	253.4	1.23
CB40×84	No	A	7.00	32	47.1	0.68
		B	7.00	32	45.1	0.71
		C	3.50	16	22.5	0.71
	Yes	A	7.00	387.6	481.1	0.81
		B	7.00	387.6	151.1	2.57
		C	3.50	315.8	237.7	1.33
Average unstiffened						0.87
Average stiffened						1.13

\* See Table 2 (for load position C, e is half of the value in Table 2).

sections. More accurate estimates can be obtained by using the reported effective width values provided in Table 6.

An example is provided to illustrate the application of the proposed simplified approach. The example features a CB30×62 that supports a composite roof slab and several stub columns. The CB cantilevers over two column supports.

The location of the stub columns and support columns was intentionally chosen as a variable to illustrate the variety of loading conditions that a CB may be subject to. Additionally, column sizes and the corresponding base plates and cap plates were chosen to cover the range of loading conditions that was investigated in this paper.

## DESIGN EXAMPLE

### Given:

The CB30×62 shown in Figure 16 is used to support a portion of the roof slab, two stub columns supporting a mechanical unit and two canopy columns providing shelter for the mechanical unit. The worst-case factored reactions and concentrated loads are provided in Figure 16. The top flange is braced by the roof slab, and discrete braces are provided at the bottom flange at concentrated loads and reaction points. Assume that the yield stress for the CB is  $F_y = 50$  ksi and that the modulus of elasticity is  $E = 29,000$  ksi. Determine whether stiffeners should be provided in the castellated beam at concentrated loads and reaction points.

### Solution:

#### Reaction 1 ( $R_1 = 60$ kips)

Using load position A without a stiffener, select the effective width from Table 6 ( $b_{eff} = 7.93$  in.) Check the web of the castellated beam as a rectangular column fixed at both ends per AISC *Specification* Section E3 (2010).

Calculate section properties:

$$\begin{aligned} L &= d_g - 2t_f \\ &= 30 \text{ in.} - 2(0.625 \text{ in.}) \\ &= 28.75 \text{ in. (clear distance between flanges } L = h_{wcb} \text{)} \end{aligned}$$

$$\begin{aligned} I_{rec} &= \frac{1}{12} b_{eff} t_w^3 \\ &= \frac{1}{12} (7.93 \text{ in.})(0.375 \text{ in.})^3 \\ &= 0.035 \text{ in.}^4 \end{aligned}$$

$$\begin{aligned} A_{rec} &= b_{eff} t_w \\ &= (7.93 \text{ in.})(0.375 \text{ in.}) \\ &= 2.97 \text{ in.}^2 \end{aligned}$$

$$\begin{aligned} r &= \sqrt{\frac{I_{rec}}{A_{rec}}} \\ &= 0.11 \text{ in.} \end{aligned}$$

Calculate elastic critical buckling stress and slenderness ratio:

$$\begin{aligned} F_e &= \frac{\pi^2 E}{\left(\frac{KL}{r}\right)^2} \\ &= \frac{\pi^2 (29,000 \text{ ksi})}{\left(\frac{0.5(28.75 \text{ in.})}{0.11 \text{ in.}}\right)^2} \\ &= 16.8 \text{ ksi} \\ \frac{KL}{r} &= \frac{0.5(28.75 \text{ in.})}{0.11 \text{ in.}} \\ &= 130.7 > 4.71 \sqrt{\frac{E}{F_y}} = 4.71 \sqrt{\frac{29,000 \text{ ksi}}{50 \text{ ksi}}} = 113.43 \end{aligned}$$

Calculate the flexural buckling stress, nominal and available compressive strength:

$$\begin{aligned}
 F_{cr} &= 0.877F_e \\
 &= 0.877(16.8 \text{ ksi}) \\
 &= 14.7 \text{ ksi} < F_y = 50 \text{ ksi} \\
 P_n &= F_{cr}A_g \\
 &= (14.7 \text{ ksi})(2.97 \text{ in.}^2) \\
 &= 43.7 \text{ kips} \\
 \phi P_n &= 0.9(43.7 \text{ kips}) \\
 &= 39.3 \text{ kips} < P_u = 60.0 \text{ kips} \quad \text{Stiffeners are required.}
 \end{aligned}$$

Provide 1/2-in. transverse stiffeners, and check the enhanced capacity of the web. Using load position A with stiffeners, select the effective width from Table 6 ( $b_{eff} = 12.17 \text{ in.}$ ). Check the web of the castellated beam as a column with a cruciform cross-sectional shape fixed at both ends per AISC Specification Sections E3 and E4 (2010).

Calculate section properties:

$$\begin{aligned}
 b_s &= b_f - t_w \\
 &= 7.875 \text{ in.} \\
 I_x &= \frac{1}{12} t_w b_{eff}^3 \\
 &= \frac{1}{12} (0.375 \text{ in.})(12.17 \text{ in.})^3 \\
 &= 56.3 \text{ in.}^4
 \end{aligned}$$

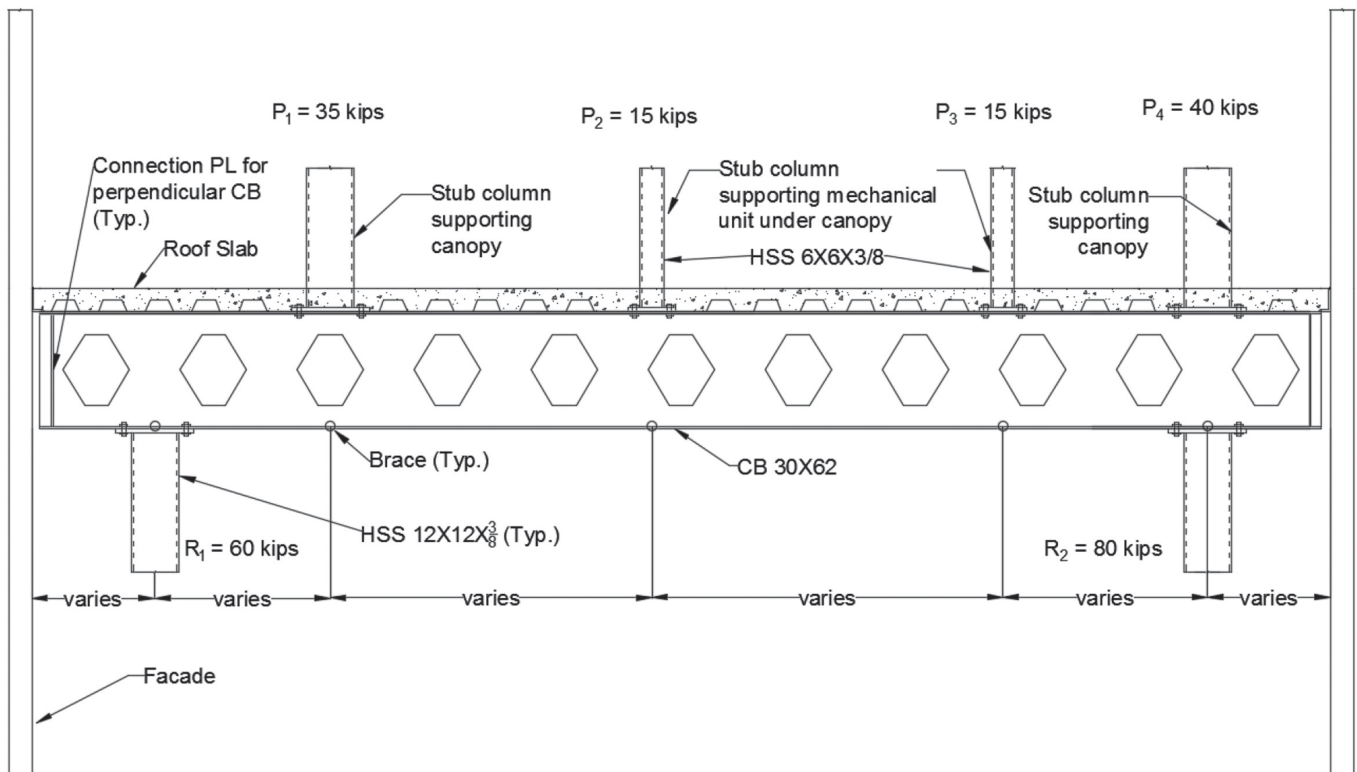


Fig. 16. Example of castellated beam subject to concentrated loads.

$$\begin{aligned}
 I_y &= 2 \left[ \frac{1}{12} t_s \left( \frac{b_s}{2} \right)^3 + t_s \left( \frac{b_s}{2} \right) \left( \frac{b_s}{4} + \frac{t_w}{2} \right)^2 \right] \\
 &= 2 \left[ \frac{1}{12} (0.5 \text{ in.}) (3.9375 \text{ in.})^3 + (0.5 \text{ in.}) (3.9375 \text{ in.}) \left( \frac{3.9375 \text{ in.}}{2} + \frac{0.375 \text{ in.}}{2} \right)^2 \right] \\
 &= 23.39 \text{ in.}^4
 \end{aligned}$$

$$\begin{aligned}
 A &= b_{eff} t_w + b_s t_s \\
 &= (12.17 \text{ in.}) (0.375 \text{ in.}) + (7.875 \text{ in.}) (0.5 \text{ in.}) \\
 &= 8.50 \text{ in.}^2
 \end{aligned}$$

$$\begin{aligned}
 J &= \frac{1}{3} b_s t_s^3 + \frac{1}{3} b_{eff} t_w^3 \\
 &= \frac{1}{3} (7.875 \text{ in.}) (0.5 \text{ in.})^3 + \frac{1}{3} (12.17 \text{ in.}) (0.375 \text{ in.})^3 \\
 &= 0.542 \text{ in.}^4
 \end{aligned}$$

$$\begin{aligned}
 C_w &= \frac{1}{9} b_s t_s^3 + \frac{1}{9} b_{eff} t_w^3 \\
 &= \frac{1}{9} (7.875 \text{ in.}) (0.5 \text{ in.})^3 + \frac{1}{9} (12.17 \text{ in.}) (0.375 \text{ in.})^3 \\
 &= 0.181 \text{ in.}^4
 \end{aligned}$$

$$\begin{aligned}
 r_x &= \sqrt{\frac{I_x}{A}} \\
 &= \sqrt{\frac{56.3 \text{ in.}^4}{8.50 \text{ in.}^2}} \\
 &= 2.57 \text{ in.}
 \end{aligned}$$

$$\begin{aligned}
 r_y &= \sqrt{\frac{I_y}{A}} \\
 &= \sqrt{\frac{23.39 \text{ in.}^4}{8.50 \text{ in.}^2}} \\
 &= 1.66 \text{ in.}
 \end{aligned}$$

Calculate elastic critical buckling stress:

$$\begin{aligned}
 F_{torsional} &= \left[ \frac{\pi^2 E C_w}{(K_z L)^2} + GJ \right] \frac{1}{I_x + I_y} \\
 &= \left\{ \frac{\pi^2 (29,000 \text{ ksi}) (0.181 \text{ in.}^4)}{[0.5(28.75 \text{ in.})]^2} + (11,200 \text{ ksi}) (0.542 \text{ in.}^4) \right\} \frac{1}{56.3 \text{ in.}^4 + 23.39 \text{ in.}^4} \\
 &= 79.3 \text{ ksi}
 \end{aligned}$$

$$\begin{aligned}
 F_{flexural} &= \frac{\pi^2 E}{\left[ \frac{K_x L}{r_x} \right]^2} \\
 &= \frac{\pi^2 (29,000 \text{ ksi})}{\left[ \frac{0.5(28.75 \text{ in.})}{2.57 \text{ in.}} \right]^2} \\
 &= 9,150 \text{ ksi}
 \end{aligned}$$

$$\begin{aligned}
F_{e\text{flexuraly}} &= \frac{\pi^2 E}{\left(\frac{K_y L}{r_y}\right)^2} \\
&= \frac{\pi^2 (29,000 \text{ ksi})}{\left[\frac{0.5(28.75 \text{ in.})}{1.66 \text{ in.}}\right]^2} \\
&= 3,820 \text{ ksi} \\
F_e &= F_{e\text{torsional}} \\
&= 79.3 \text{ ksi} > 0.44 F_y = 0.44(50 \text{ ksi}) = 22.0 \text{ ksi}
\end{aligned}$$

Calculate buckling stress, nominal and available compressive strength:

$$\begin{aligned}
F_{cr} &= \left(0.658 \frac{F_y}{F_e}\right) F_y \\
&= \left(0.658 \frac{50 \text{ ksi}}{79.3 \text{ ksi}}\right) 50 \text{ ksi} \\
&= 38.4 \text{ ksi} \\
P_n &= F_{cr} A < F_y A = (38.4 \text{ ksi})(8.50 \text{ in.}^2) = 326 \text{ kips} \\
\phi P_n &= 0.9(326 \text{ kips}) \\
&= 293 \text{ kips} > 60.0 \text{ kips} \quad \mathbf{o.k.}
\end{aligned}$$

Again, 1/2-in. stiffeners on each side of the castellated beam web provide adequate strength to prevent the limit state of web post compression buckling.

**Reaction 2 ( $R_2 = 80 \text{ kips}$ )**

Using the same procedure, provide 1/2-in. stiffeners on each side of the castellated beam web.

**Concentrated Load  $P_1 = 35 \text{ kips}$ ,  $P_2 = P_3 = 15 \text{ kips}$**

Using the same procedure, no stiffeners are required.

**Concentrated Load  $P_4 = 40 \text{ kips}$**

In this case, the concentrated load aligns with the column reaction. Because the column reaction is higher, the necessity for stiffeners was determined based on the column reaction, and it was concluded that stiffeners were required.

## CONCLUSIONS

The research presented in this paper addressed the need for a design method to estimate the nominal capacity of castellated beams against concentrated loads as it pertains to the limit state of web post buckling in compression. The other limit states summarized in the Introduction—such as flexural failure, shear failure, lateral torsional buckling, Vierendeel mechanism, local buckling, buckling of the web post due to shear and fracture of a welded joint—should each be checked as described in the provided References so that the overall safety of the castellated beam in question is ensured. This investigation dealt with a loading condition in which the load is applied over a support. This was done to specifically study the limit state of web post buckling in compression. It was demonstrated that this loading condition represents the worst-case scenario with respect to the limit state of web post buckling in compression and that other conditions in which the load is away from the supports can be conservatively checked using the simplified approach presented herein.

Five castellated beam section depths were considered, which cover a wide range of the available depths. For each section three load cases were considered: (A) center of load aligns with the middle of web post, (B) center of load aligns with the center of the hole, and (C) center of load aligns with a point halfway between the center of web post and center of hole. For each load position, two cases were considered: one without a stiffener and one with a full-height stiffener. This resulted in a total of 30 cases, which were investigated using nonlinear finite element analyses that accounted for geometric and material nonlinearities, including the effect of initial imperfections.

The peak loads obtained from the analyses of unstiffened cases were compared with AISC *Specification* (2010) provisions for flanges and solid webs with concentrated forces. Only Sections J10.2, J10.3 and J10.5 were considered for comparison because the castellated beam sections were assumed to be adequately braced for out-of-plane translations at the top and bottom flanges. When the load was considered to be away from member ends, AISC provisions for solid web beams grossly overestimated the capacity of the sections under consideration. This was expected for several reasons. Equation 6 was developed for solid web beams and does not take into consideration the presence of the holes. Additionally, in the cases investigated in this study, the restraint provided by the continuation of the castellated beam to the web on both sides (if applicable) was conservatively ignored, whereas in the derivation of Equation 6, the square web panel was assumed to be simply supported on all sides. Also, the aspect ratio between the loaded length and member depth was, at best, 1.0 (Table 1). When the load was assumed to be at member ends (Eq. 7), the prediction improved, especially for load cases A and B. This is

also expected because, when the load is applied at member ends, the restraint provided by the continuation of the beam to the web applies only to one end, and it represents more closely the boundary conditions used in this study. For load case C, the equation still grossly overestimated the capacity of the castellated beam sections because it does not take into account the shorter loaded length and the lower aspect ratios. The average between the peak load obtained from nonlinear finite element analysis and that obtained from the AISC *Specification* web buckling provisions, assuming that the load is at member ends, was 1.16 for load position A and B and 0.57 for load position C. It was pointed out that the current equations in the AISC *Specification* in Section J10.5 for checking the limit state of web compression buckling in wide flange beams do not distinguish between various load-bearing lengths. This shortcoming is currently being addressed as part of another study.

A simplified approach was presented for checking the limit state of web post buckling in compression, which considers the web of a castellated beam as an equivalent column whose height is equal to the clear height of the web. This simplified approach assumes that the top and bottom flanges are adequately braced against out-of-plane translations. For the unstiffened cases, the equivalent column has a rectangular cross-section whose thickness is equal to the thickness of the web, and the width can be determined based on the effective width values presented in this paper. This equivalent rectangular column can be checked using AISC *Specification* provisions in Section E3 (AISC, 2010). For the stiffened case, the equivalent column has a cruciform cross-sectional shape that consists of the beam web and the stiffener. The width of the castellated beam web that can be used to determine the capacity of the column can be determined based on the effective width values presented in this paper. The equivalent column with a cruciform cross-sectional shape need only be checked for global buckling using the provisions of AISC *Specification* in Sections E3 and E4 because the effects of local buckling were included in the calculation of the effective web width. A  $K$  value equal to 0.5 is recommended based on an examination of the deformed shapes of castellated beam sections at simulated failure. It was demonstrated that taking  $b_{eff} = 1.0e$  provided a rather accurate estimate of the load capacities for CB12×40 and CB18×50, and a conservative estimate for the rest of the castellated beams examined. It was also demonstrated that  $b_{eff} = 1.0e$  taking for all stiffened cases and load position A resulted in conservative estimates for the web post buckling capacity. The estimated capacity for stiffened cases and load position B based on this assumption was always higher than that computed from FEA. The results for stiffened cases and load position C varied.

The capacity of the unstiffened beams against concentrated loads, as it relates to the limit state of buckling of the



web post in compression, ranged from 1.5 kip/in. to 6.8 kip/in., assuming that the load was applied over a distance equal to the spacing of the holes for load cases A and B and half the distance between the holes for load case C. These capacities were significantly increased when the castellated beam sections were reinforced with stiffeners, and they ranged from 5 kip/in. to 47 kip/in.

The results presented in this paper can be used to determine the requirement for stiffeners in castellated beams to prevent the buckling of the web post due to compression. Physical testing of castellated beam sections subject to compression loads similar to the tests performed by Chen and Oppenheim (1974) and Chen and Newlin (1973) should be conducted to complement the results obtained from the analytical work presented in this study.

### Recommendations for Other Cases

The results presented in this paper can be directly applied in cases where the castellated beam sizes match those investigated herein. For other cases, the following practical approaches are recommended unless a finite element study is undertaken. For unstiffened castellated beams that are properly braced against out-of-plane translations at the top and bottom flanges, the effective web width,  $b_{eff}$ , for all loading cases considered can be taken equal to  $e$  (minimum width of the web post) because, in all investigated cases, the calculated effective width was typically larger than  $e$ . In the CB18×50 case, for load positions B and C, the ratio  $b_{eff}/e$  was slightly smaller than one (0.97); however, such a small difference is inconsequential given the level of accuracy considered in structural design. Additionally, it was demonstrated that taking  $b_{eff} = 1.0e$  provided a rather accurate estimate of the load capacities for the CB12×40 and CB18×50 and a conservative estimate for the rest of the castellated beams examined. As discussed in the previous sections, the height of the equivalent rectangular column can be taken equal to  $h_{wcb}$ , and  $K$  can be taken equal to 0.5. Additionally, if a more accurate estimate is desired, interpolation between the reported effective widths may be used for castellated beams that fall between CB24×50 and CB40×84 for the unstiffened cases.

For stiffened cases and load position A, Figure 13 suggests that the capacity for the limit state of web compression buckling can be based on the yield strength of the section at mid-height of the web. Additionally, it was demonstrated that taking  $b_{eff} = 1.0e$  for all stiffened cases and load position A resulted in conservative estimates for the web post buckling capacity.

For stiffened cases and load positions B and C, a rational comparison between the case in question and the cases investigated in this paper can be used to arrive at a reasonable conclusion.

### REFERENCES

- AISC (2010), *Specification for Structural Steel Buildings*, ANSI/AISC 360-10, American Institute of Steel Construction, Chicago, IL.
- Arasaratnam, P., Sivakumaran, K.S. and Tait, M.J. (2011), “True Stress-True Strain Models for Structural Steel Elements,” *ISRN Civil Engineering*, Vol. 2011, Article ID 656401, 11 pages, 2011. doi:10.5402/2011/656401.
- Blodgett, O.W. (1966), *Design of Welded Structures*, The James F. Lincoln Arc Welding Foundation, Cleveland, OH.
- Chen, W.F. and Newlin, D.E. (1973), “Column Web Strength in Steel Beam-to-Column Connections,” *Journal of the Structural Division*, ASCE, Vol. 99, ST9, September.
- Chen, W.F. and Oppenheim, I.J. (1974), “Web Buckling Strength of Beam-to-Column Connections,” *Journal of the Structural Division*, ASCE, Vol. 100, ST1, January.
- Crisfield, M.A. (1981), “A Fast Incremental/Iteration Solution Procedure That Handles Snapthrough,” *Computers and Structures*, Vol. 13, pp. 55–62.
- Darwin, D. (2003), *Design Guide 2: Design of Steel and Composite Beams with Web Openings*, American Institute of Steel Construction, Chicago, IL.
- Dassault Systemes Simulia Corp. (2014), *Abaqus User's Manual*, Version 6.14-2.
- Durif, S., Bouchaïr, A. and Vassart, O. (2013), “Experimental Tests and Numerical Modeling of Cellular Beams with Sinusoidal Openings,” *Journal of Constructional Steel Research*, Vol. 82, pp. 72–87.
- Ellobody, E. (2011), “Interaction of Buckling Modes in Castellated Steel Beams,” *Journal of Constructional Steel Research*, Vol. 67, No. 5, pp. 814–825.
- Ellobody, E. (2012), “Nonlinear Analysis of Cellular Steel Beams Under Combined Buckling Modes,” *Thin-Walled Structures*, Vol. 52, pp. 66–79.
- ENV 1993-1-1 (1993), *Eurocode 3: Design of Steel Structures—Part 1-1: General Rules and Rules for Buildings*, and *Amendment A2 of Eurocode 3: Annex N Openings in Webs*, British Standards Institution.
- Halleux, P. (1967), “Limit Analysis of Castellated Steel Beams,” *Acier-Stahl-Steel*, Vol. 32, No. 3, pp. 133–144, March.
- Hosain, M.U. and Spiers, W.G. (1973), “Experiments on Castellated Steel Beams,” *Supplement to Welding Journal*, American Welding Society and the Welding Research Council.
- Kerdal, D. and Nethercot, D.A. (1984), “Failure Modes for Castellated Beams,” *Journal of Constructional Steel Research*, Vol. 4, No. 4, pp. 295–315.

- Moen, D.C. (2008), *Direct Strength Design of Cold-Formed Steel Members with Perforations*, Ph.D. Dissertation, John Hopkins University, Baltimore, MD.
- Scherer Steel Structures, Inc. (2015), <http://scherersteel.com/joists-girders/image001/>.
- Soltani, M.R., Bouchaïr, A. and Mimoune, M. (2012), “Non-linear FE Analysis of the Ultimate Behavior of Steel Castellated Beams,” *Journal of Constructional Steel Research*, Vol. 70, pp. 101–114.
- SCI (2006), *Design of Composite Beams with Large Openings for Services*, Publication document RT959, version 05, May, Imperial College London, Silwood Park Campus, Buckhurst Road, Ascot, West Berkshire, United Kingdom.
- Tsavdaridis, K.D. and D’Mello, C. (2011), “Web Buckling Study of the Behavior and Strength of Perforated Steel Beams with Different Novel Web Opening Shapes,” *Journal of Constructional Steel Research*, Vol. 67, No. 10, pp. 1605–1620.
- Tsavdaridis, K. D., D’Mello, C. (2012), “Optimisation of Novel Elliptically-Based Web Opening Shapes of Perforated Steel Beams,” *Journal of Constructional Steel Research*, vol. 76, pp. 39-53.
- United Steel Co. Ltd., Research and Development Department (1957), *Properties and Strengths of Castella Beams: Consideration of Previous Tests*, Report D.GE. 71/262, Swinden Laboratories, Rotherham, April.
- United Steel Co. Ltd., Research and Development Department (1962), *Web Strength of Castella Beams*, Report D.TS. 6/262/6, Swinden Laboratories, Rotherham, May.
- Wang, P., Ma, Q. and Wang, X. (2014), “Investigation on Vierendeel Mechanism Failure of Castellated Steel Beams with Fillet Corner Web Openings,” *Engineering Structures*, Vol. 74, pp. 44–51.
- Zaarour, W. and Redwood, R. (1996), “Web Buckling in Thin Webbed Castellated Beams,” *Journal of Structural Engineering*, ASCE, Vol. 122, No. 8, pp. 860–866.



# Observations from Cyclic Tests on Deep, Wide-Flange Beam-Columns

GULEN OZKULA, JOHN HARRIS and CHIA-MING UANG

---

## ABSTRACT

As part of a National Institute of Standards and Technology (NIST) comprehensive research program to study the seismic behavior and design of deep, wide-flange structural steel beam-column members for application in seismic design and construction of steel special moment frames, 25 deep column specimens were subjected to inelastic cyclic loading with three different levels of constant compression axial load ( $C_a = 0.2, 0.4$  and  $0.6$ ). The test matrix included five W24 sections (W24×55 to W24×176) to cover a wide range of element slenderness ratios for flange and web local buckling and member slenderness ratios for lateral-torsional buckling and weak-axis flexural buckling. The specimens satisfied AISC 341 requirements for highly or moderately ductile elements. All specimens were subjected to strong-axis bending, except for three specimens that were subjected to weak-axis bending and one specimen that was subjected to biaxial bending. Test results showed that the slenderness ratios had a significant effect on the failure mode—local versus global buckling. The presence of an axial load produced significant local buckling and axial shortening. The level of axial load also affected the plastic rotation capacity. Specimens with weak-axis bending were ductile, showing no local buckling up to a high story-drift ratio. Most of the strong-axis bending specimens were not able to deliver a plastic rotation of 0.03 radian.

**Keywords:** Beam-column, cyclic behavior, plastic rotation, local buckling, lateral-torsional buckling.

---

## INTRODUCTION

Research on the cyclic behavior of W14 columns under high axial load and seismic drift for braced frame applications has been conducted by Newell and Uang (2008). For special moment frame (SMF) design, however, designers prefer to use deeper columns (e.g., W24 to W36 sections) to satisfy code-enforced story-drift limits. Because the cross-section element and member slenderness ratios are significantly high for deep columns, this class of columns is prone to various forms of local and global buckling that may impair their lateral drift capacity and gravity load-carrying strength. Unfortunately, minimal experimental research is available to support the seismic design or assessment provisions in AISC 341 (AISC, 2010a) and ASCE 41 (ASCE, 2013) for these deeper columns. To fill this gap, NIST developed a comprehensive research plan to study the seismic behavior and design of the wide-flange structural steel beam-column

members (NIST, 2011). The plan included studies at the member, subassembly and system levels. The first step in implementing this plan was to experimentally evaluate the cyclic behavior of plastic hinges in deep columns. Test results will then be used by NIST to validate computational models and to improve seismic design provisions for these types of columns. This paper presents observations from this test series. A detailed report of the testing program and data will be released in the future. Evaluation of the test data and their impact on seismic design and assessment provisions is ongoing.

## TEST SETUP AND SPECIMENS

Twenty-five W24 specimens were subjected to three different levels of constant axial load combined with cyclic story-drift demands; see Table 1 for the test matrix—only 21 of the 25 tests are presented in this paper. Five wide-flange sections were selected in order to cover a wide range of element slenderness ratios for flange local buckling (FLB) and web local buckling (WLB). The use of lighter sections (W24×84 and W24×55) also widened the range of member slenderness ratios for lateral-torsional buckling (LTB) and weak-axis flange buckling (FB). Figure 1 shows a comparison of the flange and web width-to-thickness ratios to the seismically compact limits prescribed in AISC 341. The limiting width-to-thickness ratios for highly ductile ( $\lambda_{hd}$ ) and moderately ductile ( $\lambda_{md}$ ) elements are also shown in Figure 1. For FLB,

---

Gulen Ozkula, Graduate Student Researcher, University of California, San Diego, CA. Email: gozkula@ucsd.edu

John Harris, Research Structural Engineer, National Institute of Standards and Technology, Washington, DC. Email: john.harris@nist.gov

Chia-Ming Uang, Professor, University of California, San Diego, CA. Email: cmu@ucsd.edu (corresponding)

---

Table 1. Test Matrix									
Group No.	Shape	Specimen Designation	Normalized Slenderness				Column Axial Load		Bending Direction
			$\frac{b_f/2t_r}{\lambda_{hd}}$	$\frac{h/t_w}{\lambda_{hd}}$	$\frac{L}{L_{hd}}$	$\frac{L}{r_y}$	$C_a$	$P$ (kips)	
1	W24×176	1L	0.67	0.57	1.42	71.1	0.2	465	Strong axis
		1M		0.61			0.4	931	
		1H		0.66			0.6	1396	
2	W24×131	2Z	0.93	0.66	1.46	72.7	0.0	0	
		2L		0.70			0.2	347	
		2L-P		0.70			0.2	347	
		2M		0.76			0.4	693	
		2H		0.82			0.6	1040	
3	W24×104	3L	1.18	0.85	1.49	74.2	0.2	276	
		3M		0.91			0.4	551	
		3H		1.00			0.6	826	
4	W24×84	4L	0.81	0.91	2.22	110.8	0.2	222	
		4M		0.98			0.4	445	
5	W24×55	5L	0.81	1.08	3.23	161.2	0.2	146	
		5LM		1.12			0.3	219	
		5M		1.26			0.4	292	
6	W24×131	6L	0.93	0.70	1.46	72.7	0.2	347	Weak axis
		6L-P		0.70			0.2	347	
		6H		0.82			0.6	1040	
7	W24×131	7M	0.93	0.76	1.46	72.7	0.4	693	Biaxial axis
8	W24×131	8M	0.93	0.76	1.46	72.7	0.4	693	Strong axis, Near-fault

$$\lambda_{hd} = 0.3\sqrt{E/F_y} \quad (1a)$$

$$\lambda_{hd} = 0.38\sqrt{E/F_y} \quad (1b)$$

and for WLB when  $C_a = P/\phi_c P_y$  is larger than 0.125,

$$\lambda_{hd} = 0.77\sqrt{E/F_y} (2.93 - C_a) \geq 1.49\sqrt{E/F_y} \quad (2a)$$

$$\lambda_{hd} = 1.12\sqrt{E/F_y} (2.33 - C_a) \geq 1.49\sqrt{E/F_y} \quad (2b)$$

In Table 1, the unbraced length,  $L$ , is also normalized by  $L_{hd}$  and  $r_y$ , respectively, where

$$L_{hd} = 0.086r_y E/F_y \quad (3)$$

Note that  $L_{hd}$  is the limiting unbraced length for beams, but not columns, for a SMF in AISC 341. Specimens were designated “L,” “M” and “H” to represent low ( $C_a = 0.2$ ), medium ( $C_a = 0.4$ ), and high ( $C_a = 0.6$ ) axial load levels, respectively. Only one specimen (2Z) was tested without any axial load. Pseudo-static cyclic lateral displacement used for testing followed that specified in Section K2.4b of AISC 341 (2010a) for the majority of column specimens. Two specimens (2L-P and 6L-P) were tested monotonically, one for

strong-axis and the other one for weak-axis bending. Specimen 7M was tested with biaxial bending, and specimen 8M was tested by using a near-field loading protocol. Each specimen was 18 ft long with 3-in.-thick base plates welded at each end. ASTM A992 (ASTM, 2012) steel was specified for the column specimens. The material properties obtained from tensile coupon tests are summarized in Table 2.

The overall view of the test setup is shown in Figure 2. Testing was conducted in the Seismic Response Modification Device (SRMD) Test Facility at the University of California, San Diego. As shown in Figure 2, beam-column specimens were tested in a horizontal position with one end attached to a strong wall fixture, while the other end was attached to a reaction block on the shake table. Both ends of the column specimens were welded to the end plates with complete-joint-penetration (CJP) welds. All specimens were tested with presumed fixed-fixed boundary conditions; lateral drift data presented in this paper have been adjusted for rotational flexibility in the boundary conditions (Ozkula and Uang, 2015). For a typical test, the target axial load was first applied to the specimen and held constant. Then the pseudo-static cyclic drift, computed as the AISC specified story-drift angle multiplied by the column length (=18 ft), was applied to the moving end of the specimen.



Table 2. Steel Tensile Coupon Test Results				
Shape	Component	Yield Stress (ksi)	Tensile Strength (ksi)	Elongation* (%)
W24x176	Flange	52.5	81.8	38.1
	Web	58.5	82.5	38.0
W24x131	Flange	50.8	75.9	38.4
	Web	55.4	77.7	35.4
W24x104	Flange	51.5	78.0	36.5
	Web	58.1	80.6	31.3
W24x84	Flange	51.3	77.6	36.2
	Web	58.8	80.2	31.0
W24x55	Flange	53.7	71.5	38.0
	Web	59.8	74.3	32.4

\* Based on a 2-in. gage length.

### DATA REDUCTION

In the following presentation, the story-drift ratio (SDR) is defined as the imposed lateral displacement,  $\Delta$ , divided by the column length,  $L$ . Assuming an inflection point at the mid-height of the column, the end moment including the  $P$ - $\Delta$  effect is computed as

$$M = \frac{1}{2}(VL + P\Delta) \quad (4)$$

where  $V$  is the measured lateral load (i.e., column shear) and  $P$  is the measured axial load. End moment can be normalized by either the plastic moment,  $M_p$ , or the reduced plastic

moment,  $M_{pc}$ . Reduced moment can be computed using Equation 5(a) for strong-axis and Equation 5(b) for weak-axis bending.

$$M_{pc} = 1.18 \left( 1 - \frac{P}{P_y} \right) M_p \leq M_p \quad (5a)$$

$$M_{pc} = 1.19 \left[ 1 - \left( \frac{P}{P_y} \right)^2 \right] M_p \leq M_p \quad (5b)$$

The measured yield stresses were used to compute these strengths.

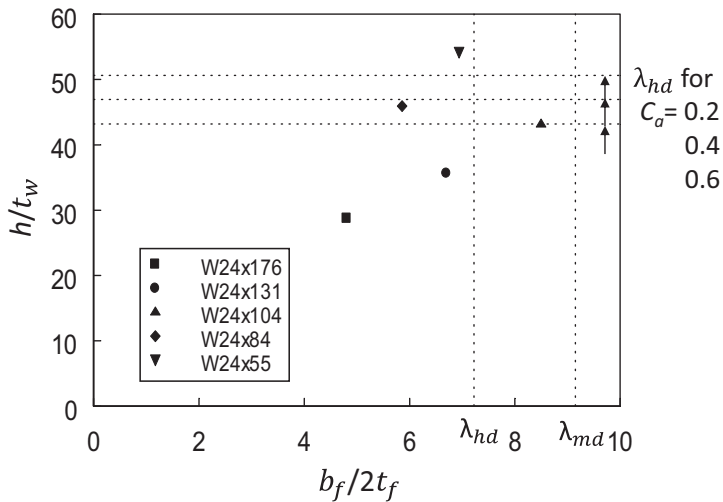


Fig. 1. Comparison of width-to-thickness ratios.

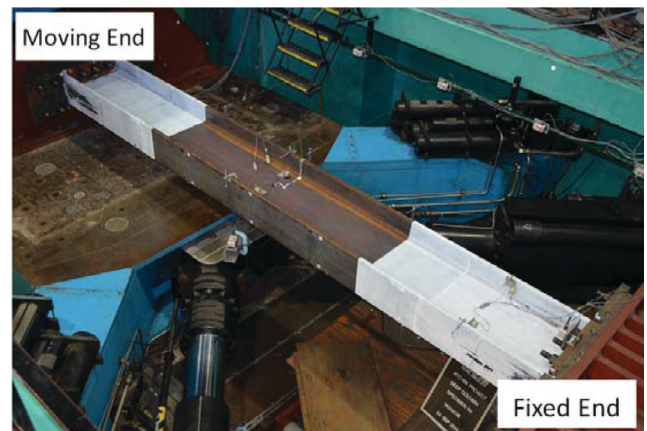


Fig. 2. Test setup.

## EXPERIMENTAL RESULTS

### Group 2: W24×131 Specimens

The flanges and webs of group 2 specimens are classified as highly ductile. This group with five specimens (2Z, 2L, 2LP, 2M, 2H) served as the reference group for comparison with the response of the other groups. To evaluate the effect of axial load, 2Z without an axial load was included in this group. This “beam” specimen was able to reach 7% drift without any strength degradation before one flange fractured near the weld access hole. Local buckling of the flanges and web in the plastic hinges was minimal. By increasing the level of axial force for the remaining specimens, local buckling of the flanges and web in the plastic hinges at the member ends became more significant. The lateral load versus story-drift ratio (SDR) responses in Figure 3 show that increasing the axial force level reduced the plastic moment,

triggered local buckling at a lower drift, accelerated strength degradation in the post-yield region, and reduced the energy dissipation and deformation capacities. For example, local buckling was visible during 3% drift cycles for specimen 2L ( $C_a = 0.2$ ), but local buckling was visible for specimen 2H ( $C_a = 0.6$ ) at 0.75% drift cycles. Other than experiencing local buckling at both ends, the specimens showed no sign of global buckling (either FB or LTB).

Specimen 2L was cyclically tested up to 4% drift only. To evaluate the axial capacity of a flexurally yielded column, after unloading the lateral load, the specimen was then axially compressed in its residual position to axial failure. The specimen eventually experienced out-of-plane FB at 1500 kips. Assuming an effective length factor,  $K$ , of 1.0 and using a member length equal to the distance between the two plastic hinges (i.e., severely buckled regions, 187 in. =  $0.86L$ ), the expected compression strength per AISC 360 (AISC, 2010b) is 1465 kips, which correlates well with the

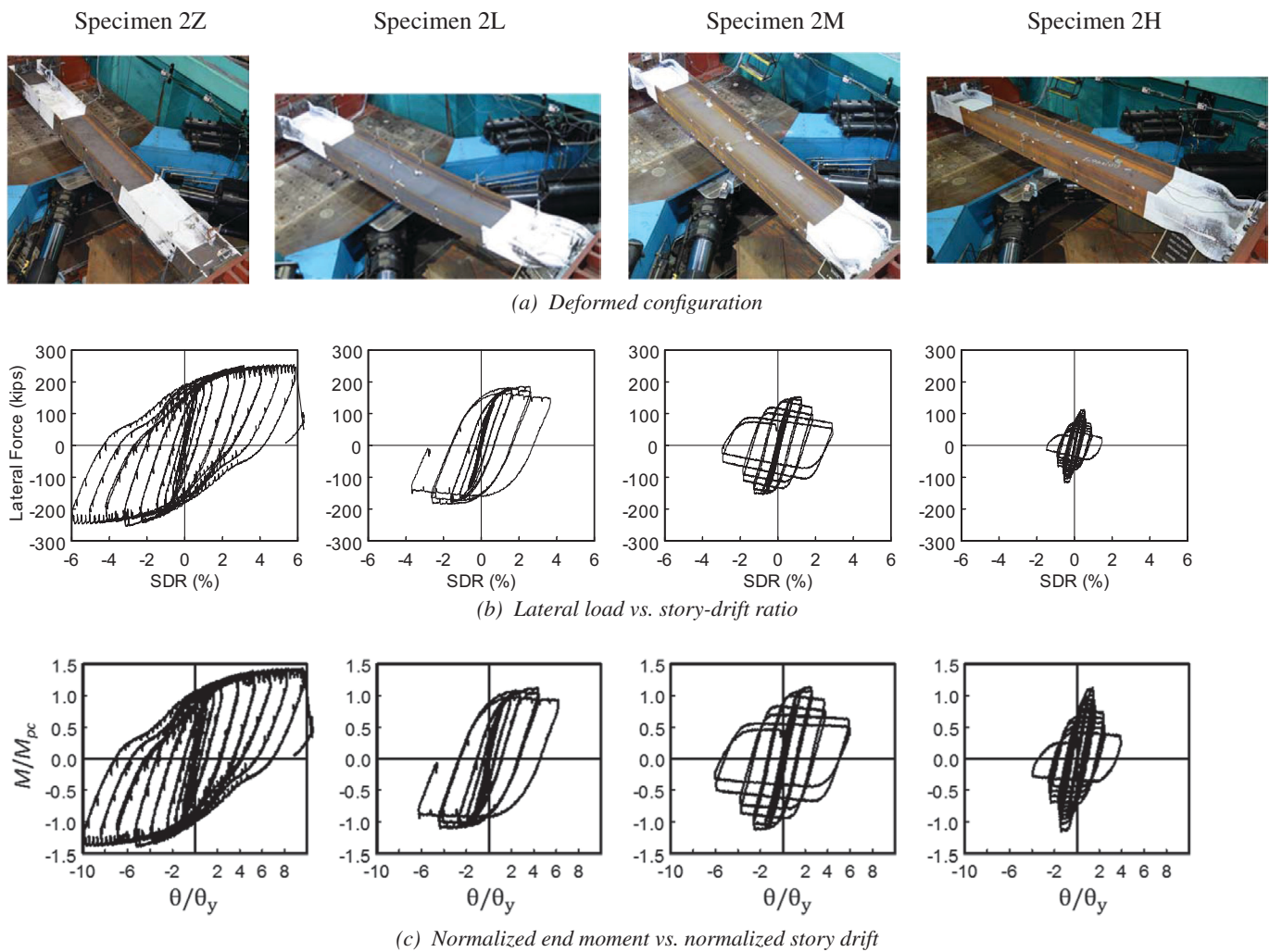


Fig. 3. Group 2 (W24×131 section): Failure mode and hysteresis response.

measured value. To evaluate the cyclic loading effect, one extra specimen, 2L-P, was monotonically loaded to 4% drift, and this “pushover” response is compared with the backbone curve for specimen 2L in Figure 12(b).

**Group 1: W24x176 Specimens**

The flange and web of group 1 specimens are more compact than group 2 specimens. It was expected that more ductility could be developed from these specimens and the extent of local buckling would be less. However, testing showed that, unexpectedly, LTB was the dominant failure mode.

It was shown that specimen 2L started to show local buckling at 3% drift. The stockier section of specimen 1L delayed local buckling to 4% drift (see Figure 4). Note that the yielded length of this group of specimens was longer when compared with those of the other groups. By having a more compact section, the onset of local buckling was delayed, and it allowed more strain hardening to occur; see Table 3 for the cyclic strain hardening ratios ( $M_{max}/M_{pc}$ ). The larger moment developed at the column ends resulted in a

longer yielded length, wherein the Young’s modulus was reduced drastically (see Figure 5). Therefore, the compressive flanges of the column were more prone to LTB. This illustrates the effect of cross-section compactness on the plastic hinge length, which in turn can influence the buckling mode.

By doubling the axial load for specimen 1M, local buckling started earlier, at 2% drift; the local buckling pattern at both ends of the column was antisymmetric. Long yielded zones at the column ends triggered the same LTB mode like specimen 1L. Tripling the axial load for specimen 1H produced local buckling at 1% drift, and the local buckling pattern at both ends of the column was symmetric. Long yielded lengths also triggered LTB, but high axial load together with the symmetric local buckling pattern caused the column to experience FB.

In summary, all three specimens first showed local buckling but eventually failed in global buckling. The yielded lengths were the longest among all groups tested due to the stockier cross-section. Specimen 1H showed

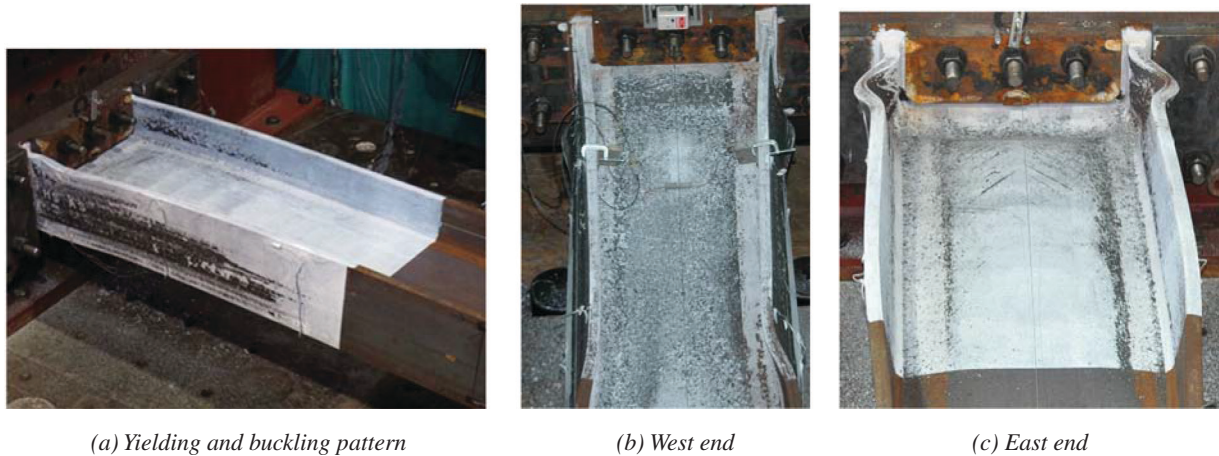


Fig. 4. Specimen 1L: Deformation at column ends (7% drift).

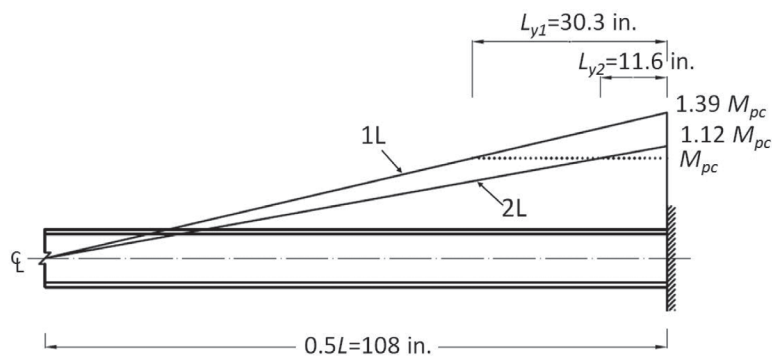


Fig. 5. Comparison of yielded length.



single-curvature FB, probably because the local buckling patterns at both ends were symmetric. Specimens 1L and 1M had antisymmetric local buckling patterns, and both failed in an S-shaped (double-curvature) LTB mode. Figure 6 shows the failure mode and hysteresis response of all three specimens.

### Group 3: W24x104 Specimens

The webs of group 3 specimens are classified as highly ductile, and the flanges are classified as moderately ductile. All three specimens in this group experienced FLB first,

which then interacted with WLB. Significant local buckling occurred at high drift levels or when the axial load was high, which was accompanied by considerable column shortening. No global buckling was observed. Depending on the direction of local buckling at member ends, one end at the buckled region might move out-of-plane in one direction, while the other end moved in either the same or opposite direction, thus causing the column segment in between to twist slightly as a rigid body. However, this deformation was not the result of global buckling. Figure 7 shows the failure mode and hysteresis response of all three specimens.

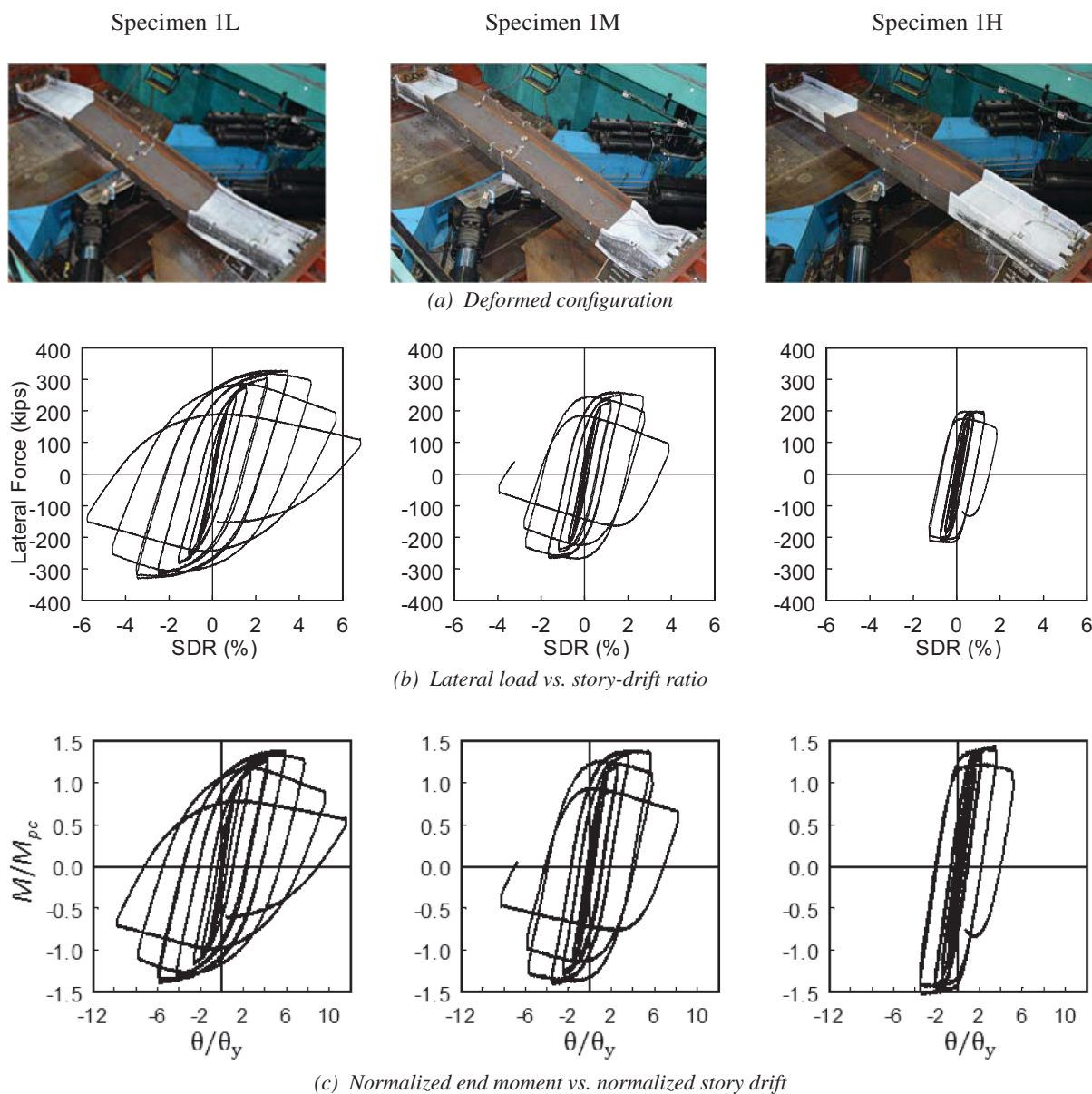


Fig. 6. Group 1 (W24x176 section): Failure mode and hysteresis response.

Specimen 3L



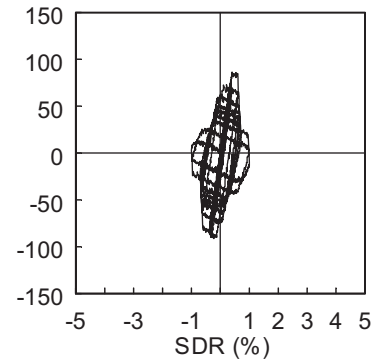
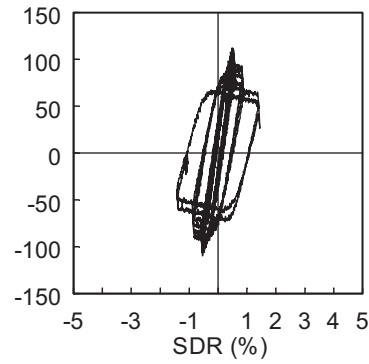
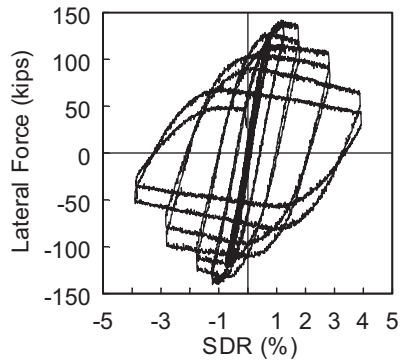
Specimen 3M



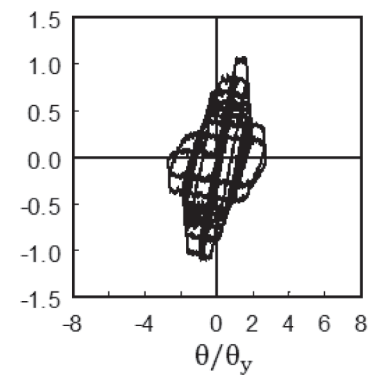
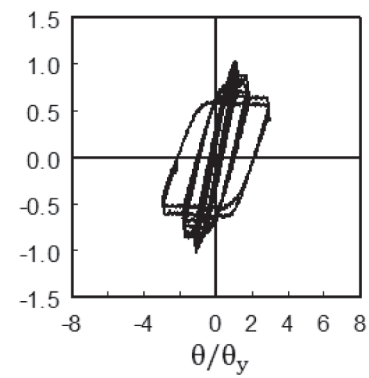
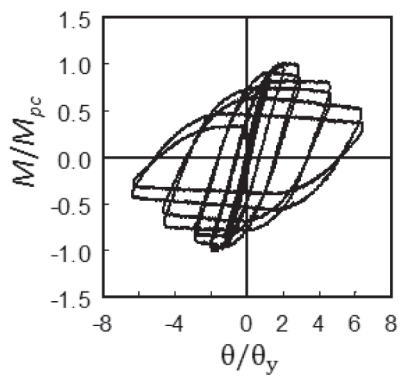
Specimen 3H



(a) Deformed configuration



(b) Lateral load vs. story-drift ratio



(c) Normalized end moment vs. normalized story drift

Fig. 7. Group 3 (W24x104 section): Failure mode and hysteresis response.



**Group 4: W24x84 Specimens**

The flanges of group 4 specimens are classified as highly ductile, and the webs are classified as highly ductile for low axial load but otherwise moderately ductile. Specimen 4L ( $C_a = 0.2$ ) experienced brittle fracture near the weld access hole at 2% drift. It was decided not to test the specimen originally planned for high axial load (4H) so that testing of 4L could be repeated. Although the slenderness ratio for LTB of this group of specimens was about 50% higher than those of the first three groups, the specimens did not fail in LTB

or FB. Instead, local buckling dominated the responses. Compared to groups 1 and 2 specimens, the larger width-to-thickness ratios of the webs caused the specimens to buckle along the entire depth of the webs, which in turn triggered local buckling of both flanges at each end. The direction of local buckling at one end of the column was reversed from that at the other end. Therefore, both specimens failed in a double-curvature configuration. Because local buckling developed along the full section depth, axial shortening was significant. Figure 8 shows the failure mode and hysteresis response for both specimens.

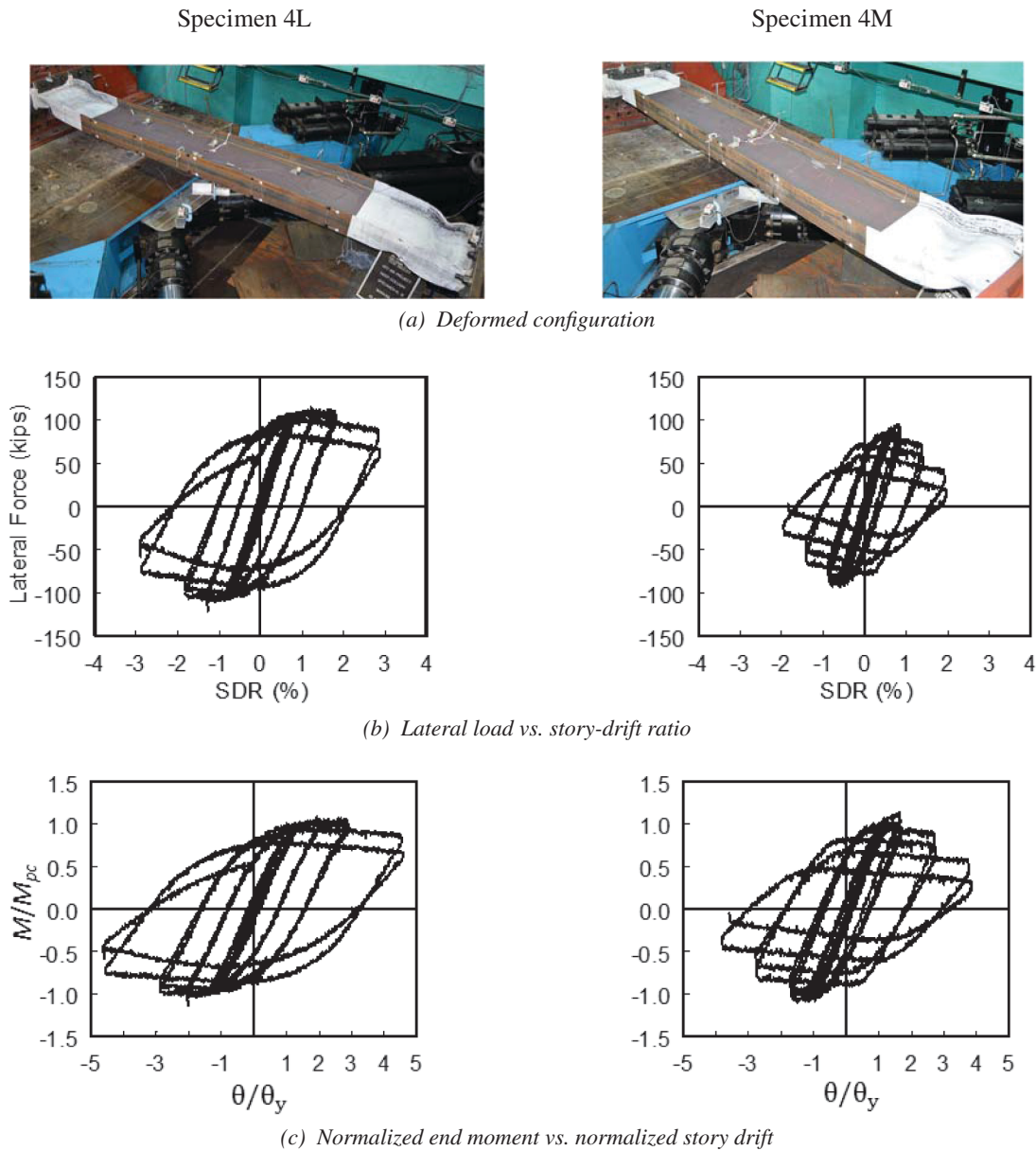


Fig. 8. Group 4 (W24x84 section): Failure mode and hysteresis response.

### Group 5: W24x55 Specimens

Three specimens were planned for this group. After testing 5L ( $C_a = 0.2$ ) and 5M ( $C_a = 0.4$ ), it was observed that the measured ductility capacity was small. Instead of testing the last specimen (5H) at the high axial load ( $C_a = 0.6$ ), it was decided to test it with an intermediate  $C_a$  value of 0.3; the specimen was designated as 5LM. The slenderness ratio for LTB was 2.2 times that of the group 2 specimens. The flanges are classified as highly ductile, and the webs did not meet the highly ductile requirement; specimen 5L was

below, 5LM was practically at and 5M exceeded the limiting value for a moderately ductile web.

With little sign of local buckling, specimen 5L experienced LTB during the 1.5% drift cycles. Alternating loading caused the same (south) flange to buckle in the same (upward) direction. The deformation amplitude was significant at 2% drift before the test was stopped. Figure 9(a) shows that LTB caused the middle portion of the column to tilt about its longitudinal axis. Local buckling was observed at one end, but it was triggered by LTB. Specimens 5LM

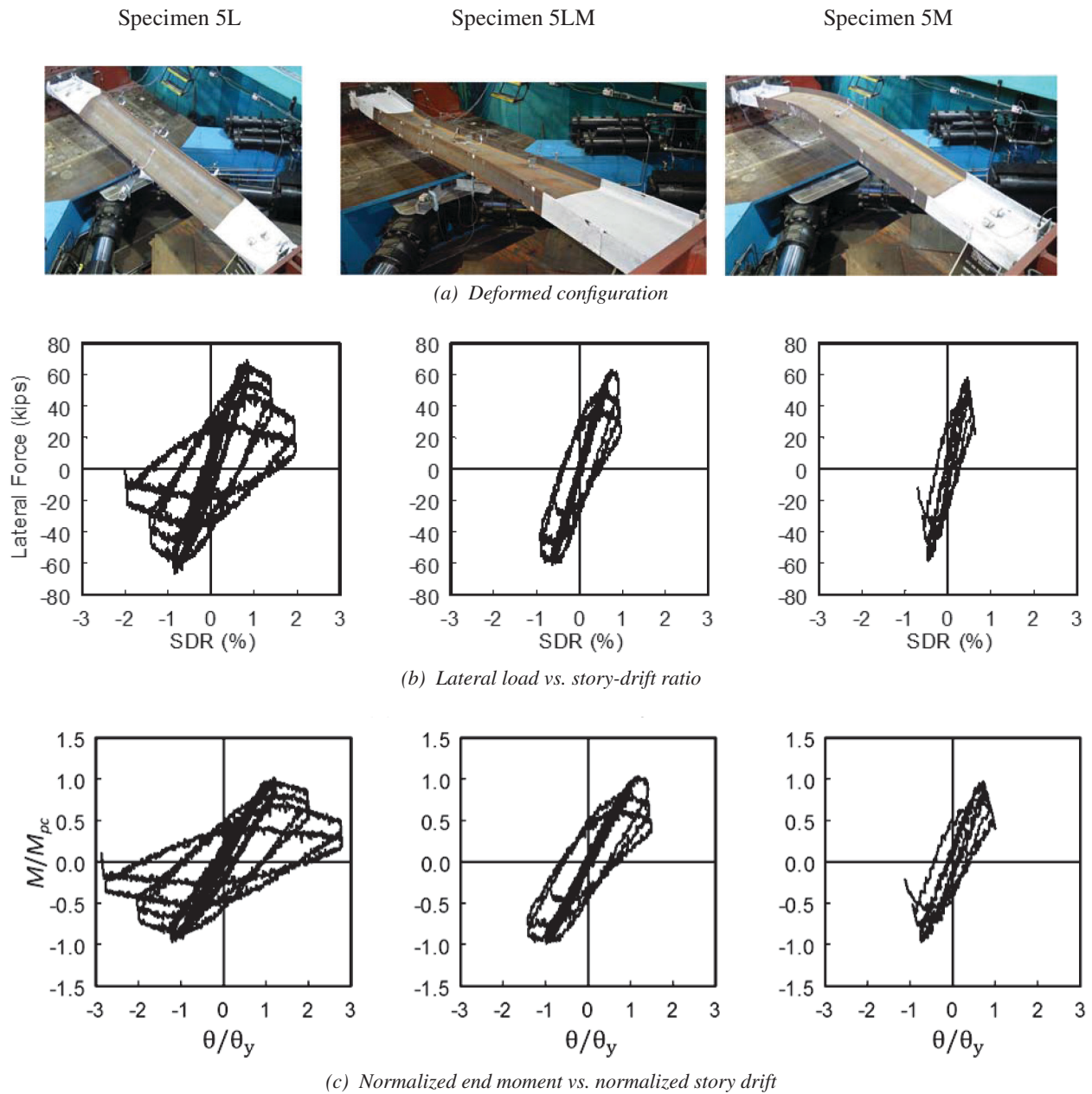


Fig. 9. Group 5 (W24x55 section): Failure mode and hysteresis response.

and 5M also showed LTB first at lower drift levels. But specimen 5M turned to FB about the weak axis during the fourth negative excursion to 0.75% drift. Specimen 5LM also turned to the same FB mode but at a slightly higher (1%) drift level. The failure mode and hysteresis response are shown in Figure 9.

**Group 6: W24x131 Specimens**

Specimens from groups 6 and 2 had the same shape and material properties, except that the former specimens were subjected to weak-axis bending. Specimen 6L was tested up to 7% drift. As expected, LTB was not a concern for

weak-axis bending. But local buckling observed in the nominally identical specimen 2L did not occur in specimen 6L, and the specimen performed in a ductile manner. Because the AISC *Specification* compactness requirement for wide-flange sections does not distinguish between strong- and weak-axis bending, testing of specimen 6L clearly shows that the AISC *Specification* compactness criterion for weak-axis bending is very conservative. Upon unloading the lateral load, it was decided to monotonically compress the column in order to evaluate the residual axial load capacity. The specimen failed by weak-axis flexural buckling at an axial load of 1627 kips. After observing the stable response of

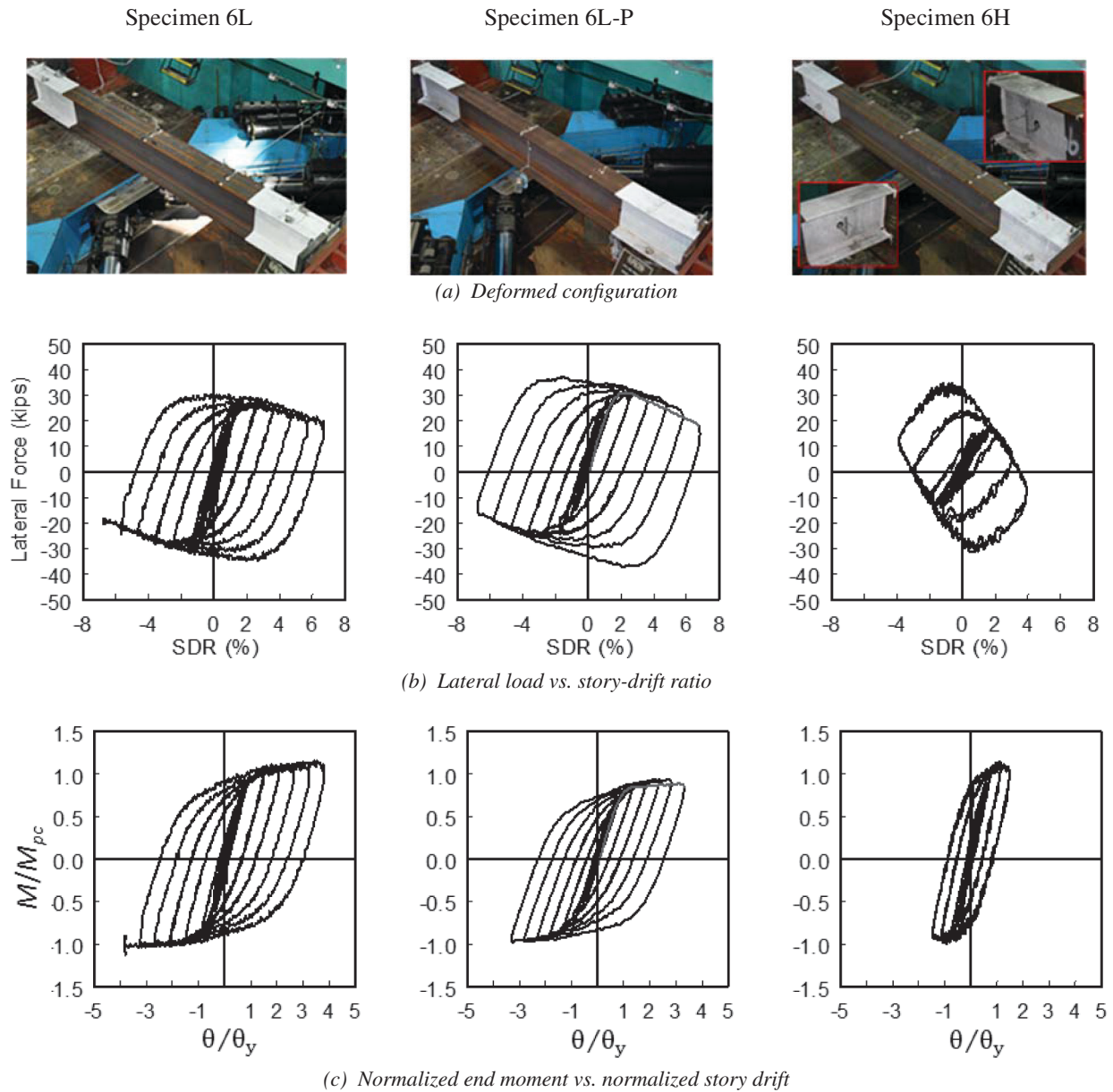


Fig. 10. Group 6 (W24x131 section): Failure mode and hysteresis response.

Table 3. Member Overstrength and Rotational Capacity					
Specimen	$M_{max}$ (kip-ft)	$M_{max}/M_{pc}$	$\theta_{yc}$ ( $\times 0.01$ rad)	$\theta_p$ ( $\times 0.01$ rad)	$R_p$
1L	3148	1.39	0.61	3.99	6.54
1M	2423	1.38	0.50	2.42	4.84
1H	2010	1.43	0.38	1.15	3.03
2Z	2327	1.41	0.63	4.95	7.98
2L	1655	1.12	0.60	2.91	4.85
2M	1430	1.13	0.49	1.07	2.18
2H	1084	1.10	0.37	0.28	0.76
3L	1262	1.03	0.62	2.82	4.55
3M	880	0.99	0.50	0.96	1.92
3H	779	1.03	0.38	0.68	1.79
4L	1039	1.05	0.63	2.85	4.52
4M	897	1.12	0.51	1.32	2.59
5L	599	1.02	0.69	0.60	0.87
5LM	594	1.03	0.63	0.26	0.41
5M	494	1.00	0.61	N.A.	N.A.
6L	454	1.15	1.78	5.68	3.19
6L-P	406	0.93	1.79	5.61	3.13
6H	337	1.14	1.74	3.49	2.00

specimen 6L, it was decided to triple the axial load and test specimen 6H. Under high axial load, minor web and flange buckling at both ends developed. The test was stopped at 4% drift due to the significant  $P-\Delta$  effect; the lateral resistance practically diminished at this drift level.

To evaluate the cyclic loading effect, it was then decided to laterally load the third specimen (6L-P) to 7% drift in order to generate a monotonic response for comparison with the backbone curve of specimen 6L. Thereafter, the specimen was subjected to the AISC loading protocol in a reverse sequence from 7% drift to evaluate the loading sequence effect. As shown in Figure 10, the sequence of loading did not affect the failure mode nor the strength of the column. But the post-buckling negative stiffness was reduced somewhat when the AISC loading protocol was applied in a reverse sequence.

## ANALYSIS OF TEST RESULTS

### Backbone Curves and Member Overstrength

The backbone curve of each cyclically loaded specimen was derived from the first cycle of each story-drift level (ASCE, 2013) as shown in Figure 11(a). The backbone curves of each of the six groups in Figure 12 show that the level of axial

load significantly affected both the strength and plastic rotation capacity of the columns.

It was observed from the behavior of group 1 specimens that significant strain hardening could alter the failure mode and trigger global buckling mode. The cyclic strain hardening ratio is evaluated as the ratio between the maximum end moment and the reduced plastic moment,  $M_{pc}$ , in Equation (5a). The ratios thus computed are listed in Table 3.

### Plastic Rotation Capacity

The plastic rotation,  $\theta_p$ , can be evaluated from the backbone curve by the procedure shown in Figure 11(b). The plastic rotation capacity,  $R_p$ , is then computed as

$$R_p = \frac{\theta_T - \theta_y}{\theta_y} = \frac{\theta_p}{\theta_y} \quad (8)$$

Figure 13(a) shows the effect of axial force level on the plastic rotation of six groups of specimens. The weak-axis specimens (group 6) delivered the highest plastic rotations. Under strong-axis bending, the slenderness ratios for both local and global buckling in addition to axial force level had a significant effect on the plastic rotation capacity. Assuming that a beam-to-column connection in an SMF is expected to achieve a story-drift angle of 0.04 radian, taking the elastic

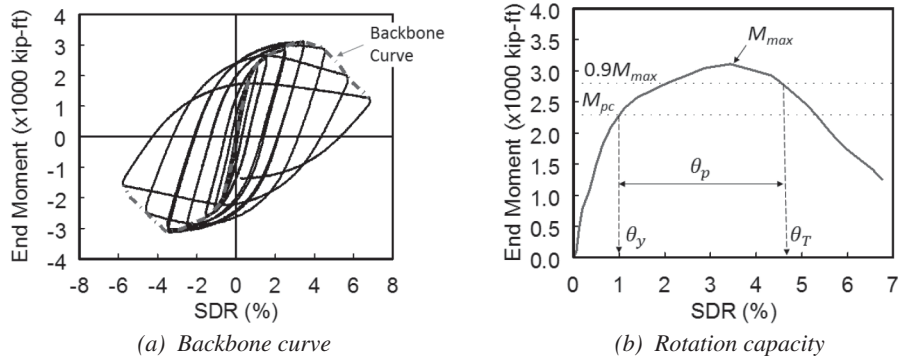


Fig. 11. Definition of backbone curve and rotation capacity.

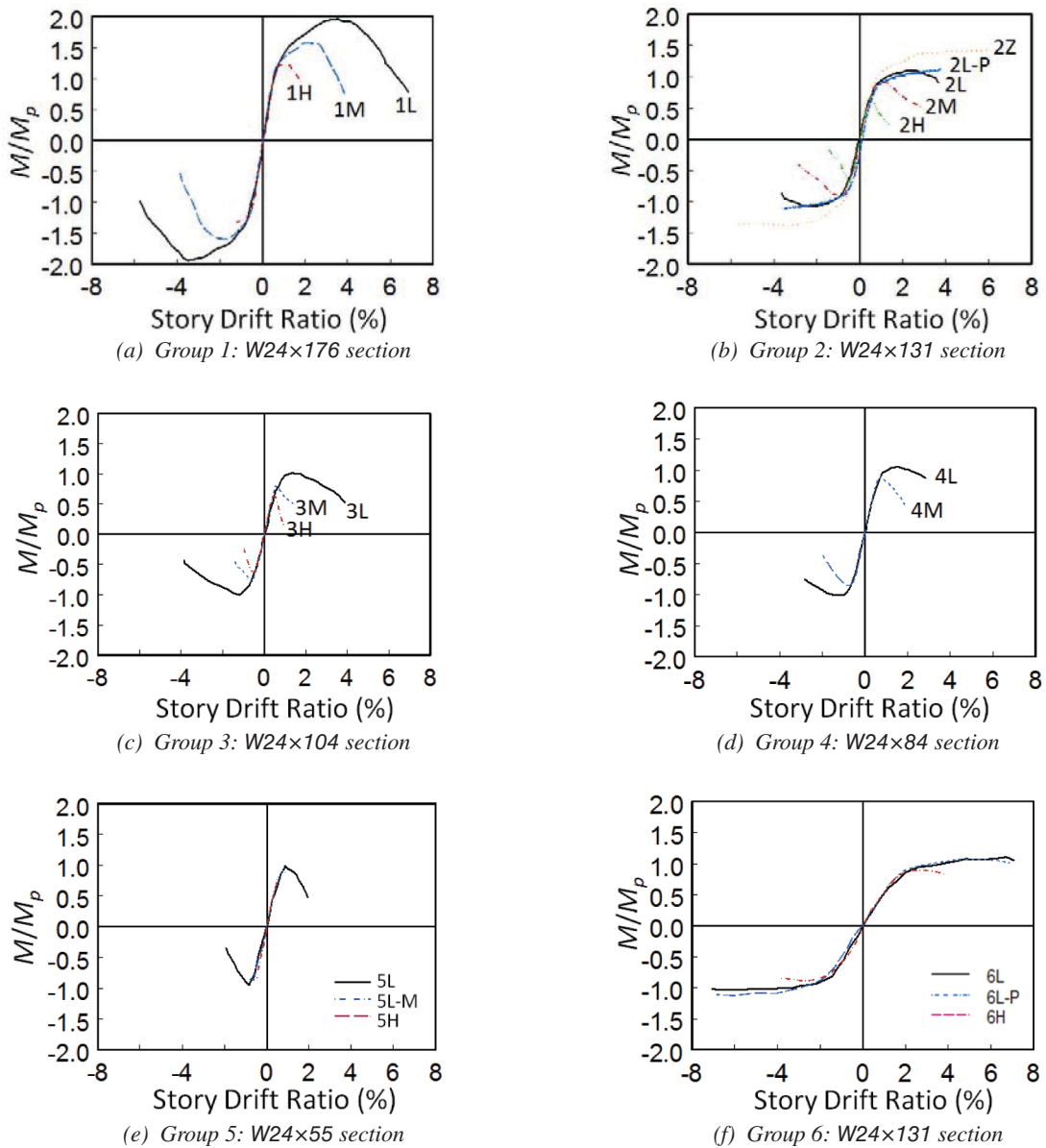


Fig. 12. Comparison of backbone curves.



component as 0.01 radian, the plastic rotation demand would be 0.03 radian. Figure 13(a) shows that the majority of deep column specimens failed to deliver this rotation.

The plastic rotation capacities of the deep, slender W24 columns tested in this research program can be compared with those of the stockier W14 columns tested by Newell and Uang (2008); these W14 columns had a  $b_f/2t_f$  ratio up to 7.2 and a  $h/t_w$  ratio up to 17.7. Taking a W14×233 column specimen ( $b_f/2t_f = 4.62$  and  $h/t_w = 10.7$ ) under cyclic axial loading with a peak  $C_a$  value of 0.6 for example, local buckling was limited even for a drift up to 0.08 rad. In-plane plastic hinging developed at both ends of the column, and the plastic rotation capacity reached 15, much higher than those of the W24 columns tested in this test program.

### Axial Shortening

With the presence of a constant axial force, most of the column specimens showed significant shortening after severe local buckling or global buckling occurred. The measured shortenings are summarized in Figure 14. Two plots are presented for each group. The first plot compares the shortenings at the end of each test. To show the effect of axial force level, the second plot compares shortenings at a given drift level; the effect of axial force level is obvious from these plots. Note that most of the nonlinear analysis software for performance-based seismic evaluation cannot model column shortening due to buckling. This effect on the margin against collapse at the system level remains to be investigated.

## CONCLUSIONS

Based on the test results of 21 W24 column specimens subjected to cyclic loading with varying levels of constant axial load, the following observations can be made:

1. The slenderness ratios for local buckling and LTB had a significant effect on the failure mode (local versus global buckling).
2. The level of axial load affected the plastic rotation capacity. Most of the strong-axis bending specimens were not able to deliver a plastic rotation of 0.03 radian (see Figure 13).
3. The presence of an axial load produced significant local buckling and axial shortening (see Figure 14).
4. Having a seismically very compact section with low width-to-thickness ratios may trigger LTB after local buckling occurs (see Figure 6 for the failure mode of group 1 specimens). The switch from local buckling to LTB was due to significant strain hardening, which extended the yielded length. From the viewpoint of post-earthquake, gravity load-carrying capacity, having a column experiencing in-plane plastic hinging with local buckling is more desirable than that experiencing global buckling of the member.
5. Specimens with weak-axis bending were ductile, showing little local buckling up to a very high drift level (see Figure 10). The AISC compactness requirement for W-shaped members with weak-axis bending is very conservative.

Because the number of tests conducted in this study was limited, more tests including those with different column depths have been planned to enhance the statistical significance of the test database. Together with supplementary analytical studies, design recommendations on the appropriate limiting cross-section element and member slenderness ratios for seismic design and assessment of steel moment frames will be provided at a later time.

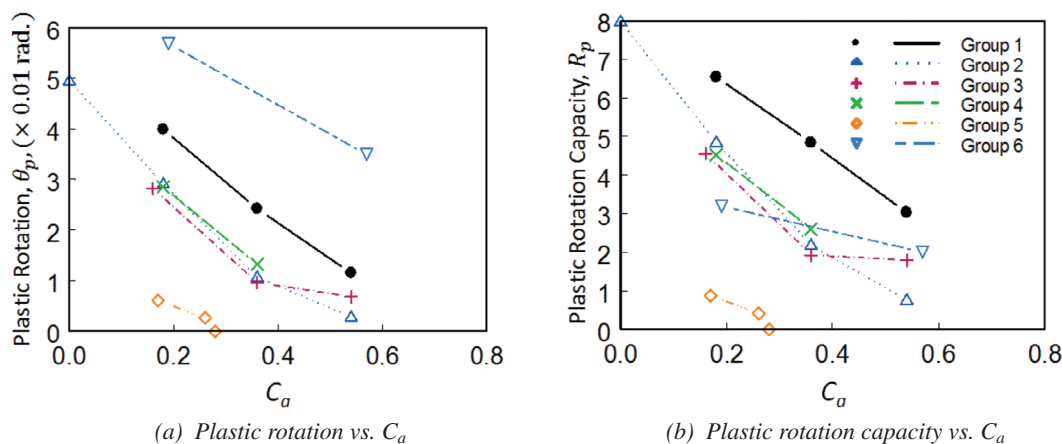
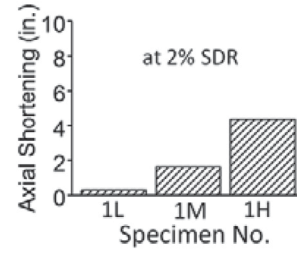
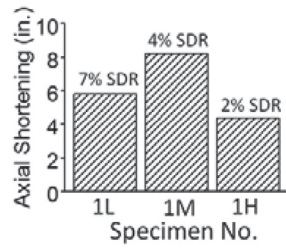
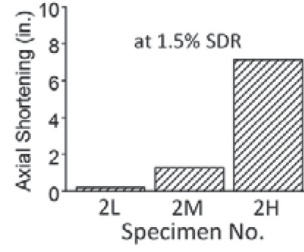
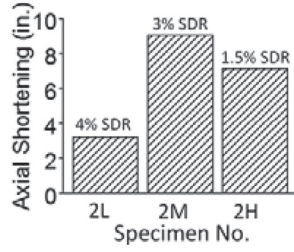


Fig. 13. Plastic rotation and plastic rotation capacity.

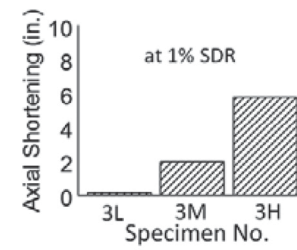
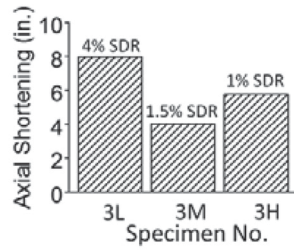




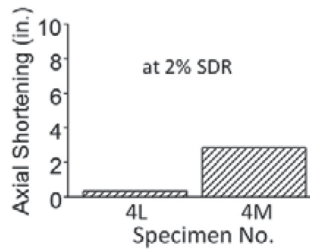
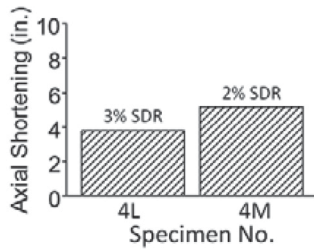
(a) Group 1 (W24x176 section)



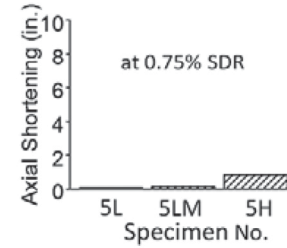
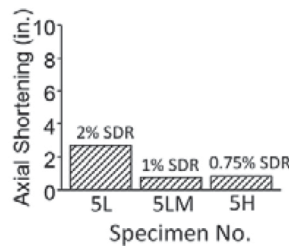
(b) Group 2 (W24x131 section)



(c) Group 3 (W24x104 section)



(d) Group 4 (W24x84 section)



(e) Group 5 (W24x55 section)

Fig. 14. Column axial shortening.

## ACKNOWLEDGMENTS

Funding for this research was provided by the NEHRP Consultants Joint Venture under its Earthquake and Structural Engineering Research contract with the National Institute of Standards and Technology. J.O. Malley from Degenkolb Engineers chaired the Project Advisory Committee, and A. Hortacsu from the Applied Technology Council served as the Project Manager. The authors also would like to acknowledge the American Institute of Steel Construction for providing steel materials and The Herrick Corporation for fabricating the test specimens.

## DISCLAIMER

NIST policy is to use the International System of Units (metric units) in all its publications. In this paper, however, information is presented in U.S. Customary Units (inch-pound) because this is the preferred system of units in the U.S. earthquake engineering industry.

## REFERENCES

AISC (2010a), *Seismic Provisions for Structural Steel Buildings*, ANSI/AISC 341-10, American Institute of Steel Construction, Chicago, IL.

AISC (2010b), *Specification for Structural Steel Buildings*, ANSI/AISC 360-10, American Institute of Steel Construction, Chicago, IL.

ASCE (2013), *Seismic Evaluation and Retrofit of Existing Building Structures*, ASCE/SEI 41-13, American Society of Civil Engineers, Reston, VA.

ASTM (2012), *Standard Specification for Structural Steel Shapes*, A992/A992M-11, American Society for Testing and Materials, Vol. 01.04, West Conshohocken, PA.

Newell, J.D. and Uang, C.-M. (2008), "Cyclic Behavior of Steel Wide-Flange Columns Subjected to Large Drift," *Journal of Structural Engineering*, ASCE, Vol. 134, No. 8, pp. 1334–1342.

NIST (2011), *Research Plan for the Study of Seismic Behavior and Design of Deep, Slender, Wide-Flange Structural Steel-Beam-Column Members*, NIST-GCR-11-917-13. Produced by the NEHRP Consultants Joint Venture, a partnership of the Applied Technology Council and the Consortium of Universities for Research in Earthquake Engineering, for the National Institute of Standards and Technology, Gaithersburg, MD.

Ozkula, G. and Uang, C.-M. (2015), "Seismic Behavior and Design of Deep, Slender Wide-Flange Structural Steel Beam-Column Members," Report No. SSRP-15/06, Department of Structural Engineering, University of California, San Diego, La Jolla, CA.



# Shear Capacity of High-Strength Bolts in Long Connections

RAYMOND H.R. TIDE

---

## ABSTRACT

Current design codes reduce the shear strength of individual bolts to account for potentially uneven distribution of force among the bolts including a 0.75/0.90 (83.3%) step function at 38 in. Available test data indicate there is no justification for a bolt shear strength reduction, especially the step function, due to the length of connection, provided that second-order effects are limited and gross and net section areas slightly exceed the AISC *Specification* limits (2010). A practical, empirical solution is proposed that maintains a reliability,  $\beta$ , slightly greater than 4.0 for all connection lengths, using the current AISC resistance factor,  $\phi$ , of 0.75.

**Keywords:** bolt shear, reliability, resistance factor, connection length.

---

## BACKGROUND

The exact solution for the load distribution in a long, bolted connection was developed by Fisher and Rumpf (1965) and reported by Kulak et al. (1987) and Tide (2012a). Because the load-deformation relationships for the bolts and plates must be known, it is not a practical solution for design purposes. Therefore, empirical solutions have been developed for bolted connections.

The current empirical shear strength of a high strength bolt (Tide, 2010) may be expressed by the following equation:

$$P_n = P_u A_b R_1 R_2 R_3 \quad (1)$$

where

$P_u$  = ultimate tensile strength of bolt, ksi

$R_1$  = 0.625, shear-to-tension ratio

$R_2$  = 0.90, initial connection length reduction factor for  $L \leq 38$  in.

= 0.75, connection length reduction factor for  $L > 38$  in.

$R_3$  = 1.00, threads excluded from shear plane

= 0.80, threads included in shear plane

$L$  = connection length between end bolt center lines, in.

$A_b$  = nominal bolt area, in.<sup>2</sup>

The design shear values for ASTM A325 and A490 bolts are given in RCSC Specification Table 5.1 (RCSC, 2014). The design values for other fasteners, such as ASTM A307 bolts and threaded material, are given in the AISC *Specification*

for *Structural Steel Buildings*, hereafter referred to as the AISC *Specification* (AISC, 2010), Table J3.2. In load resistance and factor design (LRFD) terms, the design shear strength of a bolt is  $\phi R_n$ , with  $\phi = 0.75$  and  $R_n = P_n$ . A step function with an 83.3% reduction exists at connection length equal to 38 in.

The design values are based on an extensive research program conducted by the steel industry at the Fritz Engineering Laboratory at Lehigh University from the 1950s through the early 1970s. As was the custom at the time, the high-strength bolts were fully pretensioned, and bolt threads were excluded from the shear plane. The test data were previously reported by Tide (2010, 2012a) in U.S. customary units and in S.I. dimensional units, respectively. The data are summarized in the *Guide to Design Criteria of Bolted and Riveted Joints* (the *Guide*) by Kulak et al. (1987) and will not be repeated in this paper.

The test data have also been used to evaluate and compare the bolt shear provisions of the Australian Code (Tide, 2012b) and the Eurocode provisions as found in Comité Européen de Normalization (CEN, 2003) and Tide (2012a, 2014). Because the Canadian provisions (CSA, 2001, 2005) are similar to the Eurocode criteria, all of these provisions utilize a variable bolt diameter-dependent connection length factor instead of a step function, including an increase in unit strength with increasing bolt diameter.

## CONNECTION TEST VARIABLES

All of the connections considered by Tide (2010) and in the *Guide* (Kulak et al., 1987) were loaded uniaxially to eliminate second-order effects, the bolts were pretensioned, and the threads were excluded from the shear plane. Moore et al. (2010) recommended a resistance factor,  $\phi$ , of 0.85, based

---

Raymond H.R. Tide, Principal, Wiss, Janney, Elstner Associates, Inc. (WJE), Northbrook, IL. Email: rtide@wje.com

---

on the results of approximately 1500 tests that indicated theoretical resistance factors of 0.81 and 0.87 produce a reliability of 4 for the threads excluded and threads included conditions, respectively. This can be compared to the AISC resistance factor of 0.75. Empirical data indicate that bolts will be subjected to nearly uniform shear when designs comply with current *Specification* limit states. Bendigo et al. (1963) state:

But, experimental work with riveted connections<sup>9</sup> has shown that successive yielding of the outer rivets produces a redistribution of load so that at failure a more uniform distribution exists than the elastic analysis indicates.

Reference “9” is the work presented by Davis et al. (1940). The *Guide* (Kulak et al., 1987), Section 5.2.6, pages 103 and 104, indicates that nearly equal load distribution occurs when the ratio of the plate net section to the connector shear area is large. This was confirmed by the author when the referenced papers were reviewed relative to the connection failures in long connections.

### TEST DATA

Tide (2010) compiled test data from 10 papers and reports: Bendigo et al. (1963), Fisher et al. (1963), Fisher and Kulak (1968), Fisher and Yoshida (1970), Foreman and Rumpf (1961), Kulak and Fisher (1968), Power and Fisher (1972), Rivera and Fisher (1970), and Sterling and Fisher (1965, 1966). Because of the various reporting formats and test parameters, the results were not directly comparable. Instead, the published test ultimate shear strength of each connection was reduced to an average ultimate shear strength,  $P_{TEST}$ , of a single connector, bolt or rivet, loaded on two shear planes (double shear). The predicted ultimate shear strength of the same connector was computed using appropriate single shear connector test data multiplied by 2,  $P_{PRED}$ , for each lot of bolts or rivets.

The ratio  $P_{TEST}/P_{PRED}$  was then computed and entered into a database to compare the results with connection length as the only independent variable. Tide (2010, 2012a) presents the results, which are not repeated here. Though Tide included test results for Huck bolts and rivets, these fasteners are not considered in this paper.

The test data were then plotted as shown in Figure 1 after being conditioned according to the AISC *Specification* (2010) limit states of connection gross area and net area requirements, respectively. The specifications limit states were modified by a factor of 0.90. Development of these criteria is found in Tide (2010, 2012a). Conditions for which both the gross area ( $A_g$ ) and net area ( $A_n$ ) limit states are satisfied—the  $P_{TEST}/P_{PRED}$  data—are shown as circles in Figure 1. The plotted data are in a nondimensional form,

eliminating the variability of bolt diameter, material type and connection configuration. When only one of the limit states is satisfied, the data are shown as triangles. When neither limit state is satisfied, the data are shown as squares.

The data plotted in this form clearly indicate that when the connection gross and net area limit states were satisfied, all bolts in the connection were approximately equally loaded to their maximum shear capacity. As shown in the Appendix of Tide (2010), this load condition occurs when the gross area ( $A_g$ ) and net area ( $A_n$ ) comply with the following:

$$A_g \geq 0.47A_s F_u / F_{yp} \quad (2)$$

and

$$A_n \geq 0.56A_s F_u / F_{up} \quad (3)$$

where

- $A_g$  = connection plate gross area, in.<sup>2</sup>
- $A_n$  = connection plate net area, in.<sup>2</sup>
- $A_s$  = total effective bolt shear area, in.<sup>2</sup>
- $F_u$  = bolt ultimate tensile stress, ksi
- $F_{yp}$  = plate yield stress, ksi
- $F_{up}$  = plate ultimate tensile stress, ksi

This condition is implied when Figures 5.24 and 5.25 of the *Guide* (Kulak et al., 1987) are examined for large  $A_n/A_s$  ratios.

It has been shown by Tide (2010, 2012a, 2012b, 2014) that bolt diameter, current rivet and bolt material, and current plate material grades do not influence the connection capacity provided the specification limit states are satisfied. These limit states have been addressed when the plate material gross area,  $A_g$ , and net area,  $A_n$ , requirements were developed as shown in Equations 2 and 3, respectively. Therefore, these subjects will not be discussed further in this paper.

Ocel (2013) has addressed bolted and riveted connections designs in steel-framed bridges. A major effort of this work appears to address the gusset plates that connect the members together. The report is essentially silent on the historic step function for long connections that deals with the bolt or rivet ultimate shear capacity regardless of applicable gross and net area limits in the connections.

It should be noted that once the number of bolts are chosen for a particular connection that meet the gross and net area limit states, adding additional bolts to the connection has limited benefit. The failure mechanism location will change from the bolts and will subsequently occur in the connected material.

### DATA CONDITIONING

A total of 119 connection tests were identified. Of these, 40 tests were with rivets associated with the design and construction of the San Francisco–Oakland Bay Bridge and



contained insufficient information to be included in this review. Of the remaining 79 connection tests, the connector distribution was 54 A325 bolts, 18 A490 bolts, 5 rivets and 2 Huck bolts. Shingle connection data were also removed from the database. Furthermore, it was stipulated that connection test results would only be considered provided that the limit states of gross area and net area were also satisfied. The statistical analysis was performed using the remaining 7 A325 and 11 A490 bolted connections. Because of the many connection variables, the test data were reduced to a nondimensional form to limit the significance of all the variables. As a result, the connection length remained as the desired and predominate independent variable.

In the previous papers by Tide (2010, 2012a), all of the test results were included in the database. Test data that were significantly below the specification limit states were used to determine the connection reliability and related resistance factor. Alternatively, Tide (2012b, 2014) chose the data whose test results mostly satisfied the gross area and net area limit states. As seen in Figure 2, the data were further divided into two distinct groups. The first group included nine test results having a connection length of 10.5 in. The second group included nine test results having connection lengths that varied from 21.0 in to 84.0 in. The relevant test

results are given in Tables 1 and 2, respectively. The two data groups were separated because it was felt that the nine test results at 10.5 in. would unacceptably influence the reliability calculations of the other nine test results having significant variation in connection lengths.

### REGRESSION ANALYSIS

Because the latter nine test data occurred over considerable connection lengths ( $L$ ), the results can be combined using a regression analysis that represents the nine test data from which reliability analysis can be performed at discrete lengths. A linear least-square regression analysis produced the following relationship for  $P_{TEST}/P_{PRED}$ :

$$P_{TEST}/P_{PRED} = 1.0637 - 0.00092L \quad (4)$$

This linear regression analysis is graphically shown in Figure 2.

The negative slope to the regression line is small indicating that there is minimum variation in connection strength with connection length. Furthermore, the correlation coefficient is nominally low, at  $-0.458$  and would be expected as there are no test replicates in the nine test results.

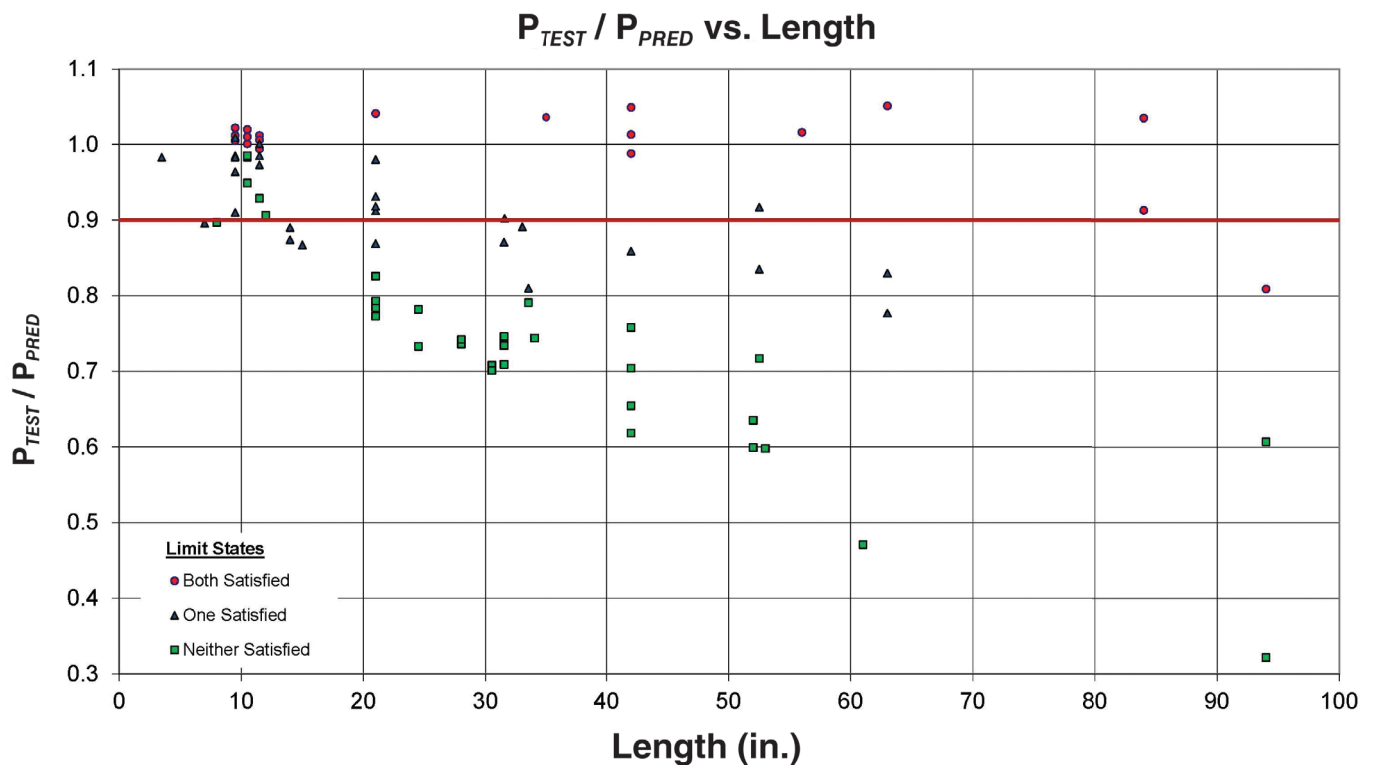


Fig. 1. Test data plotted indicating limit state considerations.

Table 1. Limit State Comparison for Compact Bolt Group Connections											
Test No.	Bolt Type	Bolts in Line	D (in.)	L (in.)	$\frac{P_{Test}}{P_{Pred}}$	$A_g$ (in. <sup>2</sup> )	$A_{gl}^{(1)}$ (in. <sup>2</sup> )	$A_g/A_{gl}$	$A_n$ (in. <sup>2</sup> )	$A_{nl}^{(2)}$ (in. <sup>2</sup> )	$A_n/A_{nl}$
1	A325	4	1½	10.5	1.001	13.0	8.3	1.52	8.07	7.8	1.04
2	A325	4	1½	10.5	1.012	13.8	8.3	1.66	8.9	7.8	1.14
3	A325	4	1½	10.5	1.005	14.5	8.3	1.75	9.66	7.8	1.24
4	A325	4	1½	10.5	1.010	15.4	8.3	1.86	10.5	7.8	1.35
5	A325	4	1½	10.5	1.022	16.3	8.3	1.96	11.4	7.8	1.46
11	A490	4	1	10.5	1.020	13.9	9.6	1.45	9.58	9.0	1.06
12	A490	4	1	10.5	1.012	14.6	9.6	1.52	10.3	9.0	1.14
13	A490	4	1	10.5	0.994	15.2	9.6	1.58	10.9	9.0	1.21
14	A490	4	1	10.5	1.006	16.0	9.6	1.67	11.6	9.0	1.29
Mean					1.009			1.663			1.214
Standard deviation					0.009			0.169			0.137

(1)  $A_{gl} = 0.90A_sF_{ub}/F_{yp}$   
(2)  $A_{nl} = 0.90A_sF_{ub}/F_{up}$

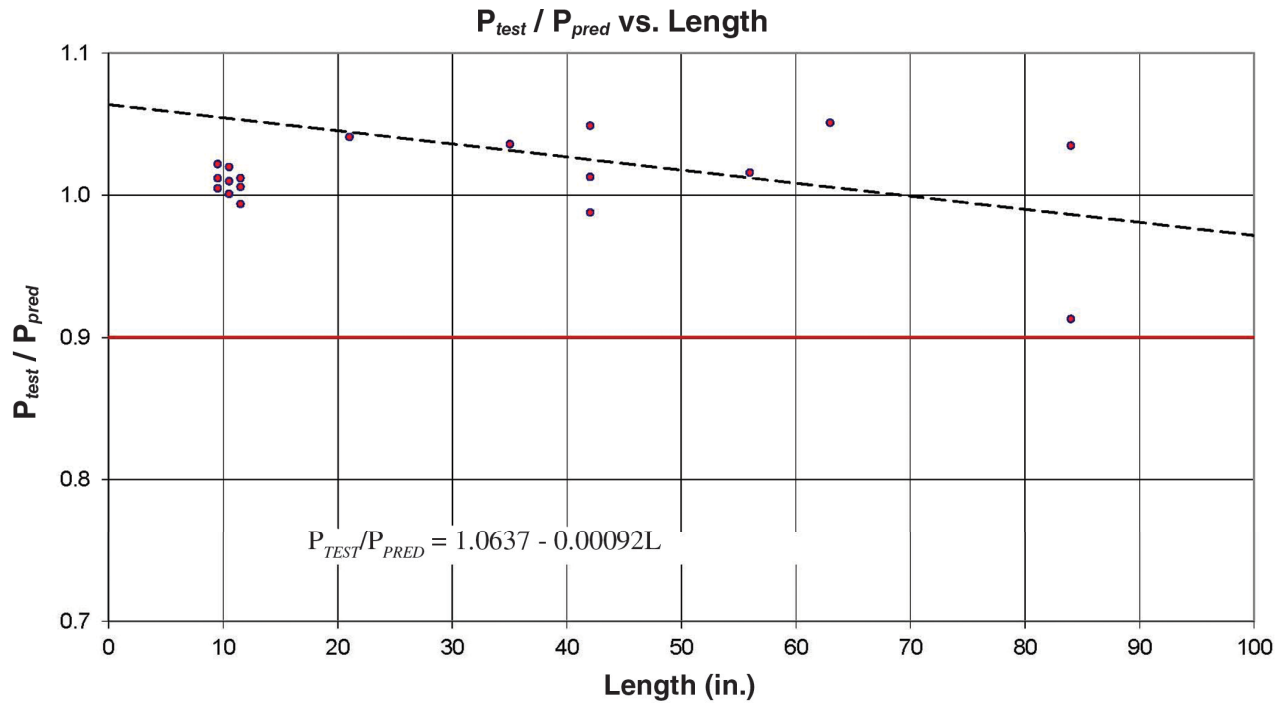


Fig. 2. Regression analysis of test data that satisfied both limit states.

**Table 2. Limit State Comparison for Dispersed Bolt Group Connections**

Test No.	Bolt Type	Bolts in Line	D (in.)	L (in.)	$\frac{P_{Test}}{P_{Pred}}$	$A_g$ (in. <sup>2</sup> )	$A_{gl}^{(1)}$ (in. <sup>2</sup> )	$A_g/A_{gl}$	$A_n$ (in. <sup>2</sup> )	$A_{nl}^{(2)}$ (in. <sup>2</sup> )	$A_n/A_{nl}$
15	A490	7	$\frac{7}{8}$	21.0	1.041	9.56	7.2	1.33	7.66	6.6	1.16
6	A325	11	$1\frac{1}{8}$	35.0	1.036	18.9	14.0	1.35	15.5	13.3	1.17
16	A490	13	$1\frac{1}{8}$	42.0	1.049	28.6	22.1	1.29	23.7	20.0	1.19
9	A490	13	$\frac{7}{8}$	42.0	1.013	33.6	29.8	1.12	29.8	17.6	1.68
10	A325	13	$\frac{7}{8}$	42.0	0.988	29.8	25.7	1.16	26.1	14.8	1.76
17	A490	17	$\frac{7}{8}$	56.0	1.016	20.4	17.5	1.17	18.5	15.9	1.16
51	A490	13	$\frac{7}{8}$	63.0	1.051	33.8	30.0	1.13	30.0	18.7	1.61
18	A490	25	$\frac{7}{8}$	84.0	0.913	28.4	24.6	1.15	24.6	24.1	1.03
19	A490	25	$\frac{7}{8}$	84.0	1.035	37.6	26.6	1.41	33.7	24.1	1.40
Mean				52.1	1.016			1.234			1.351
Standard deviation				21.6	0.043			0.110			0.269

(1)  $A_{gl} = 0.90A_sF_{ub}/F_{yp}$   
(2)  $A_{nl} = 0.90A_sF_{ub}/F_{up}$

**RELIABILITY**

With the recommended shear strength design criteria established, it is now possible to evaluate the test results in terms of LRFD procedures. The reliability index ( $\beta$ ) is determined from Fisher et al. (1978):

$$\beta = \frac{\ln\left(\frac{\bar{R}}{\bar{Q}}\right)}{\sqrt{V_R^2 + V_Q^2}} \tag{5}$$

And the corresponding resistance,  $\phi$ , is:

$$\phi = \frac{R_m}{R_n} \text{EXP}(-0.55\beta V_R^2) \tag{6}$$

where

- $\phi$  = bolt shear resistance
- $\bar{R}$  = mean resistance
- $\bar{Q}$  = mean load effect
- $V_r$  = coefficient of variation for  $\bar{R}$
- $V_Q$  = coefficient of variation for  $\bar{Q}$
- $R_m$  = mean test value
- $R_n$  = proposed connection length design criteria ( $R_2$ )

In Equation 6,  $\phi$  is dependent upon knowing  $\beta$ . Similarly, when the step-by-step procedures are followed to solve Equation 5,  $\phi$  is required to solve for  $\beta$ . This dilemma is resolved by using the current AISC (2010) and RCSC (2014) specified resistance value,  $\phi$ , of 0.75. The corresponding  $\phi$  and  $\beta$  values for the nine tests at 10.5 in. and at three connection

lengths of 38 in., 60 in. and 84 in. are given in Table 3. Two possible length reduction factors were chosen—initially,  $R_2 = 0.90$  was considered; subsequently, the reduction factor was eliminated or  $R_2$  was set equal to 1.0. The reliability,  $\beta$ , and resistance,  $\phi$ , in Table 3 are based on a live to dead load ratio of 3. Both  $\beta$  and  $\phi$  will slightly change as the live to dead load ratio changes.

The critical issues were the importance of connection strength and quasi-stiffness as the connections became longer. The relatively small change in  $\beta$  (Table 3) as the connection length increases reinforces the small change in the value of  $P_{TEST}/P_{PRED}$  given by the linear-regression analysis in Figure 2.

When the computed values shown in Table 3 are compared to the target  $\beta$  value of 4.0 and the resulting resistance,  $\phi$ , compared to the specified value of 0.75, it can be concluded, for connections that satisfy Equations 2 and 3, that there is no need to reduce the bolt shear strength because of connection length. With the reliability values higher than the target value (4.0) and resulting resistance greater than the assumed starting value (0.75), it can be considered that the test results demonstrate ample strength to accommodate small amounts of second-order effects.

**SUMMARY AND CONCLUSIONS**

A review of the historic research test data was made to determine bolt shear strength in terms of LRFD principles. Of the 119 identified bolted connection tests only 18 tests—7 A325 and 11 A490—satisfied the modified limit state requirements of gross and net area. These 18 tests were used in

Table 3. Reliability $\beta$ and Resistance $\phi$ for Alternative Design Criteria ( $R_2$ ) <sup>(1)</sup>						
Connection Length, in.	$R_m$	Standard Deviation	$R_2 = 0.9$		$R_2 = 1.0$	
			$\beta$	$\phi$	$\beta$	$\phi$
10.5	1.009	0.009	4.72	0.89	4.22	0.82
38	1.029	0.043	4.72	0.89	4.23	0.82
60	1.009	0.043	4.62	0.87	4.14	0.81
84	0.986	0.043	4.51	0.86	4.02	0.79

(1) Based on a live to dead load ratio of 3.

the statistical analysis. Recent tests reported by Moore et al. (2010) indicated that the reliability index ( $\beta$ ) of the shear strength of individual bolts was similar to that of plates and shapes reported in earlier literature. Based on other anecdotal information, there does not appear to be any justification to change the current AISC/RCSC resistance ( $\phi$ ) unless all second-order effects are considered and addressed.

The commentary to the AISC *Specification* (AISC, 2010) indicates an implied reliability,  $\beta$ , of approximately 4.0 for connections. In comparison, manufactured main members typically have  $\beta$  of approximately 3.0 or slightly lower. Because the bolt itself is a manufactured product, there is some leeway as to what  $\beta$  is acceptable. As a practical matter, it is prudent to retain a computed reliability relatively close to or greater than the stated goal of 4.0, as shown in Table 3. This eliminates the need for detailed second-order analysis for routinely used connections. To accomplish this, the current resistance,  $\phi$ , of 0.75 was used in the computations, although the resulting computations (Table 3) and research by Moore et al. (2010) indicate the resistance could be increased.

An unexpected result of the study was the realization that, under circumstances of sufficient or slightly increased code required connection strength, as manifested by the net area ( $A_n$ ), and in conjunction with connection quasi-stiffness, as manifested by the connection gross area ( $A_g$ ) in comparison to the total bolt shear area ( $A_s$ ), there would be no need for a connection strength reduction  $R_2$  less than 0.90 with increasing length. The  $R_2$  factor could possibly even equal 1.0. This condition exists when the inequalities expressed in Equations 2 and 3 are satisfied. Equation 2 is not exactly a stiffness criterion, but it indicates that the connection plates remain essentially elastic as the bolt ultimate shear strength is reached.

All of the test data represent uniaxial loaded connections with no second-order effects. In reality, many connections actually result in small amounts of unintended and unaccounted for second-order effects. Although not explicitly stated, this phenomenon is partially addressed by the specifications employing a slightly reduced resistance,  $\phi$ , of 0.75 as compared to the value obtained from single-bolt tests as

reported by Moore et al. (2010).

As a result, it is probable that the current reduction factor of 0.90 for connection lengths less than or equal to 38 in. is slightly conservative, and the step function change to a reduction factor of 0.75 for connections greater than 38 in. is excessively conservative. Removing the connection length reduction factor,  $R_2 = 1.0$ , would maintain a reliability,  $\beta$ , equal to or greater than 4.0 for all connection lengths. Bolted connections with obvious second-order effects would have to be properly addressed following LRFD principles.

The statistical study was based on ASTM A325 and A490 bolts; however, limited studies indicate that similar results were obtained for rivets with no inconsistencies found. The connection plate material varied from relatively low-strength to high-strength steel. This would indicate that the proposed solution is applicable for other connectors and material, provided the specification limit states for gross area,  $A_g$ , and net area,  $A_n$ , are satisfied as well as Equations 2 and 3.

## ACKNOWLEDGMENTS

The author wishes to acknowledge several colleagues who assisted him in this bolted connection study: T.V. Galambos, who set up the reliability procedure that was used to calibrate  $\beta$ , and D.D. Crampton, who prepared the graphic presentations and assisted with some data interpretations.

## REFERENCES

- AISC (2010), *Specification for Structural Steel Buildings*, ANSI/AISC 360-10, American Institute of Steel Construction, Chicago, IL.
- Bendigo, R.A., Hansen, R.M. and Rumpf, J.L. (1963), "Long Bolted Joints," *Journal of the Structural Division*, ASCE, Vol. 89, No. ST 6, Proc. Paper 3727, December.
- CEN (2003), *Eurocode 3: Design of Steel Structures*, European Committee for Standardization, Brussels, Belgium, November.
- CSA (2001), *Limit States Design of Steel Structures*, CSA-S16-01, Canadian Standards Association, Rexdale, Ontario, Canada.

- CSA (2005), *Supplement 1 to CAN/CSA-S16-01, Limit States Design of Steel Structure*,. CSA S16s1-05, Canadian Standards Association, Rexdale, Ontario, Canada.
- Davis, R.E., Woodruff, G.B and Davis, H.E. (1940), "Tension Tests of Large Riveted Joints," *Transactions*, ASCE, Vol. 105.
- Fisher, J.W., Ramseier, P.O. and Beedle, L.S. (1963), "Strength of A440 Steel Joints Fastened with A325 Bolts," *Publications*, IABSE, Vol. 23.
- Fisher, J.W. and Rumpf, J.L. (1965), "Analysis of Bolted Butt Joints," *Journal of the Structural Division*, ASCE, Vol. 91, No. ST5, October.
- Fisher, J.W. and Kulak, G.L. (1968), "Tests of Bolted Butt Splices," *Journal of the Structural Division*, ASCE, Vol. 94, ST11, November.
- Fisher, J.W. and Yoshida, N. (1970), "Large Bolted and Riveted Shingle Splices," *Journal of the Structural Division*, ASCE, Vol. 96, No. ST9, Proc. Paper 7534, September.
- Fisher, J.W., Galambos, T.V., Kulak, G.L. and Ravindra, M.K. (1978), "Load and Resistance Factor Design Criteria for Connectors," *Journal of the Structural Division*, ASCE, Vol. 104, No. ST9, September.
- Foreman, R.T. and Rumpf, J.L. (1961), "Static Tension Tests of Compact Bolted Joints," *Transactions*, ASCE, Vol. 126.
- Kulak, G.L. and Fisher, J.W. (1968), "A514 Steel Joints Fastened by A490 Bolts," *Journal of the Structural Division*, ASCE, Vol. 94, No. ST10, October.
- Kulak, G.L., Fisher, J.W. and Struik, J.H.A. (1987), *Guide to Design Criteria for Bolted and Riveted Joints*, 2nd Edition, John Wiley and Sons, New York, NY.
- Moore, A.M., Rassati, G.A. and Swanson, J.A. (2010), "An Experimental Analysis of Strength and Ductility of High-Strength Fasteners," *Engineering Journal*, AISC, Vol. 47, 3rd Quarter, No. 3.
- Ocel, J.M. (2013), "Guidelines for the Load and Resistance Factor Design and Rating of Riveted and Bolted Gusset-Plate Connections for Steel Bridges," National Cooperative Highway Research Program (Project 12-84), February.
- Power, E.H. and Fisher, J.W. (1972), "Behavior and Design of Shingle Joints," *Journal of the Structural Division*, ASCE, Vo. 98, No. ST9, September.
- RCSC (2014), *Specifications for Structural Joints Using High Strength Bolts*, Research Council on Structural Connections, Chicago, IL, August 1.
- Rivera, U. and Fisher, J.W. (1970), "Load Partition and Ultimate Strength of Shingle Joints," Fritz Laboratory Report 340.6, Lehigh University, Bethlehem, PA.
- Sterling, G.H. and Fisher, J.W. (1965), "A440 Steel Joints Connected by A490 Bolts," *Journal of the Structural Division*, ASCE, Vol. 92, No. ST3, Proc. Paper 4845, June.
- Sterling G.H. and Fisher, J.W. (1966), "Tests of Long A440 Steel Bolted Butt Joints," Fritz Engineering Laboratory Report No. 288.26, Lehigh University, Bethlehem, PA.
- Tide, R.H.R (2010), "Bolt Shear Design Considerations," *Engineering Journal*, AISC, Vol. 47, 1st Quarter, No. 1.
- Tide, R.H.R. (2012a), "Shear Strength of High Strength Bolts<sup>®</sup>," Wiss, Janney, Elstner Associates, Inc., Northbrook, IL.
- Tide, R.H.R. (2012b), "Re-evaluation of Shear Strength of High Strength Bolts in AS4100," ACMSM 22 Conference, University of Technology, Sydney, NSW, Australia.
- Tide, R.H.R. (2014), "High Strength Bolt Shear Capacity in Long Connections," 7th European Conference on Steel and Composite Structures, College of Engineering, University of Napoli Federico II, Naples, Italy.



